UNIVERSITÀ
DEGLI STUDI
DI PADOVA

Head Office: Università degli Studi di Padova

Department:
Scienze Chimiche

Ph.D. COURSE IN:
Scienza e Ingegneria dei Materiali e delle Nanostrutture

SERIES: XXX

# Microscopic Insights in Photo-Induced Charge Transport in Fe : $LiNbO_3$

**Coordinator :** Ch.mo Prof. Giovanni Mattei

**Supervisor :** Dr. Marco Bazzan

**PhD student :** Laura Vittadello

# Abstract

The description of charge transport phenomena in polar oxide materials has up to now numerous unclear points, unlike for what happens for semiconductors and conductors where the band model explain exhaustively their properties. First studies on ionic insulators highlighted the necessity to introduce new concepts and a new transport theory, without which it would not be possible to explain convincingly the photo-electrical behaviour of these materials. One of these key concepts is the polaron, introduced the first time by L. D. Landau in 1933, to explain some new properties exhibited by alkali halide. A strong electron - phonon interaction characterizes these materials thanks to which the electron can induce a local distortion through Coulombian interaction. This mechanism produces a potential well localizing the electron. A polaron can be thought as a quasi-particle composed by a charge auto-localized and the relative lattice distortion that moves as a whole. Under particular conditions, it can move by thermally assisted hopping, diffuse in the material or be trapped by point defects having an attractive potential. Moreover, the polaron constitutes a localized state in the band gap, which can absorb the light releasing the trapped charge to higher energy levels. The coexistence of all these processes, under specific conditions of illumination and temperature, determine the light-induced charge transport phenomena, which are the object of this thesis. The material chosen for this research is lithium niobate ($LiNbO_3$). Besides its technological interest, since it is largely applied for nonlinear optic and holography, it is a prototype system for polaron study, among similar polar oxides. Another advantage provided by this material is that its electrical transport properties can be studied in a convenient way via optical measurements. The purpose of this study is the creation of a predictive model describing transport properties of the material starting from its microscopic composition and the external experimental conditions to which it is exposed. We performed a set of experiments on a series of well-characterized samples and compared them with the results of numerical modelling. The main results are a quantitative estimate of some poorly known microscopic polaron parameters and, by consequence, the development of a quantitative numerical tool able to predict the behaviour of the material, in a wide range of temperature and compositions. Several new ideas concerning a semi-analytical modelling for this system were also developed and tested, together with some interesting concepts for future research, traditionally not applied in lithium niobate community, such as the physics of anomalous diffusion of polarons among a disordered defect network.

# Acknowledgement

The first person that I would to thank is my scientific supervisor, Dr. Marco Bazzan. It was a pleasure to work with you during the last three years.

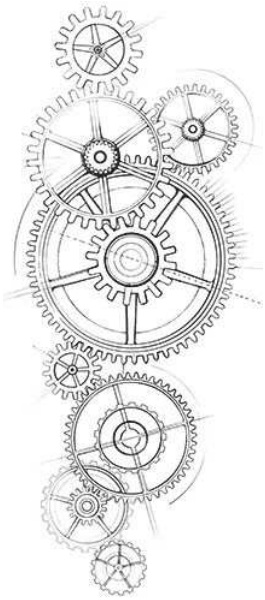

This PhD work is the result of a fruitful international collaboration and for this reason I would like also to thank:

- Prof. M. Imlau who provided me the opportunity to join his team in Osnabrück (Germany), and who gave me the access to the laboratory of Ultrafast Physics and related research facilities. A special mention is for a PhD student of this group, Simon Messerschmidt for the long discussions on polarons hopping and not just.
- Prof. Laurent Guilbert and Dr. Imed Mhaouech at the Laboratoire Matériaux Optiques, Photonique et Systèmes of the Université Lorraine et Supélec (Metz, France) for the theoretical discussions on the microscopic interpretations and modelling of experimental results.
- Prof. E. Kokanyan from the Pedagogical University of Yerevan (Armenia) who provided me with one of the three set of samples studied in this work and a PhD of this group, Anush Danielyan, on leave from the Pedagogical University of Yerevan (Armenia) and the research unit at the Laboratoire Matériaux Optiques, Photonique et Systèmes of the Université Lorraine et Supélec (Metz, France) for access to the Raman laboratory and for measurements of near stoichiometric samples.

Systematic Monte Carlo simulations to reproduce the hopping transport were possible thanks to CloudVeneto support.

Another special thanks is for Luca Bacci and Nicola Argiolas for the technical and informatics support respectively.

# Contents

# Introduction

Lithium Niobate (LN) stands out, among other ferroelectric oxides for its large use in the realisation of acusto- and electro-optic as well as non-linear optical devices. This material is also considered as a reference for other ferroelectric oxides, and it is generally used as a "test bench" where new concepts and applications can be tested both in fundamental and applied research [1].

In this scenario, lithium niobate is often taken as a paradigm for light induced charge transport phenomena in oxide crystals. This is the physical basis of the so-called photorefractive effect, which in LN is especially strong as a consequence of the high electro-optic coefficients and of the fact that large internal electric fields ($10^6 - 10^7$V/m) can be built up in the bulk simply by illuminating this material with visible low intensity light [2]. The microscopic origin of these fields are related to the interplay between the photogalvanic effect (i.e. the appearance of a bulk current density proportional to the light intensity) and the charge transport mechanisms that determine the material conduction [3]. The interest in these phenomena is timely because they bear a high interest for practical applications: in the field of nonlinear and ultra-fast optics the photorefractive effect is an unwanted drawback that limits the use of LN for high intensity multiphoton processes [4], while in photorefractive holography this effect is used to record high quality gratings, optical memories and demonstrate low-intensity all-optical interactions [5]. Integrated optics as well needs to control those phenomena due to the high cw light intensities obtained in waveguiding regions [6]. More recently, the exploding field of ferroelectric photovoltaics has raised several questions on charge transport processes in polar materials [7].

Initially these phenomena have been described by mutuating from semiconductor physics a band model picture for charge transport [8]. These models were quite successful in explaining the experimental data collected in the last decades [1], but as pointed out in Ref. [9], this approach is valid as long as it is not necessary to deal with the microscopic origin of the macroscopic parameters used in such descriptions. Moreover, with the advent of high power (ultra-) short pulsed laser system and the consequent observation of novel non-linear phenomena [4], it appeared obvious that the microscopic description of charge transport in LN needed a deep revision. These problems, discovered for lithium niobate, are part of a more general framework concerning polar oxide materials such as $KNbO_3$, $KTiOPO_4$, $BaTiO_3$, or $LiTaO_3$. In those systems the description of charge transport phenomena, unlike for what happens for semiconductors and metals, cannot be based on band model to explain exhaustively

their properties. A key concept in this respect is that of *polaron*, introduced the first time by L. D. Landau in 1933 [10]. The strong electron - phonon interaction characterizing these materials enables a charge carrier to induce a local distortion of the ionic lattice through Coulombian interaction. This mechanism produces a potential well localizing the charge carrier. Under certain conditions, a polaron can be thought as a quasi-particle composed by a charge auto-localized together with the relative lattice distortion that moves as a whole. In these conditions the charged particle cannot be described as de-localised Bloch wave function which may recombine with acceptors at any lattice site, as prescribed by the band model theory. On the contrary the charge is more or less localized (in the case of LN, practically at a single ionic site) and its movements can take place only by thermally assisted hopping transitions to adjacent sites. Polaron hopping, in this context, refers to the phonon-assisted jumping of a carrier through severely localized (collapsed) states [11]. More recently, the polaron concept appeared to play an ubiquitous role in a wide range of solid state physics topics, such as superconductivity, DNA replication, conductive polymers, ferroelectric photovoltaic or THz wave damping [12, 7, 13].

Quite surprisingly, however, in spite of the fact that the role of polarons is nowadays clear, to our knowledge a self-contained, detailed microscopic description of polaron transport meant to replace old-fashioned band-like approaches is still lacking. It appears therefore of great interest to develop a quantitative understanding on this subject by comparing different investigation methods and ad-hoc theoretical and numerical modelling. In this context, lithium niobate serves as a reference material due to its variety of small polaron features and to the abundance of literature on this respect. Another advantage provided by this material is that its electrical transport properties can be studied in a convenient way via optical measurements.

The main goals of this thesis work are therefore: (i) investigate by a combination of different complementary techniques and in a wide range of experimental conditions the charge transport mechanism in LN in order to put in evidence its polaronic features (ii) clarify what is the role of the different polaronic centres in the transport. (iii) recognize that LN, from the point of view of transport, can be considered as a *disordered system* and adapt a suitable theoretical framework to this case. (iv) Ultimately, setting up a quantitative and predictive modelling of charge transport in this material.

This work is the result of a successful international collaboration between the Physics and Astronomy Department of the University of Padova, the School of Physics of the Osnabrück University in Germany, the laboratory M.O.P.S. of the Lorraine University/Supélec in Metz, France and the Institute for Physical Research in Ashtarak, Armenia. All the involved partners contributed with experimental analysis, theoretical models, samples and ultimately deep and lively discussions. The material is organized as follows:

In chapters 1 and 2 the state of the art of the problem is reviewed. Lithium niobate is described by stressing the aspects that are necessary to deal with in the following

chapters with special attention to classical charge transport phenomena description and the physics of small polarons.

Chapter 3 describes a numerical tool developed in this thesis which will be used to interpret the results of the experimental work. It is based on a Monte Carlo simulation code describing the motion of the different polaron types in LN.

Chapter 4 describes the different samples used in this work, from their preparation to their detailed characterization.

Chapter 5 deals with the two main experimental techniques used to study polaron motion: transient absorption spectroscopy and photorefractive measurements. The first of these two complementary approaches allows to obtain information on the relaxation process of a photo-excited polaron population in non stationary conditions and give information on the different types of polaron contributing to the transport; the second permits to study the sample photoconductivity and the photogalvanic effect under constant light illumination. As a distinctive feature of this work, all the analyses are carried out as a function of temperature in the poorly explored range between 100 and 400 Kelvin, to test our theoretical modelling also from the point of view of temperature dependence.

Chapter 6 and 7 illustrate and analyse the results, finally combining in a single coherent view the different observations and numerical modelling.

Finally, Chapter 8 deals with the application of the theory of anomalous diffusion to the polaron transport.

# Part I.

# State of the art

# 1. Lithium Niobate

Lithium niobate single crystal ($LiNbO_3$, or LN) is an oxide material whose properties make it a great candidate for many linear and non-linear optical applications such as waveguides [6], electro-optic modulators, second harmonic generators, holographic devices and sensors [14]. It is an artificial crystal, described the first time in 1928 by Zachariasen [15] and synthesized in large crystal sizes for the first time in 1965 by Ballman using the Czochralski technique [16]. It exhibits strong ferroelectric, pyro-electric and piezo-electric features and it is colourless and insoluble in water and organic solvents. In this chapter its fundamental properties are reported.

## 1.1. Phase diagram and crystal structure

Lithium niobate is one of the four compounds of the pseudo-binary system $Li_2O - Nb_2O_5$, besides $Li_2Nb_{28}O_{71}$, $Li_3NbO_4$ and the lithium triniobate $LiNb_3O_8$. The first phase diagram of this system was created in 1958 [17] and was refined in the following years thanks to thermal and density analysis, as well as to X ray diffraction, obtaining the one presented in figure 1.1.1. As it can be seen LN has a variable composition having the solid phase in the range of $Nb_2O_5$ between 50% and 54%. In this interval there is only one point in which the liquid phase has the same composition of the solid one, the so-called *congruent composition*, corresponding also to the maximum melting temperature of 1253°. From the thermodynamic point of view this composition, minimizing the Gibbs free energy, gives the most stable phase of lithium niobate: this implies that energetically the preferred structure is a defective one having a $Li_2O$-deficient structure. The figure 1.1.1 shows also that, according to the composition, there is a different Curie temperature between the ferroelectric and the para-electric phase. Several physical properties related to optics and subsequently to photo-induced transport phenomena do strongly depend on the [Li] / [Nb] ratio, as it will be shown in next chapters. Literature values defining the numerical value of the congruent composition are somehow dispersed. In this work $x = [Li] / ([Li] + [Nb]) = 0.4845$ is considered, according to one of the most recently result obtained in [1].

The structure of lithium niobate at room temperature belongs to the rhombohedral (trigonal) space group R3c and the point group is 3m. This structure is stable up to the Curie temperature ($T_C$) where a transition to the non polar point group $\bar{3}m$ occurs. In the trigonal system three are the possibles choices for the elementary cell namely hexagonal, rhombohedral or orthogonal. The former two are convenient for crystallo-

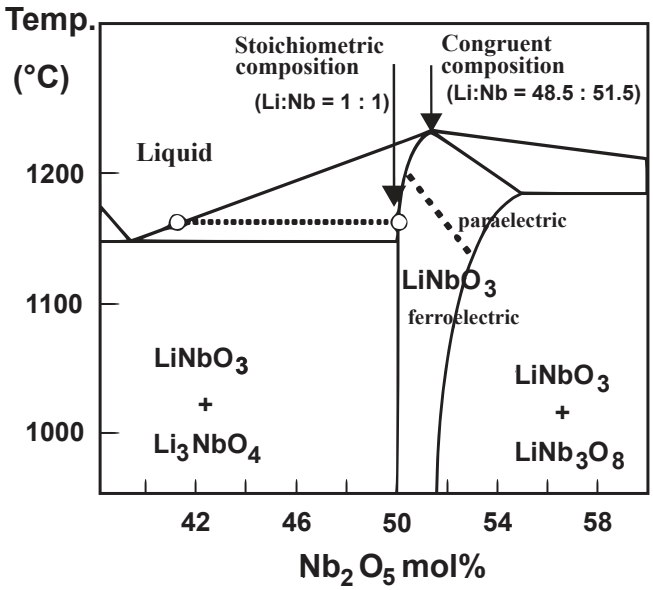


Figure 1.1.1.: Schematic phase diagram of the pseudo binary system $Li_2O - Nb_2O_5$ near the congruent and stoichiometric composition of $LiNbO_3$ [18].

graphic aims and structural investigations, but for most applications the orthogonal setting is the preferred one, therefore tensor components of the material properties are usually given with respect to its x, y and z axes, which are all orthogonal. Among all the possibilities the hexagonal unit cell is the only one here briefly described because the only one later used to simulate the results (chapter 3). In this cell, represented in figure 1.1.2, the c axis corresponds to the z-axis of the orthogonal cell and to the optical axis. It is defined as the axis about which the crystal exhibits a three-fold rotation symmetry, with the positive end point toward the crystal face where a positive charge appears by cooling the material. This cell, has the form of a right parallelepiped with a rhombohedral base defined by two equal lengths $a = b = 5.150 \pm 0.002\,\text{Å}$ having an angle of 120° between them and the third one in the normal plane equal to $c = 13.867 \pm 0.005\,\text{Å}$ [19]. The x axis corresponds to the [1 1 -2 0] direction in this setting, while the y axis to the [1 -1 0 0].

The lithium niobate structure at temperatures below its Curie point, consists of planar sheets of oxygen atoms in a slightly distorted hexagonal close-packed configuration. The octahedral interstices formed by this oxygen structure in the congruent composition are one-third filled by lithium atoms, one-third by niobium and one third is vacant, following along the c axis the order Vacancy - Li - Nb (figure 1.1.3 a). In this phase cations do not occupy the central position of the octahedra but Li ions are shifted with respect to the O planes by about 44 pm, and the Nb ions by 27 pm from the centre of the octahedra. These shifts are the origin of the spontaneous polarization. The positive polarization direction is conventionally the one for which the Li displacement with respect to oxygen planes is positive.

Since the chemical bond between niobium and oxygen is essentially covalent, the Nb

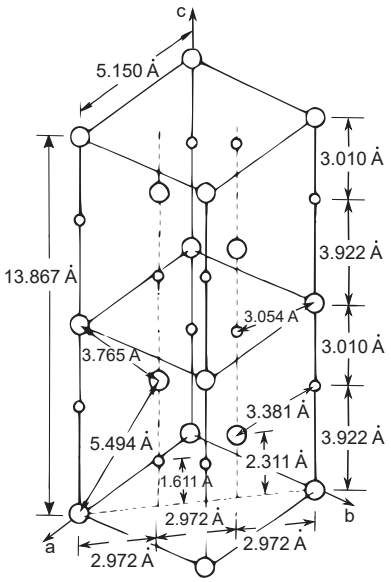


Figure 1.1.2.: Hexagonal unit cell of lithium niobate with interatomic distances and axis lengths indicated [20].

and 6 atoms of oxygen are considered as a single entity. This fact, together with the one that Li atoms are highly decentered with respect to the centre of the oxygen octahedra leads to adopt the vision illustrated in the figure 1.1.3 b/c where a sequence of octahedra and triangle of oxygen is considered instead of the one of connected octahedra. In the paraelectric phase, above Curie temperature, lithium atoms lie in the centre of oxygen planes, while niobium ions are located at the centre of oxygen octahedral making this phase non-polar.

## 1.2. Defect structure

As already mentioned the congruent composition is the most energetically favoured and the one normally encountered in commercially available samples. This structure is Li deficient and naturally defective, so that it is of main importance to understand and evaluate its impact on the physical properties of the material, especially for what concerns charge transport.

### 1.2.1. Intrinsic defects

As already mentioned, the congruent composition is characterized by a Li fraction of $x = [\mathrm{Li}] / ([\mathrm{Li}] + [\mathrm{Nb}]) = 0.4845$, corresponding to about 6% empty Li sites in the lattice. Charge compensation for such deficiency can be described by several possible processes of $Li_2O$ outdiffusion. Using the Kröger-Vink notation [21], the formation of defects can be described by the following equations:

$$(\mathrm{LiNbO_3}) \rightarrow \mathrm{Li_2O} + 2\mathrm{V}'_{\mathrm{Li}} + \mathrm{V}_{\mathrm{O}}^{2\bullet} \tag{1.2.1}$$

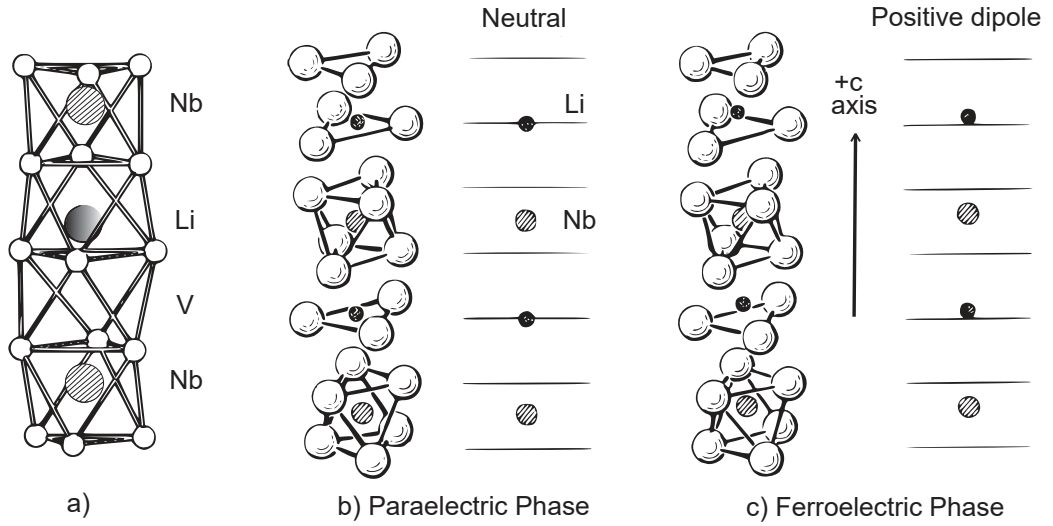


Figure 1.1.3.: (a) Crystal structure of congruent $LiNbO_3$. (b) Paraelectric phase. (c) Ferroelectric phase [20].

$$(LiNbO_3) \rightarrow 3Li_2O + 4V'_{Li} + Nb^{4\bullet}_{Li} \tag{1.2.2}$$

$$(LiNbO_3) \rightarrow 3Li_2O + 4V^{5'}_{Nb} + 5Nb^{4\bullet}_{Li} \tag{1.2.3}$$

which are respectively known as *Oxygen vacancy model*, *Lithium vacancy model* and *Niobium vacancy model*. The equation 1.2.1 assumes that the lithium vacancies are compensated by oxygen vacancies, as it usually occurs in the oxides perovskites. On the contrary the equation 1.2.2 implies that some $V_{Li}$ are filled by Nb ions, forming the so called *niobium antisites* $Nb_{Li}$, whereas the equation 1.2.3 states that *all* the lithium vacancies are filled with niobium antisites, leading to the formation of niobium vacancy, $V_{Nb}$. Density measurements [22] rather early discarded the first model, because they showed an increase in the density of $LiNbO_3$ with decreasing of $Li_2O$ content, which is inconsistent with the oxygen vacancy model. On the contrary experimental results can be justified by assuming the presence of niobium antisites. Evidently the formation of $Nb_{Li}$ costs less energy than that of $V_O$ and therefore only the two latter compensation mechanisms can be taken into account. Calculations of the defect formation reveal that the mechanism 1.2.2 is the most energetically favourable, but this was in contradiction with the first result of Abrahams and Marsh [23], according to which Nb ions occupy 4.9% of the Li site in the crystal, i.e. the empty Li sites are mostly populated by Nb. However, further structure results led to different conclusions. According to precise data of X-ray and neutron diffraction [24] only 1% of the Li sites are occupied by Nb, whereas about 4% of the Li sites are empty. These data support again the Li vacancy model 1.2.2. Nowadays, the *lithium vacancy model* is commonly accepted as valid.

$Nb_{Li}$ antisite defect has been identified clearly, using Electron Paramagnetic Resonance (EPR) technique and related studies [25]. In the ground state of a congruent crystal, $Nb_{Li}$ is present in the diamagnetic charge state $Nb^{5+}_{Li}(4d^0)$, but after a two-

photons, X-ray irradiation or a reduction treatment and subsequent illumination of the crystal, the paramagnetic configuration $Nb_{Li}^{4+}(4d^1)$ can be observed, indicating that this defect can work as an acceptor for electrons. Thanks to optical absorption measurements, it has been possible to achieve a better understanding of role of $Nb_{Li}$ in the lithium niobate crystals and explain its double nature (paramagnetic and diamagnetic). It appears that this defect produces a shallow level in the bandgap at a depth of about 1.7 eV absorbing in the near infrared. This point is better clarified in chapter 2 in the framework of the polaron model.

### 1.2.2. Extrinsic defects

It is a common practice to introduce dopants into metal oxides to improve their technological performance and numerous examples are available from the areas of sensors, electronics and optoelectronics. In particular in lithium niobate an extrinsic defects consists in any other elements out of Li, Nb and O that can enter in the crystal during the growth or subsequent treatments. In order to understand the precise role that the dopant plays in modifying the properties of the oxide the primary information required is its exact location in the host lattice. In principle, these ions might occupy either of three available octahedra sites (Li, Nb, and empty octahedron) or even interstitial sites. However, according to the data obtained with EXAFS, EPR, ENDOR or RBS technique, the impurity ions independently of their charge state are localized on the Li sites. The only ion which unambiguously occupies the $Nb^{5+}$ site in $LiNbO_3$, is $Ta^{5+}$ [26].

Charge transport processes in LN are strongly influenced by extrinsic defects, as determined by the marked sensitivity of photorefractive effect to the presence of impurities. Concerning this, the dopants usually employed can be divided into two categories:

- materials which increase the resistance to the optical damage, as Mg, Zr, Zn and Hf, whose role is to increase the material conductivity [1]; the first optical-damage-resistant composition found was $LiNbO_3 : Mg$, for which it was detected a critical concentration of about 5 mol% MgO for the congruent melt, referred to as a *threshold*, above which the optical damage drastically falls off by more than two orders of magnitude [27];

- dopants enhancing the photorefractive properties of the crystal, as Mn, Cu, Fe, among which the latest one is the most widely used because the most strongest photovoltaic active impurity. In this case the role of the impurities is bivalent, depending on their oxidation state: on one hand they act as photo-active donor centres (reduced impurities), on the other they decrease the material conductivity (oxidized impurities).

Pure lithium niobate crystals are transparent in the near-IR, the visible and the near-UV region up to 3.8 eV, but iron doping provides new energy levels in the middle of

the band gap, in the visible range of the absorption spectrum. This strong broad band is responsible for the photo-excitation of free electrons from iron deep level, a necessary condition for the realization of the photorefractive effect. Thanks to its important role iron has been intensively studied and all microscopic parameters, as position, charge state, optical absorption etc. are available from literature. The Fe impurity exists in $LiNbO_3$ only in two valence states $Fe^{2+}$ and $Fe^{3+}$, and these states represents respectively donors and acceptors centres in photorefractivity. Site-selective investigation of site symmetry and site occupation of iron in Fe-doped lithium niobate crystals had been studied for example. by T. Vitova *et al.*[28], revealing that $Fe^{2+}$ and $Fe^{3+}$ site symmetries and positions in the LN matrix are very similar, i.e. the $Fe^{2+}$ and $Fe^{3+}$ atoms are both octahedral coordinated by six oxygen atoms and both occupy the Li site.

Once the iron concentration ($N_{Fe} = N_{Fe^{2+}} + N_{Fe^{3+}}$) is chosen in the crystal growth procedure, it is possible to change the ratio $N_{Fe^{2+}}/N_{Fe^{3+}}$ (reduction degree) by oxidation or reduction processes, allowing a full decisional power on this parameters. As this dopant controls the photoconductivity and the photogalvanic effect it is important to give a precise estimation of its concentration and of the concentration of its two charge states: the optical absorption technique is a great candidate to absolve this purpose. (see section 4.3.1) The first characterization of the optical absorption processes in bulk $Fe : LiNbO_3$ samples was realized by Clark *et al.* [29] and subsequently formalized by Dischler *et al.* [30]. In particular, in this work the ordinary optical absorption at 532 nm is used to determine the $Fe^{2+}$ absolute concentration, as proposed for bulk Fe : LN by Berben *et al.* [31], whose experimental results lead to the following cross section:

$$\sigma_{532nm} = (3.95 \pm 0.08) \cdot 10^{-18} cm^2$$

The $Fe^{3+}$ concentration can be obtained as difference between $N_{Fe}$ and $N_{Fe^{2+}}$ assuming known the total Fe concentration or, as firstly reported by *Ciampolillo et al.* [32], by exploiting the isosbestic point at 342 nm found in Fe-diffused lithium niobate samples. Indeed, it was demonstrated that the absorbance at 342 nm is proportional only to the total iron regardless its reduction degree.

Typical concentration of intentional iron doping do not exceed 0.1 mol% because, as demonstrated by Peithmann *et al.* [33], higher concentrations lead to a degradation of photorefractive properties. However, Fe is also often encountered as a contaminant after the growth process, with a typical concentration that in the best cases is of few ppm.

## 1.3. Permittivity and refractive indices

In anisotropic crystals, as it is the case for LN, the relationship between the electric displacement $\mathbf{D}$ and the electric field $\mathbf{E}$ is tensorial and can be written as $\mathbf{D} = \hat{\epsilon}\,\mathbf{E}$

where $\hat{\epsilon}$ is the second-rank permittivity tensor. Permittivity is often given in terms of the permittivity of the vacuum $\epsilon_0$, obtaining the so-called relative permittivity or dielectric constant $\hat{\epsilon_r}$ and in this way $\hat{\boldsymbol{\epsilon}} = \epsilon_0 \hat{\boldsymbol{\epsilon}_r}$. Due to the crystallographic structure and the symmetry properties of lithium niobate, its permittivity tensor, in the orthogonal cell, can be represented by a $3 \times 3$ matrix with the form:

$$\hat{\boldsymbol{\epsilon}_{\boldsymbol{r}}} = \begin{pmatrix} \epsilon_{11} & 0 & 0 \\ 0 & \epsilon_{11} & 0 \\ 0 & 0 & \epsilon_{33} \end{pmatrix} \tag{1.3.1}$$

where it is possible to notice that only the diagonal elements are not-zero and that the permittivity has the same value for any electric direction perpendicular to the c-axis. The temperature dependence of the tensor is not trivial [34] as reported for exemple for $\epsilon_{33}$ in figure 1.3.1. It exhibits a continuous decrease while the temperature decreases and it converges to steady values of $\epsilon_{33} = 25.4 \pm 0.1$ below 50 K. The compositional dependence is taken into account in relation to the experimental measures reported by Turner *et al.* [35]. In the melting ratio range from [Li] / [Nb] = 0.852 to [Li] / [Nb] = 1.083 they found that $\delta\epsilon_3/\epsilon_3 = -0.075$.

At optical frequencies the permittivity of a material is usually described in terms of its refractive index. In particular lithium niobate presents two refractive indices, an extraordinary one ($n_e$) and an ordinary one ($n_o$), which refer respectively to optical beams polarized parallel to the z -axis and to the x or y axes of the crystal respectively. Their dependence on temperature, light wavelength and composition of the material is taken into account in a generalized Sellmeier equation proposed by Schlarb and Betzler [36]. In particular the Schlarb's approach is valid not only for pure $LiNbO_3$ crystals, but also in the case of doping with optical damage-resistant ions, allowing to exploit the refractive indices as a sensitive method to determine the composition of the material.

## 1.4. Pockels effect

The Pockels effect, named also linear electro-optic effect, is a second order process, discovered in 1899 by Friedrich Pockels. It consists in a linear modification of the refractive index when the material is exposed to an electric field. Due to its linear nature in the electric field, this effect can occur only in non centro-symmetric material, as $LiNbO_3$. This effect is usually described in term of the optical indicatrix, i.e. an ellipsoid surface whose central section is perpendicular to the direction of propagation of the incident beam and whose principal axes are identified as the refractive index of the material, according to the polarization of the propagating beam. The behaviour of the indicatrix can be represented as a power series of the electric field **E**

$$\triangle \left(\frac{1}{n^2}\right)_{ij} = \sum_{k=1}^{3} r_{ijk} E_k + \sum_{k,l=1}^{3} s_{ijkl} E_k E_l \tag{1.4.1}$$

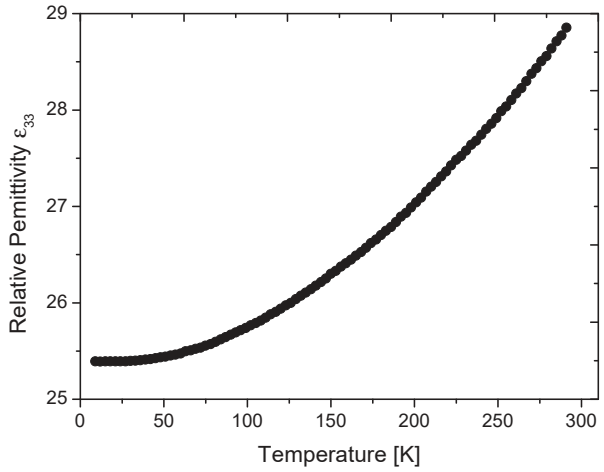


Figure 1.3.1.: Unclamped relative permittivity $\epsilon_{33}$ of congruent lithium niobate covering the temperature range of $7\,K < T < 300\,K$ at $f = 5760\,\text{Hz}$ and $\lambda = 632.8\,\text{nm}$ [34].

where $r_{ijk}$ and $s_{ijkl}$ are are the coefficients relative to the linear and quadratic electro-optic effects, usually named respectively Pockels effect and Kerr effect. Although lithium niobate presents high linear electro-optic effect, higher-order terms can generally be neglected, because in this material no quadratic electro-optical effect can be significantly observed for applied electric fields up to $65 \cdot 10^6\,\text{V/m}$ [37]. Due to the anisotropy of the material, Eq. 1.4.1 assumes a tensorial form and in the Voigt notation [1] the linear electro-optic tensor $\hat{\mathbf{r}}$ results:

$$\hat{\mathbf{r}} = \begin{bmatrix} 0 & -r_{22} & r_{13} \\ 0 & r_{22} & r_{13} \\ 0 & 0 & r_{33} \\ 0 & r_{42} & 0 \\ r_{42} & 0 & 0 \\ -r_{22} & 0 & 0 \end{bmatrix} \tag{1.4.2}$$

Thus, the electro-optic effect in $LiNbO_3$ can be described by only four independent coefficients. In particular for an electric field aligned along the optical axis of the material, the change in the refractive index at first order is provided by the following relation:

$$\triangle n_e = -\frac{1}{2} n_e^3 r_{33} E_z \tag{1.4.3}$$

$$\triangle n_o = -\frac{1}{2} n_o^3 r_{13} E_z$$

[1] When the tensor is symmetric ($r_{ijk} = r_{ijk}$), as in the case of LN, the first two indices $ij$ can be contracted in only one indices $p$ so that $r_{ijk} = r_{pk}$ according to the convention $ij = 11 \rightarrow p = 1$, $ij = 22 \rightarrow p = 2$, $ij = 33 \rightarrow p = 3$, $ij = 23 \rightarrow p = 4$, $ij = 32 \rightarrow p = 4$, $ij = 13 \rightarrow p = 5$, $ij = 31 \rightarrow p = 5$, $ij = 12 \rightarrow p = 6$ and $ij = 21 \rightarrow p = 6$.

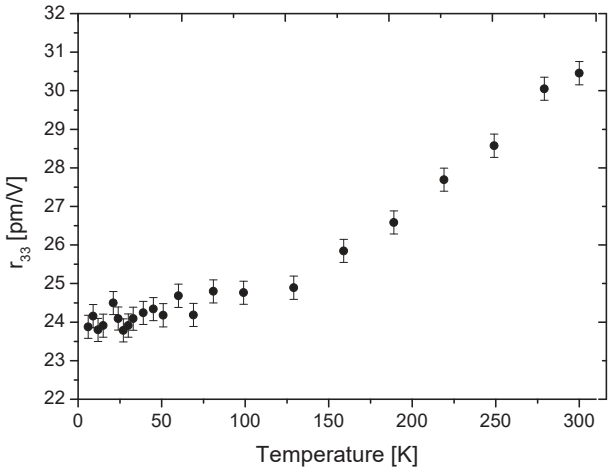


Figure 1.4.1.: Unclamped Pockels coefficient $r_{33}$ of congruent lithium niobate covering the temperature range of $7\,K < T < 300\,K$ at $f = 5760\,\text{Hz}$ and $\lambda = 632.8\,\text{nm}$ [34].

where $n_o$ and $n_e$ are respectively the ordinary and the extraordinary refractive index of the material. The only electro-optic coefficient playing an active role in this work is the $r_{33}$, equal to $r_{33} = 30\,\text{pm/V}$ at room temperature for congruent materials [20], because only extraordinary polarized light is employed, as it will be shown below in section 5.2.2. Recently is was measured by *C. Herzog et al.* [34] that the linear electro-optic coefficient $r_{33}$ has a temperature dependence as shown in figure 1.4.1 where it can be seen that it decreases by 20% upon cooling the LN crystal from room temperature to 10 K, converging to a steady value of $r_{33} \approx 24 \pm 0.7\,\text{pm/V}$ below 50 K. The electro-optic tensor shows also a dependence on the crystal composition, as reported by *Toro et al.* [38] and by *Mendez et al.* [39]. They conducted the experiment on two different near-stoichiometric samples ($[\text{Li}]/[\text{Nb}] = 0.992 \pm 0.002$) grown with the same technique used for the samples of this thesis, i.e. by mixing congruent $LiNbO_3$ powder with a 6% $K_2O$ flux, obtaining respectively $r_{33} = 29.4 \pm 0.2\,\text{pm/V}$ and $r_{33} \approx 29.5\,\text{pm/V}$ at $\lambda = 632.8\,\text{nm}$. It is interesting to notice that identical measure on near-stoichiometric samples grown with different techniques leads to complete different results. For example in [40], where the sample is grown from a 58.0 mol% $Li_2O$ melt by the continuous-charge double-crucible Czochralski method, the $r_{33}$ instead of decrease increases to $r_{33} = 38.3 \pm 1.4\,\text{pm/V}$.

## 1.5. Photogalvanic effect

The photogalvanic effect (PG), known also as bulk photovoltaic effect (BPVE), is a dominating charge transport mechanism initiating the photorefractive effect in materials such as $LiNbO_3$ or $LiTaO_3$, enabling a variety of optical applications, including

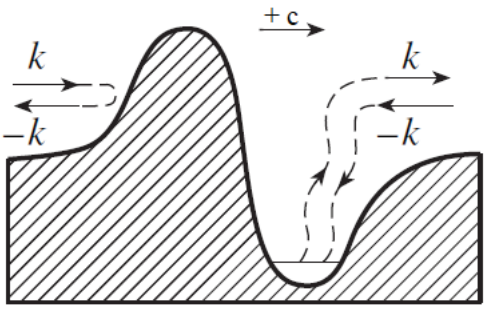


Figure 1.5.1.: Excitation of impurity centres with an asymmetric potential by an uniform illumination results in an asymmetric momentum distribution for non-equlibrium electrons (or holes). This, in turn, results in the appearance of the photovoltaic current along the $\hat{c}$ direction of the crystals [41].

holographic data storage, phase conjugating mirrors, optical filters, etc. [3]. It was observed the first time in lithium niobate in 1974 by *Glass et al.* [2], who noticed that when this crystal is exposed to uniform light a steady short-circuit current appears ($j_{pg}$), proportional to the light intensity and to the absorption coefficient of the material $\alpha$. Furthermore according to Glass the proportionality constant, known as *Glass constant* ($k_G$), depends on the nature of the absorbing centre and on the wavelength. According to his explanation, the photo - excited charge has a higher probability of being ejected in the $+c$ direction rather than in the opposite direction $-c$ due to asymmetry of the polar lattice, as it can be seen in figure 1.5.1. Therefore, electrons excited from the donor defect into the conduction band would exhibit a net drift along the positive $c$ axis (axis of spontaneous polarization) without being driven by a macroscopic electric field or a concentration gradient. This microscopic process results in a net macroscopic current of the order of $10^{-7}\,\mathrm{A/m^2}$ under cw illumination of about $300\,\mathrm{W/m^2}$ and for moderately iron doped samples ($[Fe] \sim 0.05\mathrm{mol}\%$).

More rigorously, the PG effect is described by a third-rank tensor $\beta_{ikl} = \beta^*_{ikl}$, expressing the details of the response of the photogalvanic current $j_{pg}$ to the light intensity I, through

$$j_{pg,\,i} = \beta_{ikl} e_k e^*_l \cdot I \tag{1.5.1}$$

where the components $e_k$, $e^*_l$ represent unit vectors of the light electric field.. The tensorial nature of the PG was first verified by Fridkin and Magomadov [42]. The crystal symmetry makes the $\beta_{ikl}$ tensor to have only four non-vanishing independent components [3]:

$$\begin{gathered} \beta_{zzz} \\ \beta_{zyy} = \beta_{zxx} \end{gathered} \tag{1.5.2}$$

$$\begin{gathered} \beta_{yyy} = -\beta_{xxy} = -\beta_{xyx} = -\beta_{yxx} \\ \beta_{xxz} = \beta^*_{xzx} = \beta_{yzy} = \beta^*_{yyz} \end{gathered} \tag{1.5.3}$$

For the elements in Eqs. 1.5.2 and 1.5.3, $z$ is directed along the $c$ axis, with $y$ perpen-

dicular to $c$ (within a glide mirror plane) and $x$ perpendicular to both in a right-handed system. The elements in Eq. 1.5.2 refer to $j||c$, and those in Eq. 1.5.3 to $j\perp c$.

For linearly polarized light, only the real part of $\beta_{ikl}$ contributes to $j_i$ and therefore the corresponding tensor is symmetric in the $k$, $l$ indices (linear photovoltaic effect or LPG).

Schirmer *et al.* [43], from data presented by Festl *et al.* [44], derives $\beta_{zzz} = 40{\cdot}10^{-9}1/V$ as having the same value of $\beta_{zxx} = 40\cdot10^{-9}1/V$, for a $Fe^{2+}$ concentration of $6\cdot10^{18}\,cm^{-3}$ and a photon energy of 2.48 eV. The values of both these elements increase linearly with energy up to 2.7 eV, above which $\beta_{zxx}$ starts to dominate slightly. The value of $\beta_{yyy}$ is $2\cdot10^{-9}1/V$ at 2.48 eV, rising to $6\cdot10^{-9}1/V$ at 3.0 eV. From data presented by Karabekyan [45] the value of $\beta_{xxz}$ can be derived to be about $0.8\cdot10^{-9}1/V$ for the $Fe^{2+}$ concentration investigated by Festl *et al.* In summary, both $\beta_{zzz}$ and $\beta_{zxx}(=\beta_{zyy})$, with $j||c$, are comparatively large and of nearly the same size, while $\beta_{yyy}$ and $\beta_{xxz}$, with $j\perp c$, are smaller by one to two orders of magnitude. Karabekyan has also investigated the dependence of these four significant tensor components on photon energy: an identical dispersive behaviour was found.

From the value of the tensor, nearly the same current is produced with a linearly polarized light along any one of the three axis of the crystal, leading to a 1D problem. In particular, during the experimental measurements described in section 5.2 the external light is chosen linearly polarized along the $y$ direction. In this situation $j_x = j_y = 0$ and $j_z = \beta_{zyy}E_yE_y^*$.

In the case of a 1D problem, equation 1.5.1 can be rewritten according to the Glass phenomenological formula:

$$j_{pg} = k_G\alpha I \tag{1.5.4}$$

In this approximation equation 1.5.4 can be also re-expressed in terms of more useful experimental quantities by the formula:

$$j_{pg} = \frac{q\alpha I}{h\nu}\phi L_{pg} = qsN\frac{I}{h\nu}\phi L_{pg} \tag{1.5.5}$$

where $q$ is the charge of the photo-excited carriers, $\alpha = sN$ is the absorption coefficient (with $s$ the cross section and $N$ the concentration of the photogalvanic centres, respectively), $I$ is the light intensity and $h\nu$ is the photon energy. The parameter $L_{PG}$ has the dimension of a distance and its physical meaning is the average distance travelled by the photo-excited carriers before stopping contributing to the current. Experiments on $LiNbO_3$ suggest a very strong connection of photogalvanic effect to the nature of the impurities, as it is outlined in paragraph 2.2, in particular for iron doping. Typical values of $L_{pg}$ for iron doped samples were found by Glass *et al.* [2] of $L_{pg} = 0.8$ Å from measurements at $\lambda = 514$ nm and $L_{pg} = 1.3$ Å at $\lambda = 473$ nm. $\phi$ is the efficiency of the process, i.e. the probability of creating an electron *contributing* to the PG effect by an absorbed photon. This factor was introduced in the early days of photorefractivity to explain the apparent contradiction between the measured values of the space charge

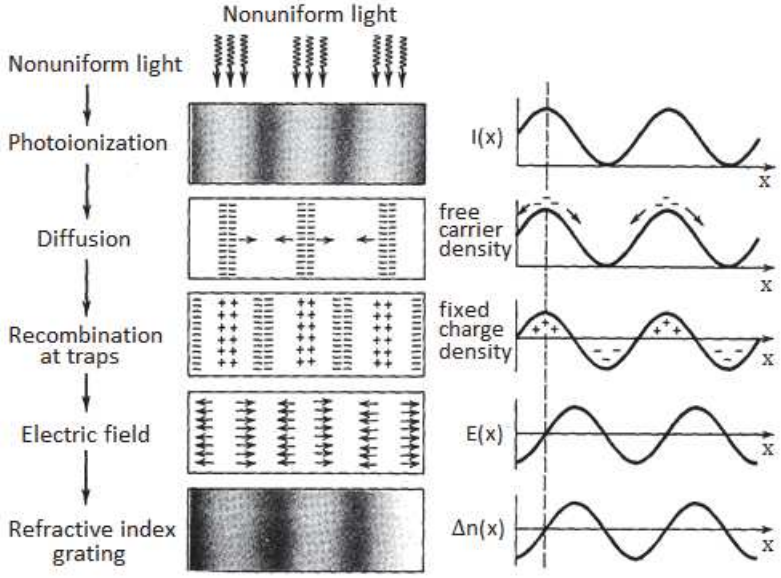


Figure 1.6.1.: Representation of the main steps creating the photorefractive effect [48]. The first step, the directional photoionization, is depicted in more detail in figure 1.5.1.

field and the mobility-lifetime product of photoexcited carriers. Its physical meaning, for the moment purely phenomenological, will be better discussed in section 2.2.

## 1.6. Photorefractive effect

Electro-optic photoconductive materials exhibit a peculiar phenomenon, known as photorefractive effect (PR), with a variety of applications in photonics and optoelectronics [46, 5]. It consists in a refractive index variation of the material exposed to a non homogeneous light pattern. In lithium niobate this variation is the result of mainly three steps , as shown in figure 1.6.1. The first one is the directional photo-ionization of electrons, i.e the photogalvanic effect (see section 1.5), which produces as second step a diffusion and a redistribution of the electric charge inside the material building up subsequently a strong space charge field $E_{SC}$ in the material. The third step arises thanks to the Pockels effect, because the internal field in turn modifies the refractive index of the material, as described in paragraph 1.4. This effect was observed for the first time in 1966 by Ashkin *et al.* [47] in $LiNbO_3$ and in $LiTaO_3$ when they observed that any beam propagating in the crystal gave origin to a slowly-growing refractive index variation distorting the wave front of the beam itself.

The first model of the photorefractive effect was proposed by Chen [48] in 1968 where he highlighted that the index variation in a material submitted to radiation can be exploited to record information carried by the light signal. He proposed a model based on the band transport, where the photo-induction mechanism is explained. This model consider a photorefractive material presenting donor impurities, named $N_D$, sufficiently

far away from the conduction band, so that the thermal excitation can be neglected. A part of these impurities, having a density $N_D^+$, is ionized, so that they are apt to accept a moving charge. The generated charges moves in the conduction band, until they are trapped at another ionized impurity elsewhere in the crystal. If the charge is trapped in an illuminated zone it can be again photo-excited and the mechanism continues as long as it is trapped in a dark zone. In this way charge transfer from illuminated to dark zone is realized and this new charge distribution generates an internal static electric field in turn modifying the refractive index via the electro-optic effect. This donor impurity is a transition metal which act as photorefractive centres, such as the iron. Its two possible valence states, $Fe^{2+}$ and $Fe^{3+}$, are deep states in the band gap which can behave as donor and acceptor respectively for the free charge carriers. The efficiency of this effect, i.e. the $\triangle n$ achieved, depends on the concentration of the two valence states, as outlined in [49]. Since the photorefractive effect in $Fe : LiNbO_3$ crystals is one of the fundamental techniques employed in this thesis, the role of this extrinsic defects and its effect will be more deeply explained during the work.

The charge carriers that contribute to the photorefractive effect can be electrons or holes. Not always one of them dominates over the other one, so that they can both contribute to the charge transport as demonstrated by Orlowsky and Krätzig [50]. The contribution of electrons and holes depends not only on the dopant used, but also on its reduction degree and on the wavelength of incident light. In the case of this thesis, in which a green laser light is exploited and only iron doping is considered, electrons can be considered the predominant charge carriers involved in the transport mechanism. This is rigorously true for continuous illumination measurements (see chapter 5.2, instead for transient measurements, made at high light intensities, also holes may play a significant role (see chapter 5.1).

The magnitude of this effect is largely determined by the values of the electro-optic coefficients that convert the space charge field into a refractive index change. Under suitable conditions, it leads to observable effects in the range of $\triangle n \sim 10^{-5}$ for intensities down to $mW/cm^2$, indicating that electric fields of the order of $10^4 V/m$ are built in the crystal. On the other hand, the response time is determined by the time needed to build up the space-charge field so it is related to light intensity and carrier mobility. Typical values ranges from few seconds to tenths of minutes. The photorefractive effect is reversible because it can be completely erased by intense uniform incoherent illumination restoring the initial charge configuration in a temporal window comparable to the one needed for its creation. This properties is highly exploited in this work permitting to perform repeated experimental measures in the same samples but eventually under different physical condition, as temperature or illumination.

## 1.7. Kukhtarev-Vinetskii model for charge transport

The equations used at present for describing charge transport, and by extension photorefractive phenomena, are overwhelmingly based on the work of the Kiev group [8] leading to the well known Kukhtarev's model. This is believed to represent the best compromise between the complexity of real crystals and the simplicity of description. A simpler phenomenological description based on the spatial symmetry of the nonlinear medium has been later formulated, with the great advantage that its equations use a relatively small number of phenomenological parameters [9]. In fact, as discussed in the latter work, all the microscopic details of the transport process can be embedded in few phenomenological parameters which are sufficient to provide a self-consistent mathematical description of photoexcitation, conduction and space charge field build up. On the other hand these two models do not give any indication on how those parameters depend on the structure of the sample. For instance, the well-known fact that the charge mobility depends strongly on the crystal Li/Nb ratio cannot be explained. Moreover the values of the mobility parameter $\left(< 10^{-4}\,\mathrm{cm}^2/\mathrm{Vs}\right)$ is way too low to be compatible with any conduction - band state. Hopping models based on the concept of localized carriers, like the one detailed in this thesis have been proposed as an alternative approach. In CW experiments, where it is possible to neglect two-photon processes, and assuming that charges follows normal diffusion laws, band or hopping transport mechanism leads to similar descriptions, as it was demonstrated by Feinberg *et al.*[51]: in this sense the mathematical framework of band-like model can be kept to calculate the evolution of the space charge field, while other more correct microscopic models are needed to determine the value of the macroscopic parameters entering into the phenomenological equations. However, as it will be detailed in the rest of this thesis, if different hopping centres are considered, it may happen that normal diffusion laws breaks down, which requires to review the equations used for transport description.

The Kukhtarev–Vinetskii equations, known also as one-centre model, describe the photorefractive effect provoked by an illumination profile in the low intensity regime into iron-doped LN and may be written as:

$$\frac{\partial N^+}{\partial t} = s\phi N \frac{I}{h\nu} - \gamma N^+ n_e \tag{1.7.1}$$

$$\frac{\partial n_e}{\partial t} = \frac{\partial N^+}{\partial t} + \frac{1}{e}\nabla \cdot \boldsymbol{j} \tag{1.7.2}$$

$$\boldsymbol{j} = e\mu_e n_e \boldsymbol{E} + \mu_e k_B T\, \nabla \boldsymbol{n}_e + \boldsymbol{j}_{pg} = \boldsymbol{j}_{drift} + \boldsymbol{j}_{diffusion} + \boldsymbol{j}_{pg} \tag{1.7.3}$$

$$\nabla \cdot \mathbf{E} = \frac{e}{\varepsilon\varepsilon_0}\left(N^+ - n_e\right) \tag{1.7.4}$$

Here $n_e$ is the concentration of photoelectrons, $N^+$ and $N$ are the concentrations of ionized and non-ionized centres, in our case $Fe^{3+}$ and $Fe^{2+}$ respectively, $s\phi$ is the absorption cross section times the process efficiency $\phi$ for the donor centre ($Fe^{2+}$) (see

Section 1.5) and $\gamma$ is the recombination constant. The first two equations of the set describe the carrier balance, the third equation gives the current density, and the last one expresses Gauss's law.

Concerning equation 1.7.3:

- the first term correspond to the Ohmic current arising under external or internal electric field

$$\boldsymbol{j}_{drift} = e\mu_e n_e \boldsymbol{E} = \sigma\left(\boldsymbol{E}_{ext} + \boldsymbol{E}_{int}\right) \tag{1.7.5}$$

- the second term represents the diffusion transport of photo-carriers occurring under a spatially non uniform illumination, which leads to a non-uniform density of mobile charges;

$$\boldsymbol{j}_{diffusion} = \mu_e k_B T \nabla \boldsymbol{n}_e \tag{1.7.6}$$

- the third one is the photogalvanic contribution already mentioned in section 1.5:

$$\boldsymbol{j}_{pg} = qsN\frac{I}{h\nu}\phi L_{PG}\hat{c} \tag{1.7.7}$$

.

The four equations describe the spatial and temporal evolution of the internal electric field that develops as a consequence of a stationary but spatially modulated illumination profile. The process is based on the excitation of electrons from $Fe^{2+}$ to the conduction band, after moving by photogalvanic effect, diffusion and drift, finally re-trapped elsewhere by $Fe^{3+}$. This model assumes that only electron contribute to the transport and two approximations are widely used to derive expressions of the photorefractive response in the low-intensity limit, namely the terms $\partial n_e/\partial t$ (second equation) and $n_e$ (fourth equation) may be neglected. The approximation exploits the smallness of the electron lifetime $\tau_e$ in comparison with the characteristic time of the photorefractive response. Usually in the low intensities regime this condition is very well justified. In addition the model is valid for moderate iron doping, indeed for iron concentration superior to $N_{Fe} = 20 \cdot 10^{24}\,m^{-3}$ the refractive index variation is no more linear with the $Fe^{3+}$ concentration [33]. The solution for this problem proposed by Nee *et al.* [52] considered that in the case of strong doping there is a direct migration from $Fe^{2+}$ to $Fe^{3+}$ by tunnelling, situation not consider by Kukhtarev equations. We further note here that 1.7.1, 1.7.5 and 1.7.6 are derived assuming normal diffusive transport. This point will be further addressed in Chapter 8.

A rigorous treatment of the photorefractive effect with the set of four equations could be done only numerically, indeed they are non-linearly coupled and in general difficult to solve without further simplifying assumption. It is possible to predict analytically the result only in some specific cases which, in spite of the simplicity of assumptions, are interesting to study to find a minimum set of parameters governing the phenomena. For example the model developed by Zozulya and Anderson [53] solves the problem

for a static Gaussian beam focused at the surface of a Fe:LN sample, with the beam polarized along the z direction and propagating along the x-axis of the crystal. In this case the analytical solution predicts a general characteristics, i.e. the refractive index variation in the illuminated zone corresponds to a decrease of the index with respect to the bulk value. Another interesting case which allows to solve equations is the one for uniform spatial illumination [54]. In this case equation 1.7.3 can be simplified in the following way:

$$\boldsymbol{j}(t) = \sigma \boldsymbol{E}(t) + \beta N I \hat{c} = \boldsymbol{j}_{drift} + \boldsymbol{j}_{pg} \tag{1.7.8}$$

where $\beta = qs\frac{\phi}{h\nu}L_{PG}$ and $\sigma = e\mu_e n_e$ is the internal conductivity. In general the latter is the sum of two term $\sigma = \sigma_{ph} + \sigma_{dark}$, respectively the photo- and the dark conductivity, however the second term has an active role in transport measurement only in regime of high temperature, not discussed in this thesis work, so this term can be neglected [52]. In this approximation of uniform spatial illumination is possible also to study in a simple way the time development of the electric space charge field, which in a scalar approximation assumes the form of a saturated exponential time evolution:

$$E(t) = E_{sat}\left(1 - e^{-t/\tau_d}\right) \tag{1.7.9}$$

where the time constant $\tau_d$, the so-called dielectric relaxation time, is given by:

$$\tau_d = \frac{\varepsilon\varepsilon_0}{e\mu_e n_e} = \frac{\varepsilon\varepsilon_0}{\sigma_{ph}}. \tag{1.7.10}$$

The space charge field consequently evolves in a time scale of $\tau_d$, which for LN, is in the order of tens of seconds at room temperature, and one hour around $T = 80\,\mathrm{K}$.

To evaluate $\sigma_{ph}$, generally one starts from Eq. 1.7.1 and considers that in quasi-equilibrium condition $\frac{\partial N^+}{\partial t} \approx 0$, from which $n_e = \frac{s}{\gamma}\frac{N}{N^+}\phi\frac{I}{h\nu}$. Substituting in $\sigma$ and neglecting the dark conductivity, one gets:

$$\sigma_{ph} = e\mu_e \frac{s}{\gamma}\frac{N}{N^+}\phi\frac{I}{h\nu} = e\mu_e \tau s N \phi \frac{I}{h\nu} \tag{1.7.11}$$

where $\tau^{-1} = \gamma N^+$ is the carrier lifetime, not to be confused with the dielectric relaxation time $\tau_d$. Eqs. 1.7.10 and 1.7.11 show that the time constant for the build up of the space charge field is inversely proportional to the intensity of the optical field.

The value of $E_{sat}$ can be derived by the stationary situation, when the photogalvanic current is exactly counterbalanced by the drift current, so that the total current $\boldsymbol{j}$ of equation 1.7.3 is zero. The electric field in this condition reaches its maximum value that, according to eqs. 1.7.7 and 1.7.11 is given by: :

$$E_{sat} = \frac{j_{pg}}{\sigma_{ph}} = \frac{L_{pg}}{\mu_e \tau} \tag{1.7.12}$$

Typical values of the saturation space charge field are in the range $10^6 - 10^7\,\mathrm{V/m}$. It

should be noted that the saturation space charge field does not depend on the light intensity, nor on the charge generation efficiency $\phi$ .

Another interesting solution of the Kukhtarev's model is the one discussed in [55] where the light profile is supposed to be a 1D Gaussian beam along the $x$ direction, but invariant with respect to the $y$ and $z$ direction, i.e. with intensity distribution:

$$I(x) = I_0 \exp\left(-\frac{x^2}{2w^2}\right) \tag{1.7.13}$$

This case corresponds to a Gaussian beam with largely different diameters in the $x$ (thin) and $y$ (thick) directions, propagating along the $z$ direction and assuming that the diffraction of the beam can be neglected, which is the case when the crystal thickness is smaller than the Rayleigh range of the beam. The crystal's c-axis is oriented parallel to the gradient direction of the Gaussian beam, i.e. the $x$ axis. The spatial extent of the Gaussian beam along the direction perpendicular to the c-axis is assumed to be infinite. The polarization of the light beam is assumed to be perpendicular to the crystal's c-axis. Additionally, the crystal is short-circuited to avoid parasitic charge buildup at the surfaces. In this geometric configuration and in the steady-state situation the electric field assumes the form:

$$E(x) = -E_{sat}\frac{I(x)}{I(x) + I_D} \tag{1.7.14}$$

where $I_D$ is the dark intensity, whose main source in this case is thermal excitation of mobile charges, while $I$ is the intensity profile expressed by formula 1.7.13. Through the linear electro-optic effect, the crystal's refractive index perturbation follows the saturated Kerr-type non-linearity

$$\triangle n(x) = \triangle n_{sat}\frac{I(x)}{I(x) + I_D} \tag{1.7.15}$$

where $\triangle n_{sat} = n^3 r E_{sat}/2$. Equation 1.7.15 displays another important property of the obtained refractive index profile: the saturation. If $I\,(x) \ll I_D$ in 1.7.15 the refractive index contrast is proportional to the illumination profile, $\triangle n(x) = \triangle n_{sat}\frac{I(x)}{I_D}$. On the contrary, if $I\,(x) \gg I_D$ the refractive index profile saturates to the limiting value $\triangle n_{sat}$.

An analytical solution of the model can be obtained also in the case of an external sinusoidal external light. The complete mathematical description can be found in [56].

# 2. Polarons in Lithium Niobate

The polaron is one of the main concept on which the charge transport theory of polar oxide materials is based. This concept was introduced the first time by L. D. Landau in 1933 to explain new optical properties exhibited by alkali halides [10]. Landau observed that these materials are characterized by a strong electron-phonon interaction, thanks to which the charge carrier (electron or hole) can distort the surrounding lattice via Coulomb and short-range interactions. The displacement of the surrounding ions leads to a potential well, in which the free carrier can localized. Since this type of electron-phonon coupling was first considered in ionic (polar) materials, the quasi-particle composed of the self-trapped carrier and the accompanying ionic displacements was called *polaron*. Nowadays this term is used in a wider scope, and one may associate polaron with the fact that the surrounding lattice is "polarized" by the carrier's charge.

Depending on the spatial range of the interaction it has to be distinguished between *large* and *small* polarons [12]. In the former case the radius of the displacement pattern is considerably larger than one lattice constant. In the second case, with the increasing of the coupling strength, the polaronic radius shrinks, restricting the potential well to a single lattice site, so that the electron density does not extend beyond a trapping cation site. This latter object is then called a *small polaron*. While the movement of a large polaron may be described like the one of a free electron in the conduction band with an increased effective mass [57], small polarons merely move by hopping between nearest neighbour sites.

Small polarons are the only ones present in lithium niobate at sufficiently high temperature, due to the strong electron-phonon interaction characterizing the material, for this reason the term polaron in this work refer uniquely to the small one. In LN they can be seen as localized defect states in the band gap, which can absorb the light releasing the trapped charge to higher energy levels under the Franck-Condon principle [58]. Upon favourable conditions they can move by thermally assisted jumps and diffuse in the material, even if very slowly since they only move when the surrounding lattice move. Furthermore, they can be captured by defects having an attractive or negative potential. The coexistence of all these process originates a peculiar transport phenomena influencing the charge transport phenomena and the optical properties of Lithium Niobate.

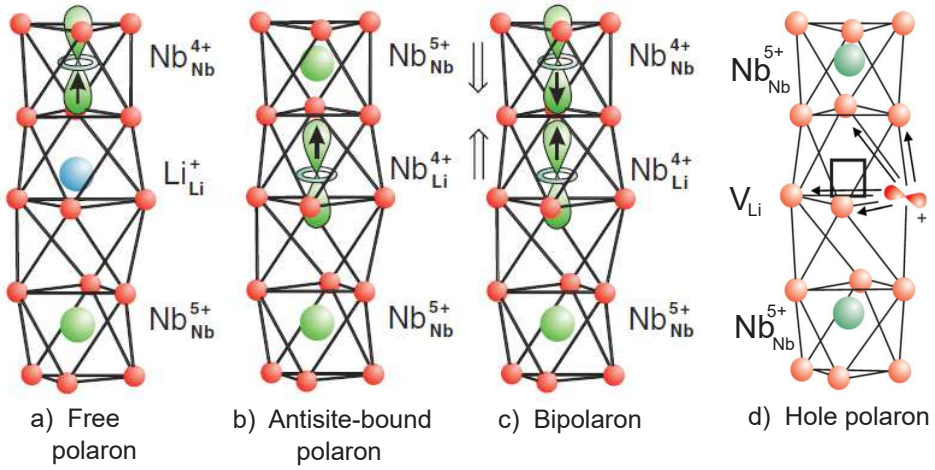


Figure 2.1.1.: Visualization of the orbital ground states of polarons in LN. a) one electron trapped in regular niobium site forming a free small polaron $Nb_{Nb}^{4+}$ b) one electron localized at the niobium antisite defect forming an antisite-bound polaron $Nb_{Li}^{4+}$. c) two electrons self trapped in a regular niobium site and in an antisite defect forming a bound bipolaron $Nb_{Li}^{4+}$ : $Nb_{Nb}^{4+}$. The two vertical double arrows indicate the relaxation of the Nb ions towards each other, increasing the bipolaron binding energy. d) hole self trapped at an oxygen ion in the vicinity of a $V_{Li}$, forming an hole polaron $O^{-}$.

## 2.1. Physics of small polarons

In order to deal adequately with the features of the different kind of polarons in lithium niobate, it is essential to understand their microscopic structures and the related physical properties [58]. The main features of this quasiparticle are described using Holstein's one-dimensional Molecular Crystal Model (MCM) [59]. A model of the real situation would have to describe the polaron localized at one cation site in a three-dimensional crystal by an appropriate relaxation of its neighbour ions. Despite of this, the MCM model employed a simpler arrangement where only two neighbours are assumed, forming a one-dimensional chain. Result of this 1D model can be sequentially applied to a more realistic 3D case using slight corrections.

### Free small polarons

Electrons self-trapped at regular $Nb_{Nb}^{5+}(4d^0)$ ions of the LN lattice forms the most simple polaron species, the *free small polaron* $Nb_{Nb}^{4+}$ (figure 2.1.1 a). It is the most shallow polaron state known in $LiNbO_3$ and it is characterized by a broad optical absorption band in the near infrared spectra range, centred at $M_F = 1.09\,\text{eV}$ (corresponding to a wavelength of 1280 nm) [60] immediately below the conduction band (see figure 2.1.5). It is interesting to point out that this energy peak is rather high, if compared with that of polarons in other oxide materials, e.g. $BaTiO_3$ (0.6 eV) or $TiO_2$ (0.7 eV), indicating that the coupling of free electrons to the LN lattice is extraordinarily strong.

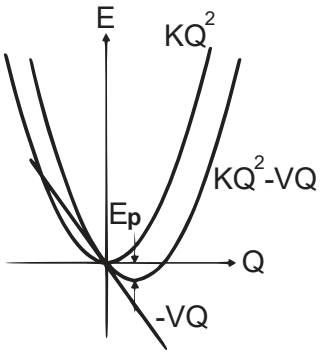


Figure 2.1.2.: Energy contribution to the stabilization of a small polaron.

Free polarons were identified initially only in samples doped with Mg or Zn above the optical-damage resistance threshold, through electrical measurements on the crystal photo-conductivity [60]. This type of doping indeed eliminates all antisite defects, essential condition to detect a free small polaron: if some antisite defect are present, the electron tends to be trapped there, forming a bound polaron, a more stable state compared to the free one [61].

According to MCM model, the polaron formation of a free electron on a regular Nb site can be depicted as shown in figure 2.1.2. The localization raises the kinetic energy of the electron and thus, to ensure the formation of the polaron, this energy must be overcompensated by an energy lowering. This is provided by the displacement of the neighbouring ions and, possibly, also by an additional long range Coulomb force. In this way the electronic energy is decreased, in the first order approximation, by $-VQ$, where $V$ is a phenomenological constant expressing the energy gain proportional to the deformation and $Q$ is an independent parameter describing the deformation. The energy paid to distort the lattice must be quadratic in the deformation, $KQ^2$. The total energy of the polaron, is thus expressed by the formula:

$$E = KQ^2 - VQ \tag{2.1.1}$$

The minimum of the energy occurs at $Q_{min} = V/2K$ and in this case the energy assumes the value:

$$E_{min} = \frac{-V^2}{4K} = -E_F. \tag{2.1.2}$$

defined as the so-called *polaron deformation-stabilization energy* (DSE).

In this condition the electronic and elastic energy are then respectively:

$$E^{ele}_{min} = -VQ_{min} = -\frac{V^2}{2K} = -2E_F \tag{2.1.3}$$

$$E^{ela}_{min} = KQ^2_{min} = \frac{V^2}{4K} = E_F \tag{2.1.4}$$

The optical absorption by a small electron polaron mainly consists in a charge transfer

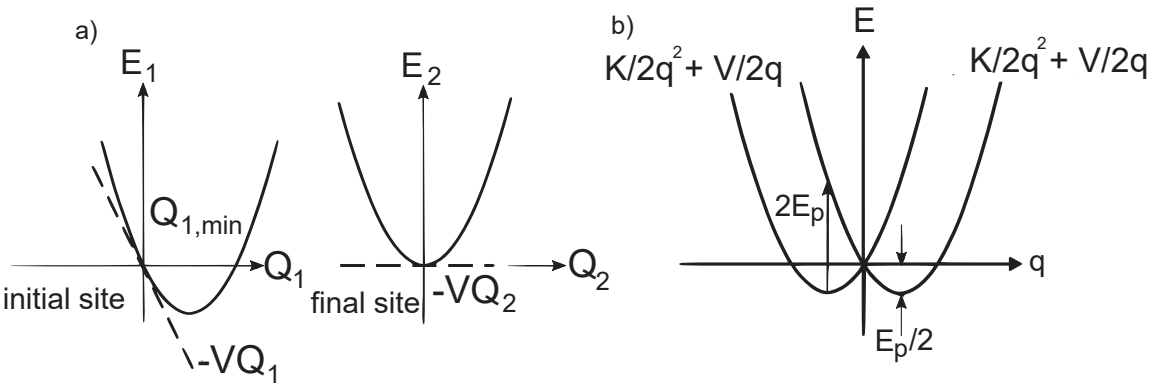


Figure 2.1.3.: a) Energy of the system electron + lattice. The electron is self-trapped at the initial cation site and light-induced charge transfer transitions occur to another cation site which is not distorted in the absence of electron. b) Scheme (a) with energies shown as depending on the relative coordinate q.

transition of the self-trapped electron to an equivalent site. This idea is presented in figure 2.1.3(a). In the initial site the lattice is distorted because of the presence the electron, but when light-induced charge transfer transition occurs, the electron is transferred to another cation site in the lattice, which is not distorted in the absence of the electron. In this vision the initial site can be modelled as a displaced oscillator, whereas the situation of the final site is represented by an unbiased oscillator, having the electronic energy equal to zero. The transition energy is thus only determined by the distortion at the initial site. On the basis of the simplifying assumption that the stabilizing distortion at the initial site does not influence the electron energy at the final one, the energy to be expended for the photon-induced electron transfer is: $E^{ele}_{final} - E^{ele}_{initial} = 0 - (-VQ_{min}) = 2E_F$. Finally, after the light-induced electron transfer to the new site, the lattice adjusts to the presence of the relocated electron. This is a spontaneous process which is not influenced by the absorbed photon. The corresponding absorption band is therefore centred around $M = 2E_F$, so from absorption measures it is possible to know the polaron energy, which in the case of free polarons is $E_F = 0.545\,\mathrm{eV}$. Moreover, by using a modelling typical of defect physics [58], the line-shape of the absorption band can be shown to be a Gaussian function, characterized by a half width at half maximum:

$$W^2 = 4E_F\hbar\omega_0 \ln(2) \tag{2.1.5}$$

where $\hbar\omega_0$ is the energy of the phonon mode associated to the lattice distortion of the polaronic effect. The shape of the predicted optical absorption of free small polarons is based on the assumption that the absorbed photon transfers the trapped electron from the ground state orbital at the initial site to an analogous ground state orbital at one equivalent final site. This approach however fails when higher-energy tails of the absorption band are considered, essentially because the final situation presents an increased density of states with respect to the starting one, due to the various possible

destination sites that the excited charge can choose to localize at. For this reason it is a common practice to fit only the low-energy half of the polaron absorption peak with a Gaussian function to measure the value of the unknown parameters $E_F$ and $\hbar\omega_0$. For free polarons, a standard value $\hbar\omega_0 = 0.1\,eV$ is assumed for polar oxides, from which one calculates the width $W_{theo} = 0.39\,eV$, almost identical with the observed one, $W_{exp} = 0.37\,eV$.

### Bound small polarons

If an electron (hole) is captured by a defect ion, positively (negatively) charged with respect to the replaced regular cation of the lattice, it is attracted locally by the extra potential of the defect. In addition a polaron-like stabilization by lattice distortion can occurs. We shall label such defects as *bound polarons*, if the optical absorption features are dominated by polaron-like transitions to next neighbours.

The extra attracting influence active in the case of a bound polaron causes a pre-localization of the carrier already before the lattice distortion sets in, so that the total energy of the polaron tends to be larger with compared to the free case. Furthermore, the defect-induced energetic inequivalent between the initial and final sites will reduce the intensity of the charge transfer transition, because the mixture of initial and final site states will be more asymmetric, leading to a greater activation energy of the process.

Examples for electron bound polarons in the case of $LiNbO_3$, are electrons bound to a $Nb_{Li}^{5+}$ antisite defect, forming $Nb_{Li}^{4+}$ (see figure 2.1.1 b) or localized in a $Fe^{3+}$ forming a $Fe^{2+}$. Spectroscopy measurements highlights that $Nb_{Li}^{4+}$ polarons are generally not observed in thermal equilibrium, all the available charges being stored in deeper defect levels such as $Fe^{2+}$ or, as it will be discussed in the following paragraph in $Nb_{Li}^{4+} - Nb_{Nb}^{4+}$ bipolarons. However, by optical or thermal excitation, their concentration can be increased. In particular, pump-pulse experiments demonstrate that a measurable bound polaron concentration of $Nb_{Li}^{4+}$ can be created using ns or fs pulses of visible light, which subsequently relaxes to the equilibrium value in some finite time [4], transforming back to $Fe^{2+}$.

For $Nb_{Li}^{4+}$ and $Fe^{2+}$ polarons the polaronic distortion (the distortion induced by the electron) is known: in the first case by a theoretical study from Nahm and Park [62] and S. Sanna [63] and in the second one by a direct measurement made by Sanson *et al.* [64]. In the first case of the antisite, according with [62], the self trapped electron originates a shift in the six oxygen ions by 0.04 Å (about 1% of the bond length) along the positive c axis and more precisely, the study reported in [63] calculates that the average interatomic distance $Nb_{Li} - O$ grows from 2.014 Å to 2.066 Å. Also in the case of iron the oxygen octahedron relaxes so that the average distance $Fe - O$ passes from $\sim 2.03$ Å to $\sim 2.12$ Å. A microscopic vision of the electron wave function localized in a $Nb_{Li}^{4+}$ and $Fe^{2+}$ site is shown in figure 2.1.4.

The absorption processes of such defects are expected to be quite similar to those of

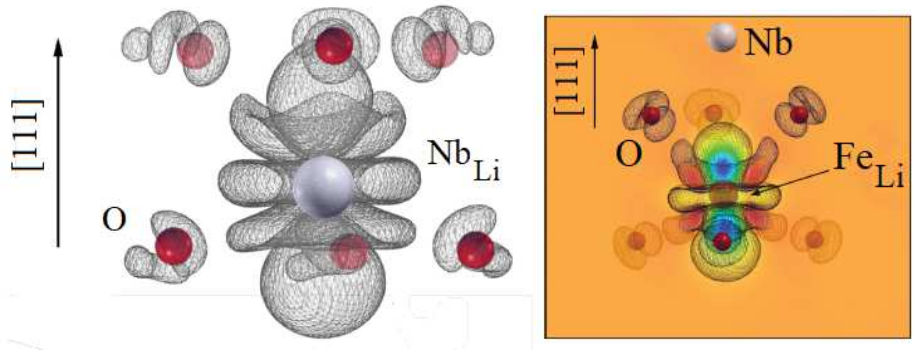


Figure 2.1.4.: (left) Electronic charge difference $Nb_{Li}^{4+} - Nb_{Li}^{5+}$ [63]. (right) Electronic charge difference $Fe_{Li}^{3+} - Fe_{Li}^{2+}$ [64]. The electron is strongly localized around the cation and the electron wave-function do not exceed the oxygen octahedra in both cases.

free small polarons. However, because of the defect potentials attracting the electron, in such cases the equilibrium level is expected to be lower if energetically compared to the one of free polarons. According to MCM model the electron energy 2.1.1 assumes now the form of:

$$E = KQ^2 - V^{'}Q - \varepsilon \tag{2.1.6}$$

where $\varepsilon$ represents the extra energy due to the defect attraction and $V$ is replaced by $V^{'}$ to consider that the different interaction between ions and free charge can give a different coupling constant with respect to the free polaron case. The energy is minimized for $Q_{min} = V^{'}/2K$ , analogously for the case of free polaron, which gives:

$$E_{min} = -E_P - \varepsilon \tag{2.1.7}$$

where $E_P = -V^{'2}/4K$. In this case the absorption band is peaked at $M = 2E_P + \varepsilon$. For antisite-bound polaron in lithium niobate, this value was found at $M_P = 1.69\,\text{eV}$, while for Fe-bound polaron $M_{Fe} = 2.62\,\text{eV}$ in the middle of the band gap [58] (see figure 2.1.5). From theory (see equation 2.1.7) and from the absorption band peak alone one cannot estimate a precise value for $E_P$ but rather a *range*, depending on the value of $\varepsilon$. For the antisite polaron the maximum value allowable compatible with observed data is $E_P = 0.845\,\text{eV}$, corresponding to a extra defect attraction $\varepsilon_P = 0$. This has as conclusion that the bound nature of the polaron, determined by the extra energy $\varepsilon$, decreases when the polaron deformation-stabilization energy $E_P$ increases, till reaching the extreme situation in which the polaron transform into a free one ($\varepsilon_P = 0$), even if the electron is localized on a defect. To gain more information, one can use the equation for the Half Width of the absorption peak (Eq. 2.1.5) together with an estimation of the phonon energy $\hbar\omega_0$. Assuming for all the bound polarons in Lithium Niobate the value obtained for the free polaron, $\hbar\omega_0 = 0.1\,\text{eV}$, we obtain the values for the polaron energies reported in table 2.1.1. However some care should be taken

| Type of polaron | $M$ (eV) | $W$ (eV) | $E_i(i = F,\ P,\ Fe)$ (eV) | $\varepsilon_i$ (eV) |
|---|---|---|---|---|
| *free (F)* | 1.09 | 0.37 | 0.54 | 0 |
| *antisite - bound (P)* | 1.69 | 0.40 | 0.58 | 0.53 |
| *Fe - bound (Fe)* | 2.62 | 0.44 | 0.70 | 1.22 |

Table 2.1.1.: Parameters related to the peak energies, $M$, and the widths, $W$, of different polaron absorption bands. $M$ and $W$ are fitted parameters [58]. $E_i$ are the polaron DSE and $\varepsilon_i$are the defect energy contribution derived from $M$ and $W$ assuming $\hbar\omega_0 = 0.1\,\mathrm{eV}$.

in assuming that both normal and defective sites possess the same phonon energy. For example it has been shown theoretically that the lattice surrounding the $Nb_{Li}$ antisite defect can display an anomalously large deformation upon capture of an electron [62]. This suggests that, due to the different structure of the defective site, the local lattice is softer and therefore the energy of the *local* vibrational mode is somehow different from the regular one. This point will be further addressed in Sec. 6.3. If the DSE energy is known, $\varepsilon_i$ can be calculated inverting the formula of the absorption band peak, $\varepsilon_i = M - 2E_i$, obtaining values reported in the la column of table 2.1.1.

### Hole polarons

Small hole polarons in LN consist in a hole self trapped at an oxygen ion in the vicinity of a cation vacancy, most probably $V_{Li}$ (figure 2.1.1 d). As in general $O^-$ hole polarons are most frequently produced optically by creation of an electron-hole pair from energetic photons or by multiple photon absorption processes [65], it is not astonishing that they were found in materials whose functions derived by interaction with intense light, such as $LiNbO_3$. Hole polarons are in this respect interesting because they can annihilate with an electron polaron, most probably in a non-radiative way. They therefore are a possible relaxation channel for a population of light-induced polarons whenever intraband photo-excitation processes are considered [66].

Hole polarons exhibits a broad absorption band in the visible range, centred at $E_{HP} \sim 2.5\,\mathrm{eV}$ (corresponding on a wavelength of about 500 nm) [67]. The optical absorption of $O^-$ is described by a photon-assisted hopping of the hole between equivalent adjacent O ions, which are located around the Li vacancy, thus restricting the hole polaron to one single $V_{Li}$. Since the spatial relation of the Li vacancies among themselves and to $Nb_{Li}$ antisite defects is not well known and the structure of the defect $O^- -$ ion next to $V_{Li}$ has not been clarified definitely, the contribution of hole polarons to the thermally and optically activated charge transport in $LiNbO_3$ is to date still unclear. Therefore also no definite values can be given for the hole polaron binding energy and thermal activation energy.

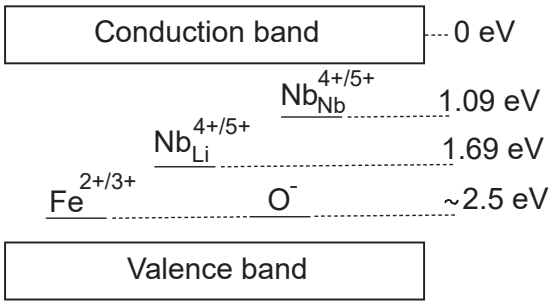


Figure 2.1.5.: Position of the centre of small polaron absorption band in the lithium niobate band gap. Value refers to the conduction band.

### Bipolarons

This polaron type is constituted by two electrons self-trapped at a cation site, or at two neighbouring cation sites, attracting each other by their joint lattice distortion. In addition cation site can be equal or different. The ground state of this polaron type in reduced congruent non doped $LiNbO_3$ was found to be of the type $Nb_{Li}^{4+} : Nb_{Nb}^{4+}$, where one electron is self-trapped in a antisite defect, while the other one in a regular niobium site [68] (figure 2.1.1 c). Since one of the binding cations ($Nb_{Li}$) is a defect ion with a different attracting charge, the ground state of such two-site bipolaron, populated by two antiparallel electrons, is characterized by a molecular orbital with a preponderance of electron probability density at the more attracting one. The electronic ground state of $Nb_{Li}^{4+}(4d^1)$, i.e. the antisite defect having trapped one electron, has axial symmetry with respect to the trigonal axis and, since the same can be expected for $Nb_{Nb}^{4+}$, the orientation of the 'Nb–Nb' molecule along the c axis will be most stable. In the presence of bipolarons a broad absorption band emerges, which is centred at $E_{BP} = 2.5\,\mathrm{eV}$ (corresponding to a wavelength of 500 nm) and covers the whole visible spectral range, giving to the samples a greyish colour [69]. Light illumination or elevated temperatures lead to a dissociation of bipolarons in favour of metastable $Nb_{Li}^{4+}$ and $Nb_{Nb}^{4+}$ polarons. Deducing the polaron energy is not straightforward as for single polarons, because in this case the model would have to be transformed in a two-site one, so standard consideration of the MCM model cannot be applied.

### Self-trapped excitons

The self-trapped exciton (STE) in LN is an electron-hole pair with strong coupling to $Nb^{5+}$ and $O^{2-}$ respectively within a single niobium-oxygen octahedron, which self localizes using a polaron-like mechanism. The absorption properties of STEs in LN are not known so far, but it may be speculated that they behave according to the general characteristics for STE in oxides materials, i.e. with an absorption feature in the blue/green spectral range [70]. Moreover, this defect is recognized as the origin of a luminescence in the blue - green spectral range, so that generally the presence of STEs in lithium niobate is probed by performing luminescence experiments with

a sufficiently intense and energetic pulsed laser, in order to promote band-to-band excitation. However this defect is extremely sensitive to the temperature and to the presence of defects, both aspects leading to a quenching of the photo-luminescence signal. Concerning the second aspect, it has been postulated that STE in LN appear in two modifications, depending whether the material is of stoichiometric composition or if some near-neighbouring $Nb_{Li}$ antisite defects are present [71].

STEs are generally studied at low-temperatures, using time- resolved luminescence measurements, in which a ns- laser pulse is used to excite a photoluminescence signal that decays with time. The luminescence decays can be described, according to Zatryb et al. [72], by the first time derivative of a stretched-exponential function:

$$I(t,T) = I_0(T)t^{\beta-1}exp\left[-\left(\frac{t}{\tau(T)}\right)^{\beta(T)}\right] \tag{2.1.8}$$

With increasing temperature the luminescence decay time is found to decrease from the milli- to the microsecond time range [73, 74]. A striking feature is the temperature-dependent change of the exponent $\beta(T)$ $(0 < \beta(T) < 1)$ that decreases by increasing the temperature, qualitatively representing the transition of a mono-exponential (at low temperatures) to a typical stretched exponential (at higher temperature) function. Furthermore, the decay time $\tau_{PL}(T)$ remains nearly constant for temperatures below 100 K with a value of $10^{-4}$ s whereas an Arrhenius-like behaviour is found for $T > 100K$ [75].

### Small polaron absorption cross sections

To resume, five type of small polarons can act in lithium niobate samples considered in this work, free, antisite-bound, Fe-bound, hole and bipolaron. In order to adequately investigate the properties of the material a precise knowledge of the number densities of the various polarons created in the samples is desirable. To achieve this, the information on the polarons cross section is necessary. For what it concerns iron, its value was already calculated by Kurtz *et al.* [76] combining optical absorption, Mössbauer and EPR measurements, while for others centres this study is reported by Merschjann *et al.* [77] employing pump-multiprobe experiments, such of the type described in chapter 6. The result of these studies is reported in figure 2.1.6 where it can be seen that all polarons are accompanied by strong, broad absorption bands. In particular bipolarons, hole and Fe-bound in the blue–green ($\lambda \sim 500$ nm), antisite-bound in the red ($\lambda \sim 760$ nm) and free in the near-infrared spectra ($\lambda \sim 1250$ nm). In table 2.1.2, values of the cross section at the wavelengths of interest for this work are reported. Some values were calculated in [77, 76] while others one are extracted from the assumed absorption band of figure 2.1.6 [58].

It is remarkable to notice that the values of $\sigma(500\,\text{nm})$ at the maxima of the specific absorption bands are apparently very similar for three types of different small po-

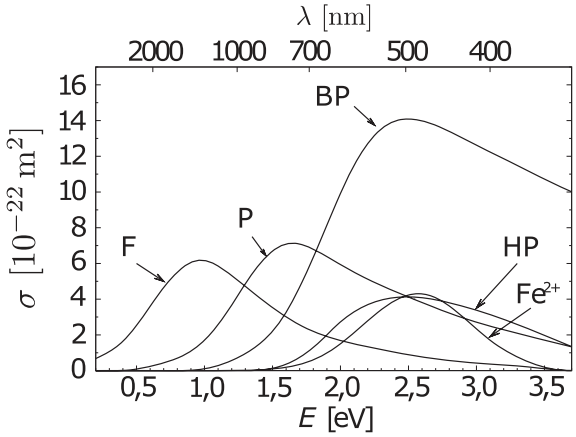


Figure 2.1.6.: Absorption cross section for small polarons of lithium niobate [77]. F refers to free, P to ansite-bound, HP to holes and BP to bipolarons.

| | F | P | $Fe^{2+}$ | BP | HP |
|---|---|---|---|---|---|
| | $10^{-22}\,\mathrm{m}^2$ | | | | |
| 1310 nm | $6 \pm 2$ | 1.5 | 0 | 0 | 0 |
| 785 nm | 3.1 | $7 \pm 2$ | 0.3 | 3.1 | 0.1 |
| 633 nm | 1.8 | 6.1 | 1.2 | 9.6 | 2.2 |
| 488 nm | 0.8 | 3.9 | $4.5 \pm 0.8$ | $14 \pm 2$ | $4 \pm 1$ |
| 445 nm | 0.6 | 3.5 | 4 | 13.8 | 4.1 |

Table 2.1.2.: Cross section of polarons species. Values having the error are calculated in [77, 76] while other are recovered from figure 2.1.6.

larons. Only bipolarons have a different behaviour because its absorption cross section is roughly twice as large as that for single small polarons.

## 2.2. Photogalvanic effect in polaron model

Schirmer *et al.* [43] give a comprehensive study on the photogalvanic effect in Fe:LN presented in section 1.5, but interpreting it with the polaron model. The main idea is that when an electron, initially trapped in some donor center, is photo-excited by a photon it experiences a transition to a de-localized state in the conduction band. In this initial stage the lattice cannot follow the charge dynamic, which propagates for some extent in a coherent way before losing its surplus energy and self-localizing into a small polaron. The formation of free polarons from optically created nonthermalized electrons has been proven experimentally by Qui *et al.* [78] and by Sasamoto *et al.* [61] by using a pump-probe setup to occur in a time scale below 0.1 ps.

In the model it is assumed that Fe exactly replaces a Li site of the defect-free crystal and that the structural positions of Li and Nb remain unchanged with respect to the

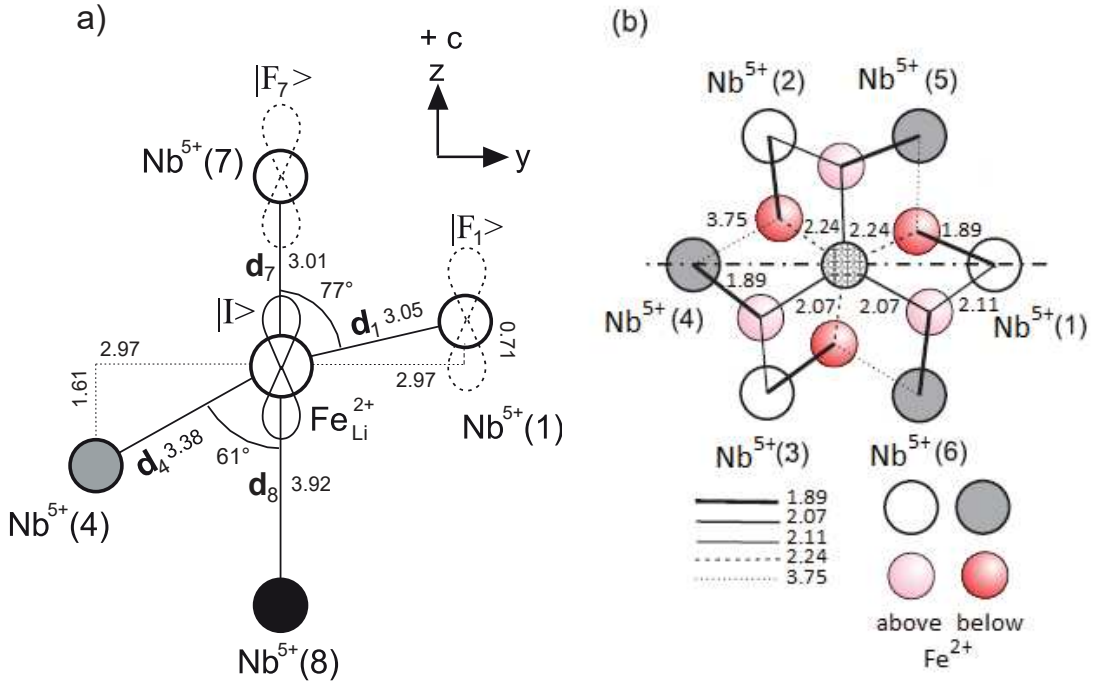


Figure 2.2.1.: Arrangement of $Fe^{2+}_{Li}$ and neighbouring $Nb^{5+}_{Nb}$ ions in $LiNbO_3$, assuming atomic positions unchanged with respect to the defect-free crystal. The lengths of the inter-ionic vectors are given in Å. (a) Cut along a yz glide mirror plane (b) Projection on a xy plane (perpendicular to c) [43].

defect-free crystal. The initial direction along which the charge is emitted as a Bloch wave is determined by the Fermi golden rule, the different matrix elements of the transition being given by the geometrical arrangement of the ions surrounding the donor center. As indicated in figure 2.2.1 on the right, there are three equivalent Nb ions in the plane perpendicular to $c$ [i.e., Nb(1), Nb(2), and Nb(3)], which are lying above Fe, and three further ones [Nb(4), Nb(5), and Nb(6)] below Fe. The $Fe - Nb$ bonds $d_1$, $d_2$, and $d_3$ all enclose an angle of 77° with c (figure 2.2.1 a). For the second set of Nb ions ($d_4$, $d_5$, and $d_6$), the angle is 61°. Since these latter bonds are considerably longer than the former ones, they contribute less to the total absorption. Among the bonds extending along the c axis, $d_7$ is shorter than $d_8$ and thus leads to a stronger absorption. Only the bonds $d_1$ to $d_6$ have projections perpendicular to c, and therefore transitions along these bonds are caused by ordinarily polarized light. Instead their projections on the c axis are rather small and, thus, the absorption by extraordinarily polarized light is dominated by transitions along $d_7$.

In a general, an extraordinarily polarized light produces a net current $\overrightarrow{j}$ along the $c$ direction according by the formula:

$$j_z \propto \sum_{i=1,2,3,7} j_{z,i} - \sum_{i=4,5,6,8} j_{z,i} \tag{2.2.1}$$

where the first and the second sums are related to the current along the positive and the

negative directions of the c axis, respectively. Each of the $j_i$ components is proportional to the electron displacement projected in the z direction $l_{i,z}$ weighted by the related transition probabilities $p_i$. In this vision the mean transport length along the c-axis, indicated as *photogalvanic length* in expression 1.5.5, is expressed by the formula:

$$L_{pg} = \frac{\sum_{i=1,2,3,7} p_i\,(\hbar\omega)\, l_{z,i} - \sum_{i=4,5,6,8} p_i\,(\hbar\omega)\, l_{z,i}}{\sum_{i=1,\ldots,8} p_i\,(\hbar\omega)} \tag{2.2.2}$$

The eight lengths $l_{z,i}$ can be much longer than $\mathrm{L_{PG}}$ (which is only the difference between the motion distance in the positive and negative directions) and are estimated to be in the range of few nm [43]. This indicates that the electron moves at most several $\mathrm{Nb_{Nb} - Nb_{Nb}}$ distances coherently along the c axis before the lattice relaxes around it to form a $\mathrm{Nb_{Nb}^{4+}}$ small polaron ground state. The indicated dependence of $\mathrm{L_{pg}}$ on $\hbar\omega$ expresses the fact that $l_{z,i}$ depends on photon energy. It is finally important to notice that the ionic movements triggered by the light-induced transfer of the electron adjusting to the new position represents also a current and in a complete description this would have to be considered because it contributes to the total photovoltaic effect. Despite of this, the removal of the electron from a Fe bound polaron shifts the ion of about 2% of the bond length along the negative c axis, thus such photo-induced ionic currents can be neglected in comparison with the much longer electronic transfer lengths.

After the end of this initial stage, the electron self-localizes into a polaron and can move only by thermally assisted hopping (see Section 2.3). The polaron has now two possible choices to continue its life: to move away or to jump back to the same initial site it came from, both processes being thermally activated but with a different energy barrier (see Fig. 2.3.1). This is believed to be the microscopic interpretation of the parameter $\phi$ introduced in Eq. (1.5.5), which denotes here the probability for the polaron to *not* go back to the starting site [79]. Being a thermally activated process, $\phi$ is expected to be temperature - dependent. Moreover it also depends on the distance between the final site and the initial empty donor centre, i.e. on $l_{z,i}$ and thus on the excitation wavelength. In addition, also the macroscopic electric field, developing across the end faces of the crystal under the flow of the PG current, if not short circuited, tends to drive the electron back to its home site $\mathrm{Fe_{Li}^{3+}}$. A part of the photo-excited electrons is therefore lost with a probability $1 - \phi$ in short time after being excited. It may be assumed that those polarons that are still present after a sufficiently long time are the surviving ones that succeeding hopping away and lost any memory on the starting position. One further aspect to consider is that the presence of a strong illumination $\left(I > 60\,\mathrm{MW/cm^2}\right)$ during the initial stage of the photo-emission process may significantly increase the photogeneration efficiency [79]. This phenomenon is due to the possibility that an additional photo excitation process take place before the newly localized particle performs its first hop. In this case the electron is pushed further away, reducing the probability to go back to initial donor site.

## 2.3. Thermally activated polaron hopping

The standard and simplest model traditionally considered to describe the thermal activated hopping between small polarons is the one proposed by Holstein in 1959 (MCM model)[59]. In order to accomplish the hopping between sites, thermally induced fluctuations of the surrounding lattice have to create a situation in which the electron energies at the initial and the final sites are equal. This facilitates the tunnelling of the electron between both sites in the related thermally excited state of the crystal [11]. In this model the transition between sites having different energies is mediated by phonons, which play an active-assisting role to conduction, in evident contrast with the band models. After the transfer, the lattice around the final site relaxes in such a way that the polaron forms again. The hopping energy barrier, activating the mobility of small polarons, is then the minimum energy needed to establish the lattice distortion leading to the coincidence of the involved electronic energies. A small-polaron hop may therefore be regarded as a three-step process. A jump begins when, (i) amidst atoms' thermal vibrations, extraordinarily large atomic displacements occur near a self-trapped carrier. (ii) Appropriate large-amplitude fluctuations enable the self-trapped carrier to transfer between sites. (iii) Finally these transitory large-amplitude atomic displacements relax, dissipating energy to the vibrations of surrounding atoms [12]. Exchange of vibration energy between atoms, governed by the vibrations' dispersion, is crucial to phonon-assisted hopping [12]. Moreover, in small polarons, electron are strongly self-trapped at one site and it is the presence of a non-vanishing electronic overlap term which allows electron transitions to a neighbouring site. According to these considerations the correct formula describing the charge carrier hopping has to introduce a strong dependence on the space separation between initial and final site.

The MCM model is a one dimension model of two vibrating molecules in the non-adiabatic regime, that occurs when ion vibrations are sufficiently fast compared to the electron hopping frequency. In order to present a more intuitive visualization of the absorption and transport processes of small polarons, it is advantageous to introduce a transformation from the site-centred coordinates $Q$ of figure 2.1.2(a) to those emphasizing the equivalence of initial and final site. The more symmetrized representation is found by the transformation $q = Q_1 - Q_2$ where $Q_1$ is the distorted coordinate, while $Q_2$ the undistorted one. In this vision, depicted in figure 2.1.3(b), the total energy can be rewritten as:

$$\tilde{E} = \frac{1}{2}Kq^2 \pm \frac{1}{2}Vq. \tag{2.3.1}$$

the energy minima now occur at $q_{min} = \mp V/2K$. Equation 2.1.2 become:

$$E_{min,q} = -\frac{V^2}{8K} = -\frac{E_i}{2}. \tag{2.3.2}$$

where $E_i$ is the DSE of the polaron ($i = F,\ P,\ Fe$). In this alternative presentation the polaron hopping can thus be viewed as a transition between two symmetrically

arranged parabolic potential sheets. Figure 2.1.3(b) also shows that the energy barrier for an electron to jump from one molecule to another is given by the intersection point of the two parabolic sheets, which is equal to:

$$U_i = \frac{E_i}{2} \tag{2.3.3}$$

This condition neglects the fact that the electron wavefunction, jumping back and forth the initial and the final site, may alter the energy barrier to be crossed of a quantity $J$. This is the electron "resonance energy" coming from the constructive interference of the wavefunction [80, 12]. In a one-dimensional tight binding model according to the usual polaron notation, this corresponds to one half of the bandwidth $2J$ of the rigid lattice, i.e. the energy barrier that one electron would need to cross to jump from a site to the other if the ions remained fixed and periodically placed. According to the above model, equation 2.3.3 is fulfilled when the electronic bandwidth $2J$ is small compared to the deformation - stabilization energy (DSE) of the small polaron involved in the hopping defined in section 2.1. This situation, indicated as "non adiabatic hopping" correspond to the case in which the lattice is able to re-adapt quickly to the electron motion. Although the motion of the polaron in its well is adiabatic, the chance of electron tunnelling from one molecule to the other during an excited state (corresponding to a point on the parabola branches of Fig. (2.1.3)) is low, so that the electron wavefunction loses its coherence and $E_P - J \approx E_P$.

The non-adiabatic hopping requires that the lattice possesses sufficient thermal energy to move quickly, so that the non-adiabatic approximation is considered valid only for temperatures above $\Theta_D/2$ where $\Theta_D \approx 503\,\mathrm{K}$ is the Debye temperature for lithium niobate [81]. However this estimate is quite rough. Experimental results obtained by Faust [60] show that the the Arrhenius behaviour of the conductivity in compensated LN is preserved till 150 K, indicating that the non-adiabatic approximation in LN is valid at least down to this temperature.

In the conditions detailed above, Holstein obtained an explicit expression for the polaron hopping frequency:

$$\nu_{ii} = \frac{J_{ii}^2}{2\hbar}\sqrt{\frac{\pi}{kTE_i}}exp\left(-\frac{E_i/2}{kT}\right) \tag{2.3.4}$$

where $J$ is the resonance energy and E the DSE energy. From the Einstein's diffusion equation, the mobility of a system of polarons is readily obtained [80]:

$$\mu_i = \frac{ed^2}{kT}\nu_{ii} \tag{2.3.5}$$

where $d$ is the hop distance. However the above expressions are applicable only if the initial and the final site are of the same type, and if the sites are located on a regular lattice. In this work we need to consider also the possibility of hopping

between non-equivalent sites (such as between a bound hopping to a free polaron, for example), placed on arbitrary distances (see 2.1). A proper generalization is provided by the semi-classical Marcus theory developed in 1956 [82], originally applied in biology and biochemistry to describe the rates of the electron transfer in reactions – the rate at which an electron can jump from one chemical species (called the electron donor) to another one (called the electron acceptor). The hopping rate generalized to two arbitrary polaron sites is therefore:

$$\nu_{ij} = \frac{J_{ij}^2}{2\hbar}\sqrt{\frac{\pi}{kT\Omega}} exp\left(-\frac{U_{ij}}{kT}\right) \tag{2.3.6}$$

where the subscript $i$ and $j$ indicate the type of the initial and the final site respectively ($i,\ j = F,\ P,\ Fe$), $k$ is the Boltzmann constant, $T$ is the absolute temperature, $\Omega$ the reorganization energy of Marcus theory, corresponding to the energy paid to rearrange the lattice and here equal to $(E_i + E_j)$ sum of the elastic energies of the two polarons, $U_{ij}$ is the energy barrier and $J_{ij}$ is the transfer integral.

The latter is defined as the half of the electronic bandwidth, i.e. the difference between the maximum and minimum energy allowed for the electron during the hop, and describes the dependence of the hopping frequency on the distance between sites. It is modelled with an exponential function type [80]:

$$J_{ij} = J_{ij}^0 exp\left(-\frac{\boldsymbol{r}_{ij}}{2a_{ij}}\right) \tag{2.3.7}$$

where $J_{ij}^0$ is in the order of the ionization energy of the atom, $r_{ij}$ is the distance separation between sites and $a_{ij}$ is an orbital parameter describing the localization radius of the electronic wave-function with respect to the cation site. Equation 2.3.7 states that the closer the sites, the higher the hopping frequency. As we are dealing with small polarons (localized essentially at one lattice site), the orbital parameter should not exceed the cation-oxygen length, which is about 2 Å. For the case of the free polaron hopping, encountered in stoichiometric or compensated LN, the conduction at high temperature is ensured only by free small polaron hopping on $Nb_{Nb}$ sites. An estimation for $J$ in this case has been provided in ref. [83, 84] giving $J_{FF} = 35\,\text{meV}$.

The energy barrier of the formula 2.3.6 depends again on the type of sites involved (through the indexes $i$ and $j$). An explicit expression can be derived in the non-adiabatic approximation by finding the intersection between the two parabolic energy surfaces similar to those shown in Figure 2.1.3. In a similar way the effect of an external applied field can be modelled. The hopping energy barrier assumes the form [85]:

$$U_{ij} = \frac{\left(E_i - \frac{\varepsilon_i - \varepsilon_j - e\overrightarrow{r_{ij}}\cdot\overrightarrow{E}}{2}\right)}{E_i + E_j} \tag{2.3.8}$$

where $\overrightarrow{E}$ is the applied electric field, $\overrightarrow{r_{ij}}$ the distance between two sites, $\varepsilon_{i(j)}$ is the

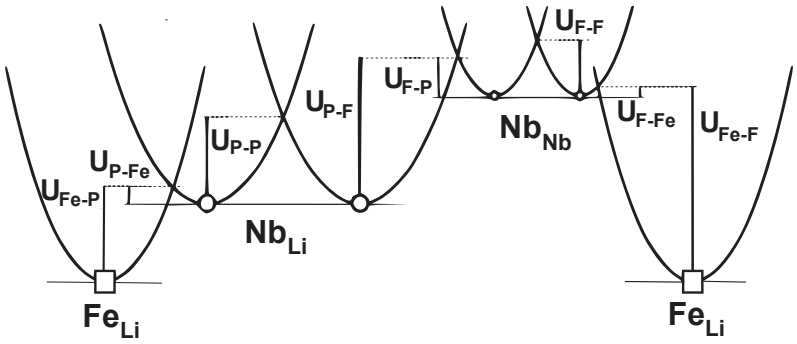


| | | final site | | |
|---|---|---|---|---|
| | energy in eV | *Free (F)* | *antisite (P)* | *Fe* |
| initial site | *Free (F)* | 0.273 | 0.069 | 0.003 |
| | *antisite (P)* | 0.634 | 0.290 | 0.043 |
| | *Fe* | 1.378 | 0.853 | 0.350 |

Figure 2.3.1.: Hopping energy barrier (equation 2.3.8) calculated for no applied electric field and using the values for the different polaron energies detailed in ref. [58] .

extra energy due to the defect attraction (see equation 2.1.6), and $E_{i(j)}$ is the DSE of the polaron, equal in modulus to the polaron elastic energy. In Fig. 2.3.1 are sketched all the possible hopping processes of small electron polarons in Fe-doped LN. From the values reported in Table 2.1.1, the relative thermal energy barriers are calculated with equation 2.3.8 in absence of electric field. Note that for $i = j$ and no applied field, equation 2.3.8 gives back the Holstein result, $U_{ii} = E_i/2$.

Equation 2.3.6 shows that when several parallel hopping processes are allowed, it is not straightforward to assess which one is going to dominate. At a certain temperatures, some processes may be very frequent for example because the centres involved are close to each other due to a high concentration. However, by rising the temperature, the frequency of other hopping processes may become more important depending on the respective activation energy. In particular, it may happen that at sufficiently high temperatures, the "thermal" term 2.3.8 compensates for a small "spatial" term 2.3.7, enabling a frequent hopping between distant sites.

## 2.4. Excitation and relaxation of polaron populations

The type of polarons contributing to the transport as well as their dynamic depends on the combination of various factor, as external light wavelength and intensity or sample's characteristics (i.e. presence of deep or shallow centre) and the temperature. Carrier formation and recombination is described by microscopic models based on pump and probe experiments, and here we discuss two of them in which the pulse pump laser

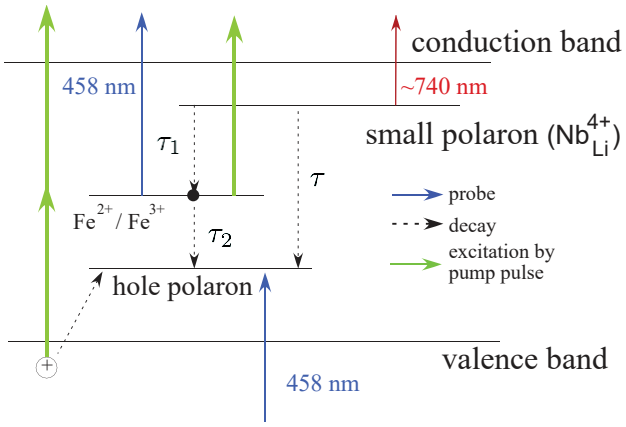


Figure 2.4.1.: Schematic description of the different excitation and decay paths of polarons in LN : Fe according to the Herth's model [66].

is centred at $\lambda = 532\,\text{nm}$, and the pulse duration in the ns regime: this is the same situation later used in the experimental part (see section 5.1).

The first complete study of the interplay between different polaron species at room temperature in Fe:LN sample ($[Fe] = 0.1\,\text{mol\%}$, $c_{Fe} = (5.5 \pm 0.2) \cdot 10^{23}\,\text{m}^3$) can be found in the article of Herth *et al.* [66]. The pump peak light intensity was $I = 410\,\text{MW/cm}^2$ and probes were $\lambda = 785, 458, 488, 514\,\text{nm}$. With such illumination conditions, it was shown that one and two photon absorption compete during the excitation. The one photon absorption involves iron centre, as previously described in section 2.2, while the two photon absorption, from valence to conduction band generate an hole in the valence band and an electron in the conduction band. The hole is subsequently trapped by a $O^{2-}$ near a lithium vacancy, forming an $O^-$ hole polaron, while the electron is quickly trapped in a $Nb_{Li}^{4+}$. In this condition the three polaronic centres involved in the transport are $Fe$, $P$, $H$, as sketched on figure 2.4.1.

The two-photon absorption is, in this way, a second independent generation path of P polarons, besides the common $Fe^{2+}$ excitation. After the pulse has finished, the $Nb_{Li}^{4+}$ polarons decay by hopping towards empty $Fe^{3+}$ centres, which is observed in a given time $\tau_1$. Hole polaron in this model are supposed to be less mobile than electron polarons. After a longer time, the $Fe^{2+}$ can release their electron to holes, till the original situation is restored. This process is characterized by a lifetime $\tau_2 > \tau_1$ .

Another interesting case, in which the polaron interplay is studied, is the one outlined by Merschjann *et al.* [86] in an undoped LN sample with different reduction degrees, at room temperature. Two extreme situations are considered here: the first one of a highly oxidized sample, the second one of an highly reduced one, both studied with a pump intensity of $I_p = 670\,\text{GW/m}^2$. The resulting model is sketched in figure 2.4.2.

In the case of the oxidized sample, a study in function of the intensity evidences that the one and two photon absorption compete during the excitation, as in the case studied by Herth *et al.* Electrons are excited from the valence band to the conduction band via a two-photon process, leaving a hole in the valence band. The carriers form F and P

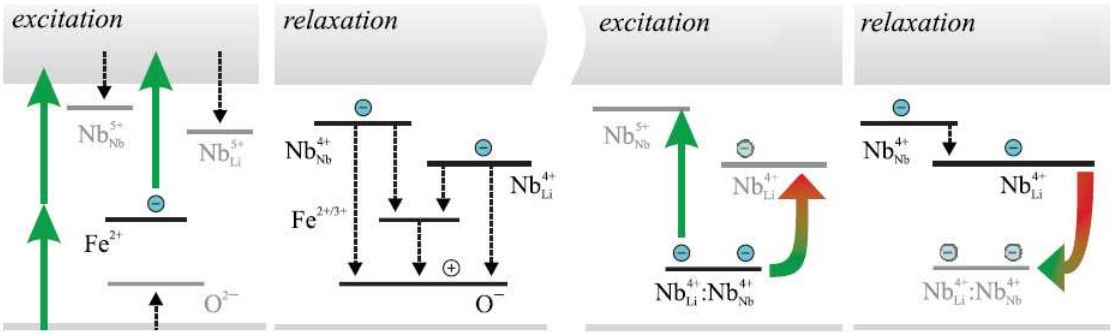


Figure 2.4.2.: Schematic description for the different mechanisms of excitation and recombination of small polarons in unreduced (left) and (right) reduced $LiNbO_3$ [86].

polarons, as well as bound hole polarons at oxygen ions adjacent to a lithium vacancy. When the excitation is finished the relaxation occurs mainly via recombination among $Nb_{Li}^{4+}$ and $O^{-}$. In this case to explain completely the results an additional centre was postulated, which was identified with residual extrinsic $Fe^{2+/3+}$ impurity, naturally present also in undoped materials, which contribute to the dynamic in the same way as already mention by Herth *et al* [66].

In the case of a highly reduced undoped sample no evidence for the two-photon absorption is found. These samples are characterized by a large concentration of bipolarons in the ground state. The results evidence that the external light pump can dissociate them, exciting one of the electrons to an adjacent Nb site, resulting in the formation of a free polaron, while the second electron remains as a bound polaron. Due to its absorption band ($E_{BP} = 2.5\,\mathrm{eV}$), the optical dissociation of bipolarons is a one photon process. The subsequent polaronic recombination proceeds via the direct recombination of $Nb_{Nb}^{4+}$ and $Nb_{Li}^{4+}$ polarons.

The case of this study showed that not only the light intensity, but also the reduction degree of the sample plays a key role in the balance between one and two photon absorption and consequently in the creation of hole polarons. In particular for the wavelength of $\lambda = 532\,\mathrm{nm}$, if a deep donor centre, is present in sufficient amount, the two-photon absorption process can be disregarded.

# Part II.

# Investigation techniques

# 3. Monte Carlo algorithm

General analytical solutions to the hopping transport problem discussed in the precedent chapter are difficult to obtain in the situation we are dealing with, on the contrary, the problem is well suited for numerical solutions. There are two principals numerical methods that can be used. The first one consists in performing Monte Carlo simulations of the hopping process. The second one consists in solving the balance equation relating the occupation probabilities of sites and the flow of charge carriers between them. In this work the first one is used to implement the small polaron theory based on Marcus-Holstein's model (section 2.3). The Monte Carlo method is the most direct numerical approach to simulate the hopping transport model and it is the best choice when it is necessary to simulate large systems, because it can be implemented with the least amount of computer memory per site. The simplest approach consists in simulating one single electron at a time. This situation corresponds to low electron density system where interaction between electrons can be ignored. The electron, randomly placed at an initial site, performs a random walk in a randomly generated structure. Furthermore for each hop the final position is randomly reached, but weighted by hopping frequency to each possible destination sites. The main idea is to consider that a polaron has been somehow generated in a random position of a Fe:LN lattice characterized by a given concentration of shallow defects ($Nb_{Li}$ antisites) and deep traps ($Fe^{3+}_{Li}$). We then study its random motion by performing a set of randomly decided hops among the different sites, as shown in figure 3.1.1. The code computes the rest time on each visited site and the next destination site by taking into account the Marcus-Holstein hopping frequency. It counts also the time, the number and the type of sites visited before polaron is captured by a perfect trap ($Fe^{3+}$ trap), as well as the final position reached. All the procedure is repeated with a sufficiently high number of polarons, until a satisfactory statistics is reached. The output of this code will be used to interpret the experimental results detailed in the next chapters.

## 3.1. System Model

This simulation program mimic the experimental conditions detailed in chapter 5. In the case of transient measures (Section 5.1) we consider that a light pulse with a duration of few ns is able to excite, from deep donor states, a certain number of polarons, which decay back to the deep traps levels with a certain dynamics. The main goal in this case is to simulate the relaxation of the polaron population. Since our experimental

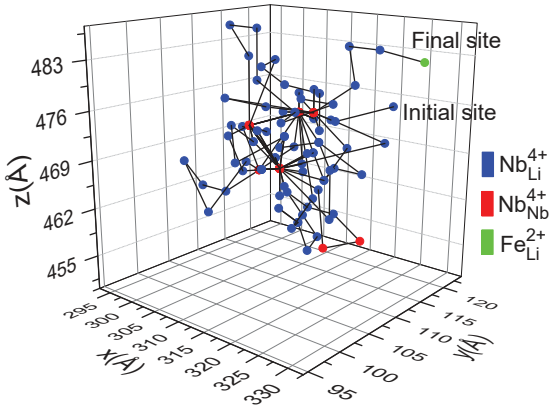


Figure 3.1.1.: Example of polaron path, calculated at $T = 300\,\mathrm{K}$ for a congruent composition, $[Fe^{3+}] = 0.52 \cdot 10^{25}\,\mathrm{m}^{-3}$, $a = 1.6\,\text{Å}$, $c = 1.5\,\text{Å}$, $E_P = 0.75\,\mathrm{eV}$, $E_F = 0.54\,\mathrm{eV}$, $E_{Fe} = 0.70\,\mathrm{eV}$, $J = 0.1\mathrm{eV}$, $SPT = 1$.

data considers only a time range starting several hundreds of ns after the pulse, we can assume that all the Site Correlation Effects (see Section 2.2) have finished and that the polaron at the beginning of our time window occupy a position completely uncorrelated with respect to the original donor site. Moreover, in agreement with *Sasamoto et al.*[61] we assume that in presence of antisite defects, which is the case for all the samples studied in this work, any free polaron is rapidly captured by an antisite. The initial position of the polaron is therefore randomly chosen in a $Nb_{Li}$ site. For the conditions used, we may consider that free polarons ($F$), antisite - bound polarons ($P$) and iron traps ($Fe$) are the only polaronic centres to deal with, so that the thermokinetic interplay between $Nb_{Li}$ or $Fe_{Li}$ with $Nb_{Nb}$ along the hopping transport is considered. Since the thermal hopping frequency from Fe towards any other site, calculated using Eq. 2.3.6 with a reasonable choice parameters, is very small, the simulation is stopped each time a Fe trap is reached. To be as close as possible to real situation in simulating measurements at high light intensities (transient measurements discussed in chapter 5.1) it must be considered that the initial pulse is probably sufficiently intense to empty a large part of $Fe^{2+}$ donors. Since our samples are characterized by a non-negligible ratio $\left[Fe^{2+}\right] / \left[Fe^{3+}\right]$ ratio in the dark, this means that the polarons produced with our experimental conditions are enough to increase considerably the traps initially present in the material just after the pulse. We modelled this effect in our simulation by decreasing in an appropriate way the trap concentration each time a polaron is launched. All those procedures are repeated until a sufficient statistics has been reached.

The program can be used also to simulate the transport measurements described in Section 7. In this case the illumination is continuous and produces bound polarons by releasing only electrons trapped on deep trap centres. Since here illumination is much less intense, we can suppose that the number of photo-excited polarons is small and we can well approximate concentration of the Fe traps with their value in the dark. In

this case what is simulated is the average distance covered by the polaron before being trapped by a Fe ion.

In principle it is possible to simulate the behaviour of the material in any temperature range. In practice we are limited to the validity conditions of the non adiabatic hopping approximation (see sec. 2.3), which for lithium niobate means $T > 250\,\mathrm{K}$. We expect that below this temperature the results may be inaccurate.

To resume the MC simulations can mimic the relaxation after pulse excitation in Fe:LN materials of various Fe and $Nb_{Li}$ concentrations provided that: (i) $Fe^{3+}$ is the only deep trap for photo-excited polarons (hole presence disregarded), (ii) the site correlation effect (SCE) is excluded and (iii) The non-adiabatic approximation holds.

The structure of the material generated in the algorithm is the one described in chapter 1 and in particular the unit cell described in the hexagonal base, having six lithium and niobium sites (Fig. 1.1.2) is employed. A supercell is built by replicating a given number of unit cells in order to create a lattice sufficiently wide to avoid systematic errors due to the repetition of given diffusion paths that would occur in a too small structure. Periodic boundary conditions are implemented to avoid surface effects. Point defects, i.e. niobium antisites and Fe ions corresponding to shallow and deep traps, substitute randomly a lithium site, with a probability depending on the respective concentration $C_P$ and $C_{Fe}$. In more detail the probability for a lithium site to be occupied by a shallow trap is $p_P = \frac{C_P}{C_{Li}}$ and similar for deep traps. While the niobium sub-lattice is fixed, the lithium sub lattice containing the random defect configuration can be kept equal or refreshed for each new polaron to evaluate the presence of possible memory effects or average over different defective configurations respectively.

## 3.2. Hop procedure

The electron performs a random walk in the system of sites described in the previous section. When the electron is located at site $i$, the probability that the next jump takes place toward a site $j$ is given by:

$$p_{ij} = \frac{\nu_{ij}}{\Gamma_i} \tag{3.2.1}$$

where $\nu_{ij}$ is the hopping frequency from site $i$ to $j$, (formula 2.3.6), $\Gamma_i = \sum_j \nu_{ij}$ is the total rate of hopping away from site $i$ . The selection of the final site $j$ is established through the Gillespie algorithm: a method well established for simulating chemical reactions but which can be applied also in this context [87]. The jump to be performed is decided by a random number $x$, generated in the range $[0, 1]$ from a uniform distribution and finding the $j$ such that:

$$\sum_{k=1}^{j-1} p_{ik} \leq x < \sum_{k=1}^{j} p_{ik} \tag{3.2.2}$$

It ensures that when the electron jumps from site $i$ each site $j$ is selected with the probability $p_{ij}$, as shown in figure 3.2.1. In practice only the right-hand inequality

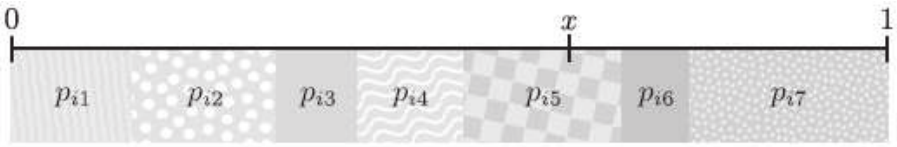


Figure 3.2.1.: A destination site is selected by picking a random number $x$, and finding the interval in which it falls. The destination site corresponding to that interval is selected, in this case site 5 [87].

needs to be tested. One starts from $k = 1$ and adds one term at time to the sum, stopping as soon as the sum exceeds $x$. The time that the electron spends on the site $i$ before hopping is calculated as

$$\tau = \frac{T}{\Gamma_i} \tag{3.2.3}$$

where $T$ for each hop is randomly generated according to an exponential distribution with unit expectation value and unit variance.

A technical difficulty that can arise in Monte Carlo simulation is the problem of so-called *soft-pairs,* sketched in figure 3.2.2. If two equal sites are spatially close and their hopping energy barrier is small compared to $kT$, the jump frequency between these two sites will be high in both directions. The electron that arrives at one of these sites may jump backwards and forwards a large number of times before escaping from this pair of sites. Normally this type of hops are very fast, therefore for each step the total time of the simulation advances only by a small amount. It is possible that the electron escape from this pair of sites but it will be necessary to follow it for a large number of hops, making the simulation inefficient. Moreover the problem is most severe when sites are randomly placed and the localization length is small, as in the case studied in this thesis. The electron in principle can even remain trapped in this condition for an infinite time, stopping the simulation. This particular situation is not an artefact of the simulation but it is a real physical effect occurring during the hopping. For this reason these cases are not eliminated, but handled following the procedure described in [87]. The surrounding idea is to consider the soft pair formed by the two sites $a$ and $b$ as a new unique centre and to modify the hopping rates in the vicinity of the soft-pair eliminating the transition from $a$ to $b$, but preserving the rate of escaping from the pair. In doing this the local properties of the system are changed to make the simulation more efficient, but the global transport properties are preserved. If $x$ is a possible destination site for $a$ or $b$ the hopping frequencies $\nu_{ax}$ and $\nu_{bx}$ are replaced by the hopping frequency out of the soft pair:

$$\nu_{sf-x} = \frac{\Gamma_b \nu_{ax} + \nu_{bx}\nu_{ab}}{\Gamma_b + \nu_{ab}} \tag{3.2.4}$$

A way to verify if the soft-pair algorithm works properly is comparing results obtained without this approximations. Globally the results must be the same but with the advantage of a smaller execution time. When the final destination is decided several

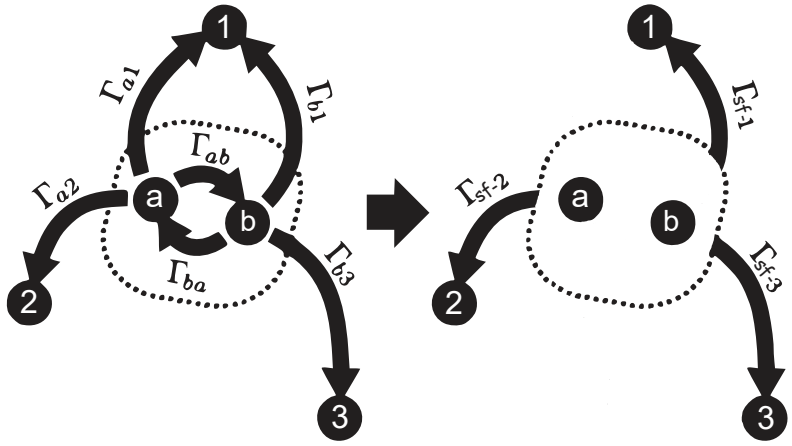


Figure 3.2.2.: The sites a and b form a soft pair. The transition from a to b is removed, and the other rates from this new site are modified preserving global transport properties.

scenario can occur, according to the choice of the initial parameters described in the next section:

- if the final site is a $Fe^{3+}$ and a Light-Induced Absorption simulation is in progress, this site disappear from the counting of possible final sites and the simulation restarts with a new polaron without refreshing the defect configuration (trap-refilling effect). In this way we model the fact that, due to the random nature of the defective lattice, not all traps are equivalent and those with higher probability to be visited are the first to disappear;
- in all other cases (transport measurements) the hop procedure restarts till when either a fixed number of hops is reached (to prevent soft pair loop) or when a time decided by the user is reached;

When the simulation ends, for every polaron, several informations necessaries for the sequent analysis are stored: the final $(x, y, z)$ electron position in the lattice calculated with respect to the initial generation site, the time spent to arrive in this position and the number and type of hops performed during its path. With all this information it is possible to construct also the population variation of free, $Nb_{Li}^{4+}$ and Fe polarons separately in a simple way. Every time that, during the hopping, the polaron A transforms into a B , the total concentration of A decreases and at he same time the one of polaron B increases. Those transformation events are plotted as a function of the time like in Fig. 3.4.1. These normalized graphs can be interpreted as the survival probability of each single polaron species.

## 3.3. Simulation parameters

The simulation accepts from the user different kind of parameters, concerning every aspect of the experiment.

SAMPLE PARAMETERS

- *shallow traps concentration*: it corresponds to the antisite concentration, therefore it allows to mimic the sample compositions, from congruent to stoichiometric one;
- *deep traps concentration*: this is the initial $Fe^{3+}$ concentration at the beginning of the experiment.
- *photo-excited carriers concentration*: this parameter is used to describe trap refilling effect. According to the photo-excitation model assumed here (see chapter 6), almost all the $Fe^{2+}$ present in the dark are emptied by the pump pulse laser, so that the concentration of $Fe^{3+}$ traps present in the sample subsequent to the pulse can be taken to be equal to the total Fe concentration $\left[Fe^{3+}\right] \simeq [Fe]$. Likewise, this number gradually decreases to the dark concentration value during the recombination process between photo-excited carriers and $Fe^{3+}$. The photo-excited carriers concentration assumes the meaning of the initial number of polarons created by the pump which will refill a part of the $Fe^{3+}$ traps. Setting this parameter to zero corresponds to neglect this effect and it is therefore used to simulate continuous-wave experiments and/or an the behaviour of an oxide sample, for which only a negligible amount of $Fe^{2+}$ are excited by the laser with compared to the amount of trap.

These parameters are experimentally known from sample characterization discussed in chapter 4, and reported in table 4.3.1, 4.3.2, 4.3.3.

HOPPING FREQUENCY PARAMETERS

- *DSE and defect energies* of free, bound and iron polarons (see Section 2.1)
- *orbital characteristic length*s: they correspond to the orbital parameters of formula 2.3.7. As here we consider three centres ($F$, $P$, $Fe$) there are in principle $3 \times 3 = 9$ possible hop combinations corresponding to 9 different possible values of $a_{ij}$. However, we can reduce the number of unknown parameters based on the following considerations: (i) the distance - dependent part of the hopping frequency must be symmetric, so that $a_{ij} = a_{ji}$. (ii) Since the Nb-O octahedra structure is very similar between $Nb_{Li}$ antisite defect and the $Nb_{Nb}$ regular site, we consider that the transfer integrals between those sites should not be very different. For the same reason, we can assume that all the transition to and from Fe site are described by the same transfer integral. (iii) Additionally we can neglect the hopping process from Fe towards other polarons because Fe is considered a "perfect" trap. Therefore the parameters $a_{Fe,F}$ or $a_{Fe,P}$ play no role. This leads to the following simplifications:

$$a_{FF} = a_{FP} = a_{PF} = a_{PP} = a$$

$$a_{F\mathrm{Fe}} = a_{P\mathrm{Fe}} = c$$

- *transfer integral pre-factor*: it corresponds to the pre-factor $J_{ij}^0$ of formula 2.3.7. As for the orbital parameter, in principle 9 different values are possible, however it is possible to reduce the number of unknown parameters using the same considerations adopted for the orbital length: (i) due to the symmetry of the hopping process, the pre-factor must be symmetric, so that $J_{ij}^0 = J_{ji}^0$. (ii) Since the Nb-O octahedra structure is very similar between $\mathrm{Nb_{Li}}$ antisite defect and the $\mathrm{Nb_{Nb}}$ regular site, we consider that the transfer integrals between those sites should not be very different. For the same reason, we can assume that all the transition to and from Fe site are described by the same transfer integral. (iii) Additionally we can neglect the hopping process from Fe towards other polarons because Fe is considered a "perfect" trap, therefore the parameters $J_{Fe,F}$ or $J_{Fe,P}$ play no role. This leads to the following simplifications:

$$J_{FF} = J_{FP} = J_{PF} = J_{PP} = J_1$$

$$J_{F\mathrm{Fe}} = J_{P\mathrm{Fe}} = J_2$$

  Finally, as the simulation results are weakly dependent on the pre-factor $J_i$, for sake of simplicity we can set $J_1 \approx J_2 = J \sim 0.1\mathrm{eV}$. This value is estimated from Ref. [83] which measured the transfer integral at high temperature in Fe:LN, where the conduction is due essentially to free polarons. The data are probably not very accurate, yet, as stressed before, this parameter is not strongly affecting our results.

EXPERIMENT PARAMETERS

- *temperature:* setted equal to the experimental value.
- *electric field* : it corresponds to the saturation value of internal space charge field and for this reason it is applied only along the $\widehat{c}$ axis of the crystal.
- *experimental time:* stops the simulation if the polaron has not encountered a deep trap before this time limit. It is used to simulate transport properties as a function of time in trap-free samples. In all the other cases, this time must be chosen to be larger than the duration of the experiment.

SIMULATION PARAMETERS

- *polaron creation site:* in this work the creation of the polaron is randomly chosen in a antisite defect but the possibility to create it in a regular $Nb$ site is allowed, for example to study the dynamic in a stoichiometric composition.
- *polaron numbers:* The number of iterations for the code, corresponding to the total simulated paths. This value has to be chosen depending on the quality of the statistics needed to describe a particular experiment.

- *max hop per polaron numbers:* this the maximum number of hops that each electron can perform. To simulate completely the transport this condition has not to be fulfilled before the condition on the experimental time is satisfied. It has an active role in the case in which the user disable the soft-pair mechanism, in fact if a soft-pair occurs it is nearly impossible to fulfilled the condition on the experimental time in a reasonable computing time and it is necessary to impose another way to stop the electron hopping. After some tests a compromise value was fixed at 10000 hops.

- *soft-pair pair threshold (SPT):* this parameter comprised between 0 and 1 allows the user to set the tolerance for the soft-pair algorithm. The condition to start the soft-pair routine when a hop between two sites $a$ and $b$ is computed is given by $p_{ab} > SPT$ AND $p_{ba} > SPT$, where $p_{ab(ba)}$ is the probability that, among all the possibilities, the destination site for a hop starting from $a$ ($b$) will be $b$ ($a$). For $SPT = 1$ no soft pair will be considered and the simulation is "exact" but very slow; for $SPT = 0$, all the possible hops are treated as soft pair. A compromise must be reached to describe accurately the system in the shortest possible time.

- *lattice dimension*: typical lattice dimensions are are ($n_a$, $n_b$, $n_c$) = (80, 80, 80) unit cells, corresponding to ($L_a$, $L_b$, $L_c$) = (412, 412, 1108.8) Å.

## 3.4. Soft-pair approximation and trap refilling effect

The typical simulation output for the polaron population decay is presented in figure 3.4.1(left), where in addition the results including the soft pair approximation is discussed. Three curves represent the population variation of three considered polarons, free ($F$), antisite-bound ($P$) and Fe-bound (Fe) in a congruent sample having $[Fe^{3+}] = 0.52 \cdot 10^{25}\,m^{-3}$ at room temperature. All polarons are created initially on a $Nb_{Li}$ site and this result evidences that during the time their number decrease till the relaxed situation, because electron are trapped by $Fe^{3+}$, increasing the amount of $Fe^{2+}$. Bound polarons can also convert in free ones and *vice versa*: the efficiency of those processes determines the overall concentration of the different polaron species at a given time. For the choice of input parameters shown in figure 3.4.1(left), practically no free polarons are present. The same simulation was repeated with a soft-pair threshold of 0.8. The approximation is very good, and in this case the computation time on a standard laptop decreased from 122 to 100 minutes. This time benefit can be much larger in case that the sample characteristics allow for the presence of a larger concentration of soft pairs and can play a crucial role when, to reduce the statistical noise, is necessary to simulate a large number of polarons.

In figure 3.4.1(right) the influence of the trap-refilling effect is demonstrated. Here only the normalized population decay of shallow-bound polarons is presented for simplicity. The situation chosen for this test is the one of an highly reduced sample

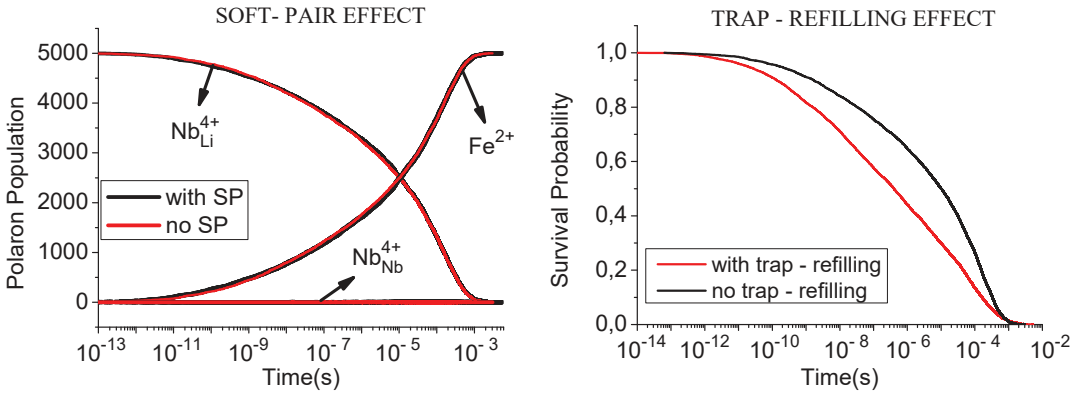


Figure 3.4.1.: (left) Typical output of polarons population variation with addition soft-pair effect influence (soft-pair threshold of 0.8, no trap-refilling). (right) Influence of trap-refilling effect considering $SPT = 1$. Both effects are simulated at room temperature and using $a = 1.6\,\text{Å}$, $c = 1.5\,\text{Å}$, $E_P = 0.75\,\text{eV}$, $E_F = 0.54\,\text{eV}$, $E_{Fe} = 0.70\,\text{eV}$, $J = 0.1\text{eV}$.

($[Fe^{2+}]/[Fe^{3+}] = 260\%$) doped with 0.1 mol%, for which $\left[Fe^{2+}\right] = 1.37 \cdot 10^{25}\text{m}^{-3}$ and $[Fe^{3+}] = 0.52 \cdot 10^{25}\text{m}^{-3}$. In the case "with trap-refilling" we consider that the pump pulse is sufficiently intense to empty all the available donor centres $Fe^{2+}$ present in the sample so that the concentration of deep traps just after the pulse is equal to the total amount of iron present in the sample. In the particular case simulated here, just after the pulse, $[\text{Fe}^{3+}] = [\text{Fe}_{\text{tot}}] = 1.89 \cdot 10^{25}\,\text{m}^{-3}$ with an initial total light induced polaron concentration of $1.37 \cdot 10^{25}\,\text{m}^{-3}$. Every time that an electron recombines with a $Fe^{3+}$, this deep trap disappears (trap refilling effect) so that the trap concentration gradually reduces from the initial concentration to the dark value $[Fe^{3+}] = 0.52 \cdot 10^{25}m^{-3}$. This situation is compared to the simulation in which this effect is neglected and the initial deep trap concentration remains unchanged and equal to the dark value of $[Fe^{3+}] = 0.52 \cdot 10^{25}m^{-3}$. In the first case the system at the beginning has a larger trap concentration compared to the second one and for this reason the decay is faster. Clearly this effect can be neglected in case that the concentration of photo-excited carriers is small compared to the trap concentration, i.e. when the sample is very oxidized and/or when the light intensity is small.

## 3.5. Influence of the electric field

The other informations stored during the simulation, i.e. the final $(x, y, z)$ electron position in the lattice calculated with respect to the initial generation site and the number and type of hops performed during its path, serves to study the diffusion and to simulate experimental photoconductivity data. An example is shown in figure 3.5.1 (left) in which the distribution of the final positions projected on the $z$ axis is shown for two different diffusion times. In this example a system containing only antisite-bound polaron with congruent stoichiometry is considered at room temperature. The distri-

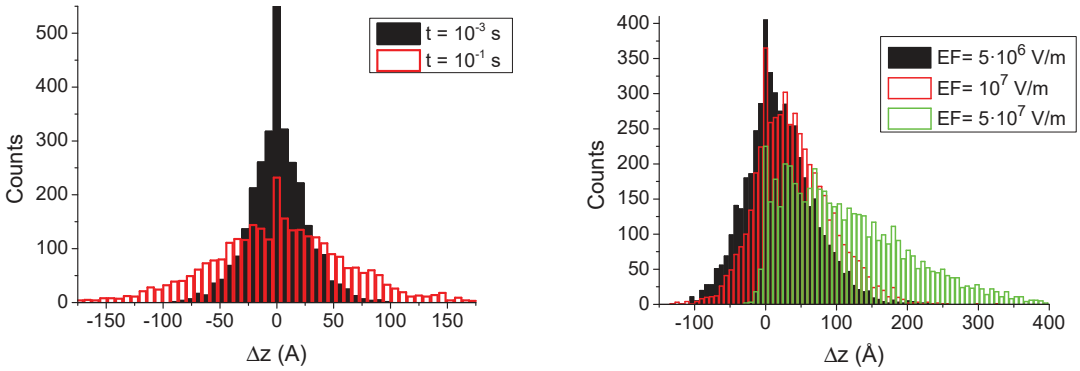


Figure 3.5.1.: (left) Distribution of final bound polarons after a fixed time without applied electric field. (right) Effect of the saturation value of internal space charge field along $\hat{c}$ direction. Other parameters used in these simulations are $a = 1.6\,\text{Å}$, $c = 1.5\,\text{Å}$, $E_P = 0.75\,\text{eV}$, $E_F = 0.54\,\text{eV}$, $E_{Fe} = 0.70\,\text{eV}$, $J = 0.1\text{eV}$, $SPT = 1$.

bution is symmetric, as it can be expected, and its mean value is zero. In addition the distribution broadens with the time due to polaron diffusion. An analysis of simulation results shows that the pronounced central peak arises from three contributions: (i) a certain amount of polaron do not perform any hop in the selected time window, (ii) another part is stopped from the birth in a soft pair situation (the final position can be either the initial position either the first neighbour), (iii) the rest performs closed-loop paths coming back to the initial position. We will return to a more detailed treatment of those aspects in Chap. 8.

The right side of the figure shows what happens when the internal space charge electric field reaches the saturation value. In addition to the distribution broadening, the mean value of the distribution is no longer zero, but assumes a value which depends on the intensity of the electric field. Having a look in the jump frequency rate formula, Eq. 2.3.3, an electric field of magnitude $\left|\overrightarrow{E}\right|$ adds a contribution to the hopping activation energy which lowers the activation energy for jumps concordant with it and raises the hopping activation energy for jumps in the opposite direction. In this situation, longer-range hops whose rates are suppressed by their relatively large field-free activation energies are enabled by the application of a sufficiently strong electric field, giving rise to an asymmetry in the distribution.

To remain in the validity of the model, it is necessary to remain in the hopping regime. This is possible only if the electric field is not strong enough, so that the stochastic behaviour dominates on the electric field-forced one. This condition is satisfied if the energy added by the electric field is small compared to the thermic one, i.e. $ed\left|\overrightarrow{E}\right| \ll k_B T$, where $e$ is the elementary charge, and $d$ is the mean distance between hopping sites. This condition evidences that the limit value of the field depends on the type of hop and temperature. In the case of hops between free polarons $d = 3.765\,\text{Å}$,

so that at room temperature $E_{max} \sim 7 \cdot 10^7\,\mathrm{V/m}$. For bound polarons it is possible to calculate roughly the mean distance as $d = (2\pi N_B)^{-1/3}$, where $N_B$ is the bound polarons concentration. In the case of a congruent sample $N_B = 1.89 \cdot 10^{26}\mathrm{m}^{-3}$so that the mean distance results equal to $d \sim 9\,\text{Å}$. In this condition, at room temperature, $\mathrm{E_{max}} \sim 2 \cdot 10^7\,\mathrm{V/m}$.

## 3.6. Influence of orbital lengths and polaron energies

In the following we give some qualitative examples on the effect of the different simulation parameters on the output of our code. We focus here on the analysis of the decay curves and, for sake of simplicity, we concentrate here on the role of three parameters, which are the ones forming the object of section 6.3, namely $a$, $c$, and $E_P$. According to the hypothesis on the characteristic orbital length parameter (Sec. 3.3), $a$ governs electron hops among $\mathrm{Nb_{Nb}}$ sites, among $\mathrm{Nb_{Li}}$ sites and mixed $\mathrm{Nb_{Nb} - Nb_{Li}}$ hops. Changing this parameter physically means changing the overlap between the electron wave functions centred on these sites. The impact of this parameter on the results of the simulation is demonstrated in the first row of figure 3.6.1 where the survival probability of the $\mathrm{Nb_{Li}^{4+}}$ polaron population is shown, only at low ($T = 200\,\mathrm{K}$) and high temperature ($T = 400\,\mathrm{K}$) for simplicity. Graphs show simulation data only from $10^{-7}\,\mathrm{s}$ because these parameters affect only the long tail of bound polaron decay. At 200 K the influence of $a$ is limited, all the curves decaying within a similar time range. However, increasing the temperature the effect of $a$ becomes more marked. The graph shows that increasing this orbital length the bound polaron mean life time decreases but the global shape of the decay curve remains unchanged. This can be easily understood having a look on the hopping frequency formula 2.3.6 and considering that the population lifetime must be proportional to the inverse of the hopping frequency: $\tau \sim \nu^{-1}$. The larger the hopping frequency, (and this is the case increasing $a$), the faster the electron moves along its path to be finally captured by an iron.

The orbital length parameter $c$ governs electron hopping between $\mathrm{Nb_{Nb}}$ or $\mathrm{Nb_{Li}}$ polarons toward $\mathrm{Fe^{3+}}$. Increasing this parameter affects the efficiency of the trapping events. Also in this case, an increase of $c$ produces a shortening of the polaron lifetime, as expected. However, here the influence appears to be more evident at low temperature. An inspection of the different hop types performed by the polarons in the two temperature regimes, explains the reason for the observed dependencies. For the particular choice of parameters used for these simulations, it appears that at low temperature, almost all the polarons starting on a $\mathrm{Nb_{Li}}$ antisite are captured by a Fe trap in one single hop (Fig. 3.6.2, left). Very rare conversion to free polarons is allowed, and practically no $F \to F$ hops are observed as it is demonstrated by the average numbers displayed in Table 3.6.1. In this situation the decay curve represents essentially the distribution of the hopping times necessary to perform the single trapping event. The paths that are performed in a larger number of hops correspond practically always to

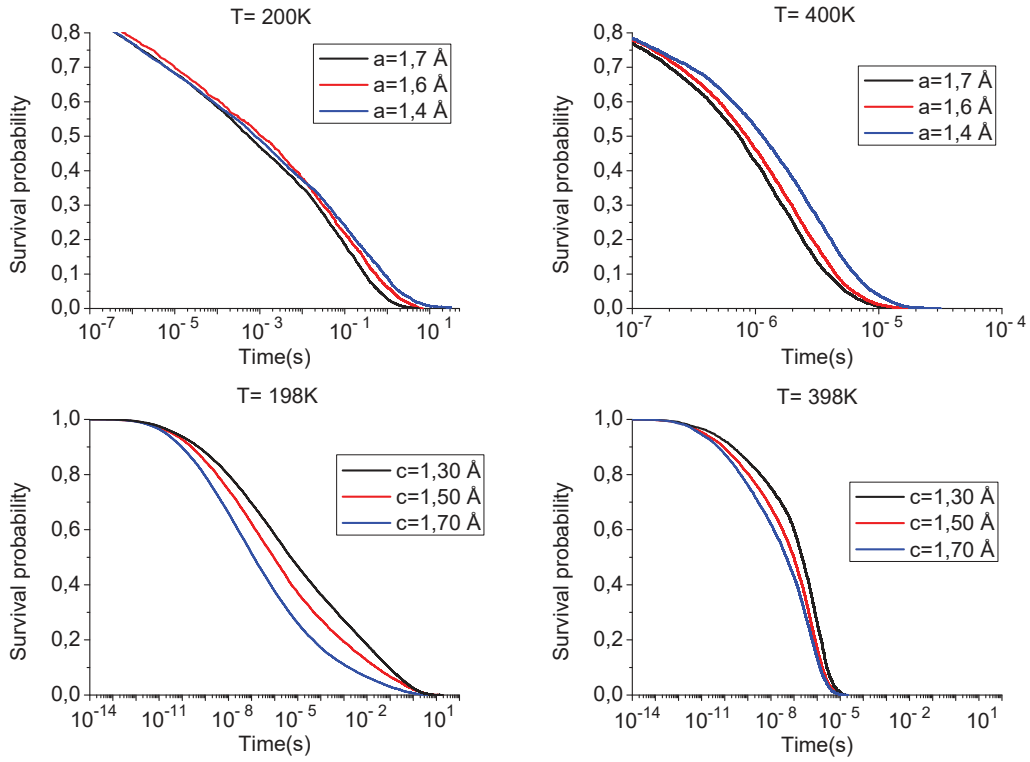


Figure 3.6.1.: (first row) Influence of $a$ orbital length at $T = 200\,\mathrm{K}$ and $T = 400\,\mathrm{K}$ . The simulated system is a congruent one, having $\left[\mathrm{Fe}^{3+}\right] = 0.38 \cdot 10^{25}\mathrm{m}^{-3}$ and considering trap-refilling (initial total light induced polaron concentration of $0.01 \cdot 10^{25}\,\mathrm{m}^{-3}$). Other parameters are $c = 1.5\,\mathrm{\AA}$, $E_P = 0.75\,\mathrm{eV}$, $E_F = 0.54\,\mathrm{eV}$, $E_{Fe} = 0.70\,\mathrm{eV}$, $J = 0.1\mathrm{eV}$, $SPT = 1$. (second row) Influence of $c$ orbital length in the same temperature ranges for a congruent sample having $\left[\mathrm{Fe}^{3+}\right] = 1.89 \cdot 10^{25}\mathrm{m}^{-3}$ and considering trap-refilling (initial total light induced polaron concentration of $1.37 \cdot 10^{25}\,\mathrm{m}^{-3}$). Other simulation parameters are $a = 1.6\,\mathrm{\AA}$, $E_P = 0.75\,\mathrm{eV}$, $E_F = 0.54\,\mathrm{eV}$, $E_{Fe} = 0.70\,\mathrm{eV}$, $J = 0.1\mathrm{eV}$, $SPT = 1$. [Note: we chose two different samples for these studies because a great amount of $\mathrm{Fe}^{3+}$masks the effect of $a$, and vice versa a less amount of traps do not permit to appreciate the influence of $c$ ].

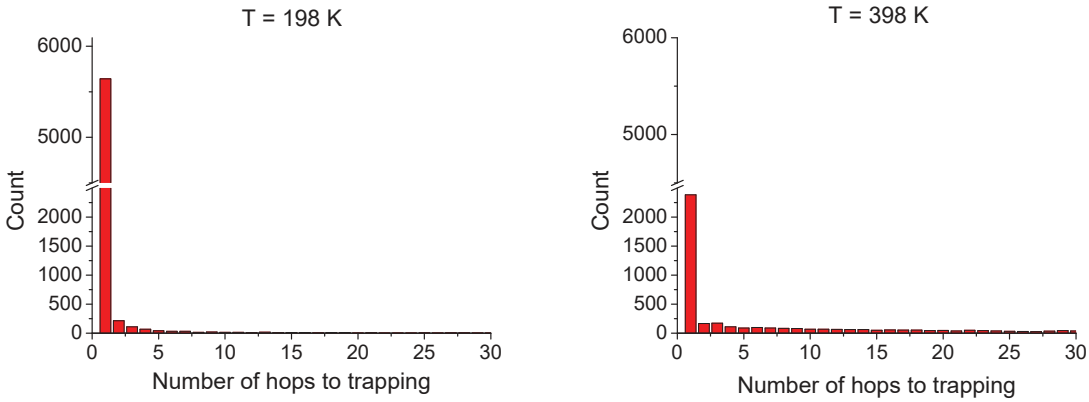


Figure 3.6.2.: Distributions of the number of hops to trapping for the simulations shown in Figure 3.6.1 for the congruent sample having $\left[Fe^{3+}\right] = 1.89 \cdot 10^{25} m^{-3}$at $T = 198\,\mathrm{K}$ and $T = 398\,\mathrm{K}$, initial total light induced polaron concentration of $1.37 \cdot 10^{25}\,\mathrm{m}^{-3}$, $a = 1.6\,\text{Å}$, $c = 1.5\text{Å}$ ,$E_P = 0.75\,\mathrm{eV}$, $E_F = 0.54\,\mathrm{eV}$, $E_{Fe} = 0.70\,\mathrm{eV}$, $J = 0.1\mathrm{eV}$, $SPT = 1$.

| | $\left\langle \frac{n_{PP}}{N_{tot}} \right\rangle$ | $\left\langle \frac{n_{PF}}{N_{tot}} \right\rangle$ | $\left\langle \frac{n_{FP}}{N_{tot}} \right\rangle$ | $\left\langle \frac{n_{FF}}{N_{tot}} \right\rangle$ | $\left\langle \frac{n_{PFe}}{N_{tot}} \right\rangle$ | $\left\langle \frac{n_{FFe}}{N_{tot}} \right\rangle$ | $\langle N_{tot} \rangle$ |
|---|---|---|---|---|---|---|---|
| $T = 198\,\mathrm{K}$ | 0.12 | $2.6 \cdot 10^{-4}$ | $2.6 \cdot 10^{-4}$ | $2.5 \cdot 10^{-4}$ | 0.87 | 0 | 27 |
| $T = 398\,\mathrm{K}$ | 0.13 | 0.11 | 0.10 | 0.25 | 0.40 | $5.8 \cdot 10^{-3}$ | 57 |

Table 3.6.1.: Average hop types normalized over the total for the simulation shown in Figure 3.6.1 for the congruent sample having $\left[Fe^{3+}\right] = 1.89 \cdot 10^{25} m^{-3}$, initial total light induced polaron concentration of $1.37 \cdot 10^{25}\,\mathrm{m}^{-3}$, $a = 1.6\,\text{Å}$, $c = 1.5\,\text{Å}$, $E_P = 0.75\,\mathrm{eV}$, $E_F = 0.54\,\mathrm{eV}$, $E_{Fe} = 0.70\,\mathrm{eV}$, $J = 0.1\mathrm{eV}$, $SPT = 1$.

soft-pair situations composed by two antisites $\mathrm{Nb_{Li}} \leftrightarrow \mathrm{Nb_{Li}}$ sufficiently close to each other. By increasing the temperature, the situation gradually changes (3.6.2, right): the polaron is able to perform a larger number of hops before being captured by a Fe trap and it can even perform some hops as a free polaron (See Table 3.6.1). It should be noted here that the average number $\langle n_{PF} \rangle$ of "conversion" hops ($\mathrm{Nb_{Li}} \rightarrow \mathrm{Nb_{Nb}}$) is very close to the one of the reciprocal process $\langle n_{FP} \rangle$ ($\mathrm{Nb_{Nb}} \rightarrow \mathrm{Nb_{Li}}$) indicating that often the polaron jumps back and forth between an antisite and a regular Nb site without a real transport. The influence of $a$ is therefore weak at low temperatures and stronger at high ones because this parameter is effective only if several hops are performed. In other words, $a$ rules the "transport" regime. Conversely, the influence of $c$ is more evident at low $T$ because in this temperature range all the processes amount to trapping ones. Of course, these observation strongly depend on the particular choice of the sample parameters: in a material with very low trap concentration, the transport regime continues also at low $T$. Those points will be addressed in greater detail in section 6.4.1.

The third dependence here studied is the effect of the $\mathrm{Nb_{Li}^{4+}}$ deformation stabilization energy (DSE) , $E_P$, the energy gained only from the deformation of the lattice (without

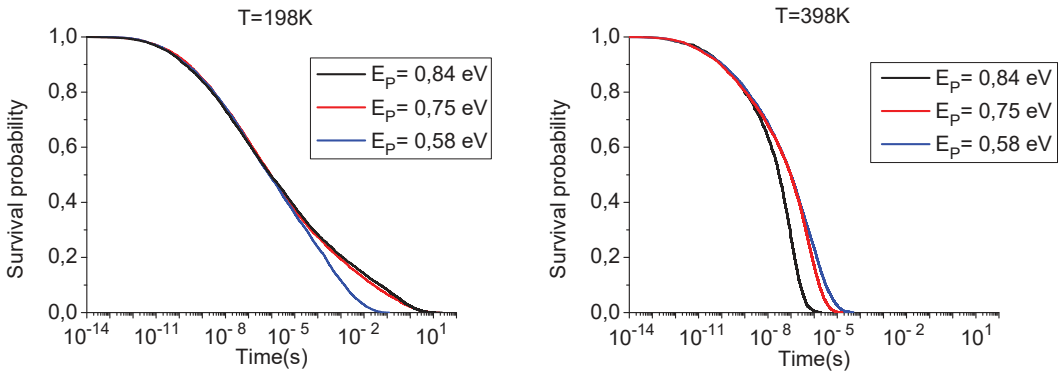


Figure 3.6.3.: Influence of polaron binding energy $E_P$ at low and high temperature. In this test the composition is congruent, $\left[Fe^{3+}\right] = 1.89 \cdot 10^{25} m^{-3}$, the trap-refilling is considered (initial total light induced polaron concentration of $1.37 \cdot 10^{25}\,m^{-3}$), $a = 1.6\,\text{Å}$, $c = 1.5\,\text{Å}$, $E_F = 0.54\,eV$, $E_{Fe} = 0.70\,eV$, $J = 0.1eV$, $SPT = 1$.

the defect attraction contribution) which is equal and opposed to the energy required to deform the lattice to its new equilibrium position upon capture of an electron on the $Nb_{Li}$ site. According to the Marcus - Holstein polaron hopping model, the elastic energy of the polaronic sites affects the temperature dependence of the hopping frequency through the information on energy barrier of the process (Eqs. (2.3.6, 2.3.8)). The value for $E_P = 0.58\,eV$, already discussed in Sec. 2.1 will be studied and tested in this work, so we show here qualitatively the impact of this parameter on the output of our simulations. The maximum value compatible with the observed optical resonance at $M = 1.69\,eV$ allowed from theory (see equation 2.1.7) is $E_P = 0.845\,eV$, corresponding to a extra defect attraction $\varepsilon_P = 0$.

In figure 3.6.3 the result of the influence of this parameter as a function of temperature is reported. The behaviour is, as a function of the temperature, not trivial. At low temperatures, this parameter affects only the long time tails of the decay. Moreover the smallest energy value is the one that produces the shortest decay time. On the contrary, at high temperature the opposite behaviour is observed and the simulation corresponding with the highest value of $E_P$ are the ones that decay faster. Around room temperature there is the crossing point for which three energies lead more or less to the same result, with survival probabilities nearly superimposed each others.

# 4. Samples

This chapter is devoted to the presentation of experimental procedures used to grow, prepare and characterize the lithium niobate single crystals doped in volume with iron used in this work. The crystal growth was performed by Czochralski technique; the prepared samples were characterized from the structural and compositional point of view with different techniques (HR-XRD, Raman and optical absorption) before using them for the main experimental tests.

## 4.1. Czochralski technique

The Czochralski technique is a well established technique generally employed in the realization of single crystals of semiconductor, metal and oxides material. This one was used the first time in 1964 to grow with success lithium niobate single crystal [16] and up to know it is the best technique to prepare this material.

This method is based on the controlled solidification of the liquid phase around a seed of the material that has to be grown. The process is divided into several steps, sketched in figure 4.1.1. The seed is the nucleation element for the crystallization and in the case of this work it is obtained by commercial wafer of pure $LiNbO_3$ and mounted on a suitable holder so that the $\widehat{c}$ crystallography axis is kept vertical. The seed it is immersed vertically in the melt material, which is contained in a platinum crucible initially maintained at a temperature higher than the melting point. When the seed is in contact with the melt, the solid-liquid interphase and the relative meniscus is formed. In this initial phase the temperature plays a fundamental role: it has not to be too low to in order to avoid an uncontrolled polycrystalline aggregation around the seed, on the other hand it cannot be too high neither to avoid the melting of the seed. The optimized thermal condition is achieved adjusting its value in way in which the solidification and fusion rate equals each other, creating an equilibrium situation. At this point, the growth is initiated by pulling up slowly the seed with a speed of about $2\,^{\mathrm{mm}}/_{\mathrm{h}}$. This breaks the balance between the mass fluxes and forces the solid phase to grow at expense of the liquid one. If the thermal conditions inside the growth chamber are optimized, a large crystal can be grown free of macroscopic defects such as cracks or bubbles. In addition, to grow the crystal in optimum condition, the solid-liquid interphase has to be homogeneous and planar and this condition is achieved by spinning the seed around its axis with constant speed, typically between 30 and 5 rpm. This motion permits indeed to contrast internal convective motion due to the thermal

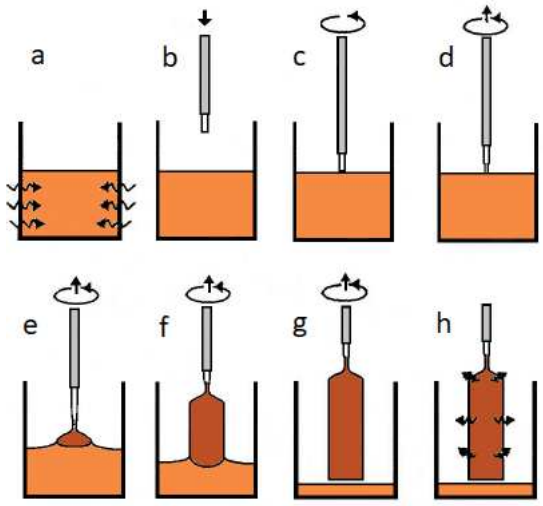


Figure 4.1.1.: Schema of Czochralski procedure. (a) The material is fused, (b) the seed is moved down toward the melt, (c) the seed touches the melt and the liquid-phase interface is formed, (d) the seed is pulled up ad the neck formation starts, (e) shoulder formation, (f) body formation (g) separation from the melt and (h) crystal cooling till room temperature.

gradient of the melt. The initial phase of the grow consists in the creation of the neck of the boule, having more or less the seed dimension. The next phase is the creation of the shoulder (figure 4.1.1 c) during which the diameter of the crystal increases. The final step is the body growth, performed with a constant diameter and which constitutes the part with the best crystallographic quality. The control of the crystal diameter during the different steps of the growth is performed by an automatic control system which tunes the temperature of the growth chamber. The feedback is performed by measuring the weight of the crucible containing the melt: the rate of mass variation is proportional to the area of the section of the crystal boule, and therefore on the square of the radius. The typical result of the growth process is shown in figure 4.1.2. The diameter is about 2 cm, while its length is of about 5 cm.

### 4.1.1. Melt composition

Three series of samples were producted for this work. The first two are composed of congruent samples (Nb/Li ratio equal to 0.94, see Sec. 1.2.1) but with different iron concentrations (Series sample A and B). Those series of samples are conceived to study the effect of different trap concentrations. The starting power for these samples is a mixture of commercial congruent $LiNbO_3$ (Sigma Aldrich 99.999) and $Fe_2O_3$ powders. The Fe contents in the melt was chosen equal to 0.1 mol%, 0.05 mol% and 0.02 mol%.

The third sample series (referred as C) is the one having a fixed deep trap concentration but a different amount of shallow traps (i.e. niobium antisites). In particular three samples, doped with Fe 0.11 mol%, with different stoichiometry were grown at the Institute for Physical Research in Ashtarak (Armenia). High-purity compounds of

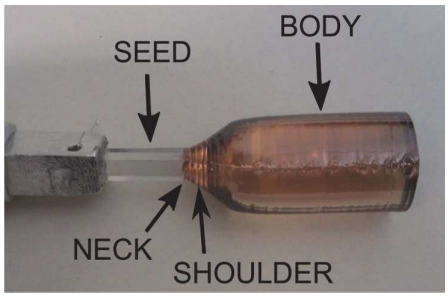


Figure 4.1.2.: Typical LN crystal produced by Czochralski technique.

$Nb_2O_5$ from Johnson-Mattey, and $Li_2CO_3$ from Merck, in powder form, were used as the starting materials for sintering of the lithium niobate charges of different composition, via solid state reaction. The appropriate amount of iron was added to the initial charges of LN in the form of $Fe_2O_3$ oxide (Merck) and thoroughly mixed. This kind of growth is known to produce samples with a composition which is not constant along the growth direction. Therefore the precise composition of the final samples cannot be assumed to be equal to the one of the melt and need to be characterized as explained in Sec. 4.3.2.

## 4.2. Sample preparation

### Poling

After being grown, each lithium niobate boule is not uniformly polarized domain but generally contain residual residual ferroelectric domains of inverted polarization which may interfere with the subsequent optical characterization. To overcome this problem, a poling treatment has been performed on all the as-grown crystal boules. This process consist in heating the boules at high temperature, generally 50 °C above the Curie point ($T_C = 1150\,°C \sim 1210\,°C$, going from the congruent to the stoichiometric composition). An electrical current of some tenths of mA is then applied to the crystal boule in a direction parallel to the z axis by platinum-wire connections. During the application the current, while the material is above the Curie temperature, it can be observed that the voltage difference between the positive and negative electrodes decrease exponentially till a constant value is reached. This happens because the LN structure is rearranging orienting all the domains along one direction. When the constant value is reached the poling process, which normally takes a time around one hour, is terminated. With the current applied, the crystal is finally slowly cooled through the Curie point to $T_C - 50\,°C$. The current is then switched off and the crystal is slowly cooled down to room temperature.

The poling was performed in two slightly different configurations for the three sample series, obtaining in any case the same result. For the congruent sample series (A and B) the poling was performed after the growing, heating again the three boules in a

tubular horizontal oven (Gero Hochtemperaturöfen GmbH) and applying a dc current of $10\,{}^{\mathrm{A}}/_{\mathrm{m}^2}$. The two electrodes through which apply the current have to be parallel to each other and both perpendicular to the $\hat{c}$ axis. They are obtained by cutting the shoulder and the bottom of the boule with a diamond blade and covering the two surfaces with platinum paste. The off- congruent series (C) was poled directly during the growth process applying to the crystal-melt system a dc electrical current of about $10\,{}^{\mathrm{A}}/_{\mathrm{m}^2}$.

## Orientation and cut

The subsequent phase is the orientation and cut of the boule along the chosen crystallographic axis. The boules are glued to a special goniometric sample holder and roughly oriented according to the boule morphology and to the seed axis. The sample holder is then attached to a South Bay 540 cutting machine, equipped with a diamond-coated Cu-alloy blade. A small slab of the boule is then cut and analyzed using a Philips MRD diffractometer in the Bragg Brentano geometry, in order to obtain the miscut angle between the chosen crystallographic direction and the cut surface. The results of this analysis are then used to finely tune the crysal orientation on the cutting machine and a set of samples is then produced.

For this work x-cut samples are used, i.e. with the main surface perpendicular to the crystallographic [1 1 0] direction. Typical sizes of about $5 \times 10\,\mathrm{mm}$ and thicknesses varying between 1 and 3 mm are used. The final preparation stage is surface lapping and polishing to optical grade. The lapping is the removal of material to produce a smooth unpolished surface and a midrange abrasive solution composed by alumina particles having dimension of $3\,\mu\mathrm{m}$ is normally used. The polishing is exploited to produce a scratch-free specular surface using an SF1 alumina colloidal suspension particle dimension of $0.1\,\mu\mathrm{m}$. This treatment was performed by the lapping machine Logitech PM5. The final result is a sample having a flat surface with roughness in the nanometer range.

## Thermal treatments

While the total iron concentration ($\mathrm{N_{Fe}} = \mathrm{N_{Fe^{2+}}} + \mathrm{N_{Fe^{3+}}}$) is chosen in the crystal growth procedure, it is possible to change reversibly the ratio $\mathrm{N_{Fe^{2+}}}/\mathrm{N_{Fe^{3+}}}$ (reduction degree) by oxidation or reduction processes. The $[\mathrm{Fe}^{2+}]$ concentration in the as-grown samples is typically of the order of $10^{24}\,{}^{\mathrm{at}}/_{\mathrm{m}^3}$ or less. This quantity can be altered, and in particular increased, by performing reduction treatments in an $\mathrm{Ar} + \mathrm{H_2}(2\%)$ atmosphere at a flux of $90\,{}^{\mathrm{Nl}}/_{\mathrm{h}}$ at a temperature of 500 °C. The reduction degree is determined by changing the duration of the treatments and eventually, by performing some subsequent air annealing for few hours to produce a homogeneous colouration of the samples. On the contrary, to decrease the $[\mathrm{Fe}^{2+}]$ oxidation treatments are performed in $\mathrm{O_2}$ atmosphere at a flux of $90\,Nl/h$ at a temperature of 500 °C for several hours.

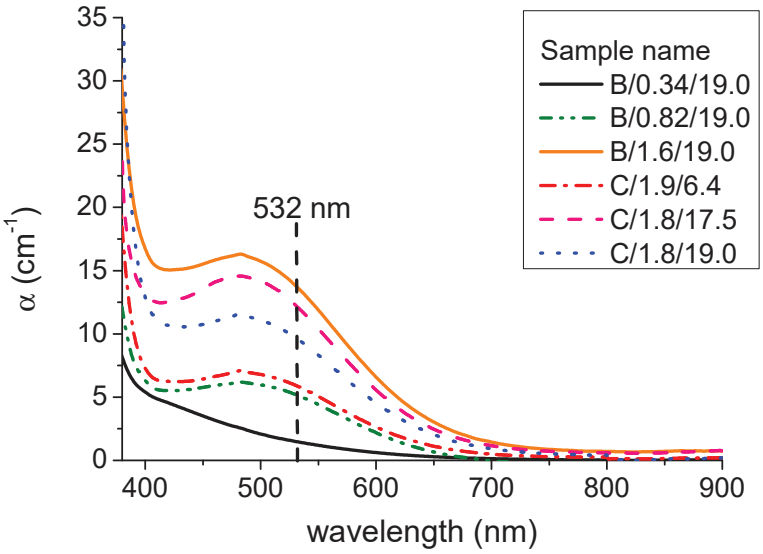


Figure 4.3.1.: Absorption coefficient for sample series B and C. Its value at 532 nm is used to calculate the amount of $Fe^{2+}$.

Every thermal treatments are performed heating the sample with a rate not superior to 300°/h, to avoid the damage of the crystal by thermal stresses, using a tubular horizontal oven (Gero Hochtemperaturöfen GmbH).

## 4.3. Sample Characterization

After the preparation procedure, the compositional and structural properties of each sample are investigated by optical absorption and Raman spectrometry. The measurements were performed respectively at the Physics and Astronomy Department of the University of Padova and at the Laboratoire Matériaux Optiques, Photonique et Systèmes of Université Lorranie et Supéléc (Metz, France).

*The samples analysed in this work are labelled according to the following convention: [Series name]/[$Fe^{3+}$ concentration ($10^{19}\,cm^{-3}$)]/[$Nb_{Li}$ concentration ($10^{19}\,cm^{-3}$)]. Thus for example the sample B/0.34/19.0 is the sample of the series B containing* $0.34{\cdot}10^{19}\,cm^{-3}$ $Fe^{3+}$ *and* $19.0 \cdot 10^{19}\,cm^{-3}$ *antisites.*

### 4.3.1. Iron concentration

In photorefractive applications using Fe : $LiNbO_3$, concentrations of $Fe^{2+}$ and $Fe^{3+}$ ions are two of the most important factors in determining the performance of the material. Indeed $Fe^{2+}$ and $Fe^{3+}$ ions serve here respectively as source and traps of electrons.

In this work the ordinary optical absorption at 532 nm is used to determine the $Fe^{2+}$ absolute concentration, as proposed by Berben *et al.* [31]. The transmittance $T_S$ of each sample is measured by a Perkin-Elmer V- 670 spectrometer in the range

| Sample name | $[Li]\,\%$ nominal | $[Nb_{Li}]$ $10^{19}cm^{-3}$ | $[Fe_{tot}]$ $10^{19}cm^{-3}$ | $[Fe^{2+}]$ $10^{18}cm^{-3}$ | $[Fe^{3+}]$ $10^{19}cm^{-3}$ | $R\,\%$ |
|---|---|---|---|---|---|---|
| A/0.36/19.0 | 48.45 | 19.0 | 0.37 | $0.14 \pm 0.01$ | $0.36 \pm 0.01$ | $3.9 \pm 0.2$ |
| A/0.87/19.0 | 48.45 | 19.0 | 0.95 | $0.79 \pm 0.05$ | $0.87 \pm 0.05$ | $9.1 \pm 0.5$ |
| A/0.5/19.0 | 48.45 | 19.0 | 1.89 | $14 \pm 1$ | $0.5 \pm 0.1$ | $262 \pm 20$ |
| A/1.84/19.0 | 48.45 | 19.0 | 1.89 | $0.54 \pm 0.03$ | $1.84 \pm 0.03$ | $2.9 \pm 0.5$ |

Table 4.3.1.: Sample series A. Summary of parameters for the group of samples having the same composition but different total iron concentration used in transient measurement. The reduction degree is defined as $R = [\mathrm{Fe}^{2+}]/[\mathrm{Fe}^{3+}]$.

between 300 and 900 nm, by using ordinarily polarized light, with an accuracy on the single measure for every wavelength of 0.3%. To isolate the contribution to the optical absorption deriving only from iron, $T_S$ is normalized to the transmittance $T_C$ relative to a calibration standard obtained from a pure undoped lithium niobate crystal, obtained in the same experimental conditions. Then, from the normalized spectra, the absorbance $A = -ln(Ts/Tc)$ is calculated. This quantity permits to compute the absorption coefficient due only to the presence of the iron $\alpha_{Fe} = A/d$, where $d$ is the sample thickness. Typical results for $\alpha$ are shown in figure 4.3.1. This quantity in turn is linked to the $Fe^{2+}$ concentration by the formula:

$$[\mathrm{Fe}^{2+}] = \frac{\alpha_{532\,nm}}{\sigma_{532\,nm}} \tag{4.3.1}$$

where $\sigma$ is the cross section $\sigma_{532\,nm} = (3.95 \pm 0.08) \cdot 10^{-18}\,\mathrm{cm}^2$. Results of this characterization are summarized in table 4.3.1, 4.3.2 and 4.3.3.

To determine the reduction degree $[\mathrm{Fe}^{2+}]/[\mathrm{Fe}^{3+}]$ of each sample, not only the concentration of filled traps, but also that of empty ones has to be known. The $[\mathrm{Fe}^{3+}]$ direct measurement was attempted by measuring the total [Fe] concentration using the method reported by Ciampolillo *et al.* [32] which is based on measuring the absolute absorption coefficient at 342 nm. However at this wavelength the transmittance of our samples is so small that, even after reducing their thickness, the absorption coefficient could not be measured. We decided to assume that the nominal [Fe] concentration is equal to the nominal one and to estimate $[\mathrm{Fe}^{3+}]$ by difference.

### 4.3.2. Niobium antisite characterization

Crystals grown from Li-deficient, stoichiometric or Li-surplus melts have compositions differing from the one of the melt, with the composition changing strongly along the growth direction. In addition the crystal composition does not uniquely depends on the melt composition, as geometrical and other growth parameters strongly influence the growth process. A linear relationship between the Li deficiency and the broadening of Raman peaks was established for compositions ranging from congruence to

| Sample name | $[Li]\,\%$ nominal | $[Nb_{Li}]$ $10^{19}cm^{-3}$ | $[Fe_{tot}]$ $10^{19}cm^{-3}$ | $\left[Fe^{2+}\right]$ $10^{18}cm^{-3}$ | $\left[Fe^{3+}\right]$ $10^{19}cm^{-3}$ | $R\,\%$ |
|---|---|---|---|---|---|---|
| B/0.34/19.0 | 48.45 | 19.0 | 0.37 | $0.37 \pm 0.02$ | $0.34 \pm 0.02$ | $11 \pm 2$ |
| B/0.82/19.0 | 48.45 | 19.0 | 0.95 | $1.17 \pm 0.09$ | $0.82 \pm 0.09$ | $14 \pm 2$ |
| B/1.6/19.0 | 48.45 | 19.0 | 1.89 | $3.3 \pm 0.1$ | $1.6 \pm 0.1$ | $21 \pm 3$ |

Table 4.3.2.: Sample series B. Summary of parameters for the group of samples having the same composition but different total iron concentration used for continuous-wave measurements. The reduction degree is defined as $R = [\mathrm{Fe}^{2+}]/[\mathrm{Fe}^{3+}]$.

stoichiometry for the first time by Okamoto *et al.* [88]. Subsequently in [89] this relationship was extended also to the sub-congruent range. This technique can be used to characterized in a convenient way the composition of our samples.

All the samples were measured in the X(zz)X backscattering configuration using the LabRAM Aramis equipment, in order to obtain the $A_1(TO_1)$ modes, corresponding to Nb/O vibrations in x-cut samples [90]. The modes were fitted by Lorentzian functions in order to measure their FWHM $\Gamma$ and from the equation [89]:

$$X_C = 69.39 - 0.123 \times \Gamma_{A_1(TO_1)} \tag{4.3.2}$$

the molar concentration $X_C$ can be obtained. In the following we will assume that Fe doping is not going to change significantly our results, because its molar concentration is one order of magnitude smaller than that of $\mathrm{Nb_{Li}}$ antisites. However, in this work a different instrument with respect to the one mentioned in [89] was used, so the formula 4.3.2 has to be checked. The spectral line profile used in this analysis is Lorentzian which width is due to the "true" Raman line shape convoluted with a "instrumental" function, which depends on the instrument used, on the wavelength etc. As the convolution of two Lorentzian functions is again a Lorentzian whose width is equal to the sum of the widths of the two functions, it can be considered that a change in the setup may affect only the intercept of equation 4.3.2, while the slope may be considered as accurate. To estimate the correct intercept, a reference sample is needed. The congruent composition is by definition the one in which the crystal composition is equal to the melt composition and can be expected to be the one with the highest compositional uniformity. In the following therefore sample C/1.8/19.0, grown from the congruent melt is considered as reference.

The molar value $X_C$ is now converted in an information on the $\mathrm{Nb_{Li}}$ concentration. Let $X_C = \frac{[Li]}{[Li]+[Nb]}$ be the Li/Nb ratio expressed in decimal notation. According to the widely accepted defect model for non – stoichiometric lithium niobate, i.e. one antisite is compensated by four Li vacancies discussed in section 1.2.1, the $\mathrm{LiNbO_3}$ molecular formula assuming the presence of $y$ moles of antisites is $\mathrm{Li_{1-5y}Nb_{1+y}O_3}$. As

| Sample name | $[Li]\,\%$ measured | $[Nb_{Li}]$ $10^{19}cm^{-3}$ | $[Fe_{tot}]$ $10^{19}cm^{-3}$ | $\left[Fe^{2+}\right]$ $10^{18}cm^{-3}$ | $\left[Fe^{3+}\right]$ $10^{19}cm^{-3}$ | $R\,\%$ |
|---|---|---|---|---|---|---|
| C/1.8/19.0 | $48.45 \pm 0.03$ | $19.0 \pm 0.4$ | 20.9 | $2.4 \pm 0.1$ | $1.8 \pm 0.1$ | $13 \pm 3$ |
| C/1.8/17.5 | $48.58 \pm 0.03$ | $17.5 \pm 0.4$ | 20.9 | $3.1 \pm 0.2$ | $1.8 \pm 0.2$ | $17 \pm 3$ |
| C/1.9/6.4 | $49.49 \pm 0.03$ | $6.4 \pm 0.4$ | 20.9 | $1.5 \pm 0.1$ | $1.9 \pm 0.1$ | $8 \pm 1$ |

Table 4.3.3.: Sample series C. Summary of parameters for the group of samples having the different composition and similar total iron concentration used for continuous-wave measurements. The reduction degree is defined as $R = [\mathrm{Fe}^{2+}]/[\mathrm{Fe}^{3+}]$.

a consequence, the ratio $X_C$ is given by:

$$X_C = \frac{(1-5y)}{(1-5y)+(1+y)} \tag{4.3.3}$$

Solving for $y$, the moles of antisites present into one mole of LN can be calculated in a straightforward manner by:

$$y = \frac{2X_C - 1}{4X_C - 5} \tag{4.3.4}$$

To transform the molar concentration into volume concentration it is sufficient to multiply it by $1.88 \times 10^{22} cm^{-3}$. The results of this characterization is summarized in the second column of table 4.3.3.

# 5. Experimental techniques

The photo-electrical transport properties of samples described in previous chapter were determined by two distinct experimental approaches. The first one, carried out at the Osnabrück University (Germany), is based on the Light-induced Absorption spectroscopy (LIA) which has been proved in oxide dielectrics ($LiNbO_3$, $TiO_2$, ZnO, ... ) to successfully connect the build-up and decay of a transient absorption to the formation and disappearance of short-lived small polarons, upon nanoseconds pulses light exposure. This *transient* measure concerns the study of the mean lifetime of polarons and their interplay during the hopping as a function of the temperature. The second characterization, carried out in the Physics and Astronomy Department of Padova University, concerns the study of photo-generation and transport properties of polarons, under *continuous-wave* illumination conditions as a function of temperature, through the study of the photo-galvanic current $J_{pg}$ and the photoconductivity $\sigma_{ph}$. The setup used for this latter characterization was assembled, tested and automatized during the first year of work and it is based on photorefractive effect and digital holographic technique, i.e. the acquisition and processing of holograms by a digital sensor. In this chapter the two setup are discussed.

## 5.1. Transient measurements

### 5.1.1. Absorption and light-induced absorption

The transmission of light through a material of thickness $d$ can be described, omitting scattering and reflection losses, by Lambert-Beer's law:

$$I(\omega, t, d) = I(\omega, t, d = 0) \cdot e^{[-\alpha(\omega,t)\cdot d]} \tag{5.1.1}$$

where $I(\omega, t, d = 0)$ and $I(\omega, t, d)$ are the incident and transmitted light intensities, respectively and $\alpha(\omega, t)$ the frequency-dependent absorption coefficient. The absorption of a crystalline material is divided into two parts: a fundamental absorption $\alpha_0$, and the sum of the absorptions of all photosensitive centres $\alpha_i$. Examples for such centres in $LiNbO_3$ are metastable small polarons (see chapter 2). The fundamental absorption is originated from the electronic transitions between valence band and conduction band and here it is assumed that it does not depend on the experimental conditions (time, illumination, etc.), but solely on the light frequency $\omega$. On the other hand the absorption

of the different centres may well depend on time, temperature and illumination:

$$\alpha(\omega,t) = \alpha_0(\omega) + \sum_i \alpha_i(\omega,t) \tag{5.1.2}$$

The absorption by photosensitive centres is the product of the respective absorption cross sections $s_i(\omega)$ and their time-dependent number densities $N_i(t)$, with $i = F,\ P,\ Fe,\ H,\ BP,\ ...$:

$$\alpha_i(\omega,t) = N_i(t)\cdot s_i(\omega) \tag{5.1.3}$$

If the number densities of the different centres are changed, e.g., upon intense light illumination, one may split $N_i(t)$ into a time-independent and a time-dependent part. This leads to

$$\alpha_i(\omega,t) = [N_{0,i} + N_{li,i}(t)]\cdot s_i(\omega) = \alpha_{0,i}(\omega) + \alpha_{li,i}(\omega,t), \tag{5.1.4}$$

where $\alpha_{li,i}(\omega,t)$ is the time-dependent *light-induced absorption change* (or simply *light-induced absorption*) for the respective centre. Combining Eqs. 5.1.4 and 5.1.2 one obtains the formula for the time-dependent total absorption, namely

$$\alpha(\omega,t) = \alpha_0(\omega) + \sum_i \alpha_{0,i}(\omega) + \sum_i \alpha_{li,i}(\omega,t) = \alpha(\omega) + \alpha_{li}(\omega,t). \tag{5.1.5}$$

Thus the total absorption of the crystal can be described as a sum of the steady-state absorption $\alpha(\omega)$ and the light-induced absorption $\alpha_{li}(\omega,t)$. In order to get the light-induced absorption from experimental data one may rewrite Lambert-Beer's law using equation 5.1.5:

$$I(\omega,t,d) = I(\omega,t\le 0,d=0)\cdot exp[-\alpha(\omega)\cdot d]\cdot exp[-\alpha_{li}(\omega,t)\cdot d] = \tag{5.1.6}$$

$$= I(\omega,t\le 0,d)\cdot exp[-\alpha_{li}(\omega,t)\cdot d]$$

from which the formula for the light-induced absorption is obtained:

$$\alpha_{li}(\omega,t) = -\frac{1}{d}\cdot ln\left[\frac{I(\omega,t,d)}{I(\omega,t\le 0,d)}\right]. \tag{5.1.7}$$

The important measures are thus the sample thickness $d$ and the intensities of the transmitted probe light prior to the laser pulse $I(\omega,t\le 0,d)$ and after the pulse $I(\omega,t,d)$. Usually light-induced absorption changes are transient, i.e., they vanish after a certain time, showing characteristic decay curves $\alpha_{li}(t)$. It is possible to deduce information about the examined material from these time spectra, especially about charge-transport processes. It is important also to notice that $\alpha$, obtained from 5.1.7, gives an information only about the *variation* of the population with respect to the steady state situation at $t < 0$. The technique employed here exploits a pump-probe setup employing ultrashort ns pulses, so that optically induced short-lived small polarons can be generated

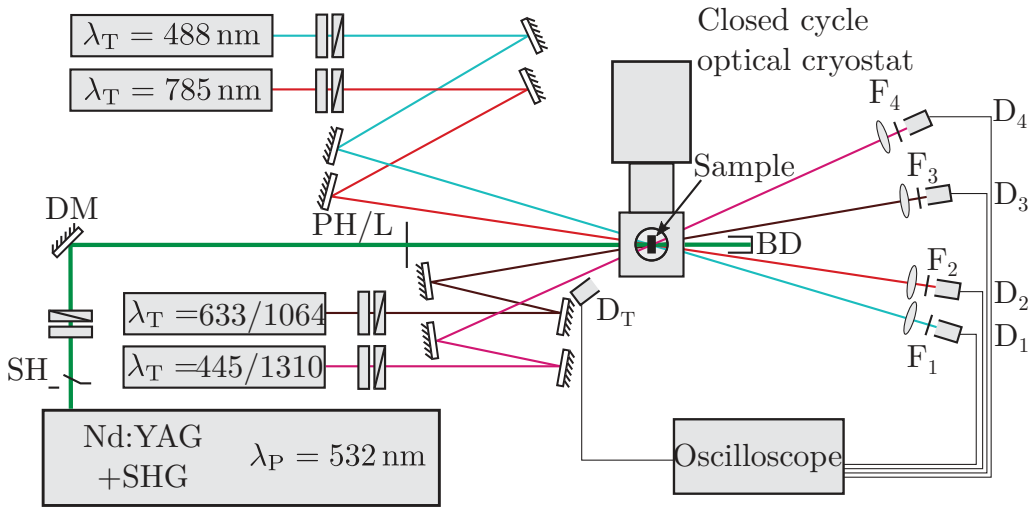


Figure 5.1.1.: Schema of setup for measurements of light-induced absorption changes. Legend: shutter (SH), dichroich mirror (DM), pinhole (PH), lens (L), filters ($F_1$, $F_2$, $F_3$, $F_4$), PIN diode detector ($D_1$, $D_2$, $D_3$, $D_4$), trigger diode ($D_T$).

with the pump laser and subsequently studied optically by probe lasers. In this case different probe lasers are used to exploit the particular absorption features of the different polaron centres to obtain some selectivity to the types of polaron and to their evolution.

### 5.1.2. Experimental setup and analysis

The experimental setup for the measurement of light-induced absorption changes is reported in figure 5.1.1. The laser source is a Q-switched Nd:YAG frequency-doubled at $\lambda = 532\,\text{nm}$ with a pulse duration of $FWHM = 8\,\text{ns}$ and a maximum pulse energy of $E_{max} \approx 290\,\text{mJ}$. The laser is operated solely in 10 Hz mode and single pulses are selected by a computer-controlled fast shutter (SH). In order to obtain different pulse energies an intensity-adjuster is applied, consisting of a $\lambda/2$ - retardation plate and a Glan-Thomson laser polariser. Both optical components are mounted in motorized rotation stages allowing for arbitrary adjustment of both pulse energy and light polarization with constant pulse duration. Four ordinary polarized continuous wave probe lasers enabled a simultaneous time-resolved detection of the changes in the absorption at different wavelengths ($\lambda = 445\,\text{nm}, 488\,\text{nm}, 785\,\text{nm}, 633\,\text{nm}, 1310\,\text{nm}$) as close as possible to the maximum of the absorption band of different type of polarons 2.1.2. The probe beams impinge on the sample with an angle of about 5° relative to the surface normal. The probe light intensity is chosen as low as possible to avoid any perturbation in the polaron population. Typical values are about $160\,\text{MW/cm}^2$, corresponding to a power of 5 mW. The intensity of the transmitted probe light is detected after the sample by Si-PIN diodes in the visible and InGaAs-PIN diodes in the infrared spectral range ($D_1$, $D_2$, $D_3$, $D_4$) and recorded by a fast digital storage oscilloscope. Diodes are preceded

by coloured glass edge filters and interference laser-line filters to avoid the detection of undesired wavelengths. Integrated amplifier circuits assures a voltage signal directly proportional to the output current of the diodes and in this way signals obtained from this diode-amplifier system are proportional to the incident light intensity. According to formula 5.1.7 it is not necessary to know this proportionality constant because does not appear in the expression for $\alpha_{li}(\omega, t)$. An additional Si-PIN diode ($D_T$) detecting the scattered pump light is used to trigger the measurement. Pulsed lasers emit strong electromagnetic pulses originating from both flash-lamp bursts and Q-switching that can severely damage any electronic devices and affect measured signals. In order to minimize this effect diode-amplifiers systems are encapsulated in braze tubes and all signal cables are kept as short as possible. Electromagnetic pulses are also transmitted via the metallic optical table, so that every element on it has to be electrically isolated.

For the purpose of the temperature-dependent measurements of $\alpha_{lia}$ two different sample holders are employed, according to the temperature range. In the case of low temperature measurements, the sample is mounted on a helium cryostat, which permits to control the temperature in the range between 100 and 300 K. In the high temperature regime a two-stage Peltier stack is used. It is clamped on a water cooled aluminium block upon which a copper plate is fixed with thermal adhesive. Using a PID temperature control and a Pt100 resistance temperature sensor it is possible to adjust the sample temperature between 10°C and 150°C with an overall accuracy of one degree.

A typical light-induced absorption spectrum results from the merging of three spectra collected in three different time windows. The first time range goes from hundreds of ns to 0.1 ms with a fix resolution of 1 ns; the second goes from 0.1 ms to 0.1 s with a fix resolution of 1 ms; the third one is chosen so that the complete relaxation of $\alpha_{lia}$ is recorded and its time resolution is decided accordingly. Typical value of the second range are $10 - 100$ s according to the temperature. In order to improve the signal-to-noise ratio, every time range is recorded four times and the averaged is computed.

## 5.2. Continuous-wave Measurements

This characterization is conducted in the regime of low light intensities in the validity regime of Kukhtarev –Vinetskii model with one-photoactive centre that in our case is $Fe^{2+}$, on congruent samples with different iron concentration, (sample series B), and on samples having different stoichiometry but with the same iron concentration (sample series C). In addition these quantities are computed in function of the temperature, in the regime between 100 K and room temperature. The technique here used exploits the pronounced photorefractive effect of Fe:LN to characterize the material properties. The main advantages with respect to direct photoelectrical techniques are that it allows the measurement of very small currents without special need for sample preparation (no electrical contact or sophisticated electrometer are needed). This technique is also very well suited to perform *in situ* measurement such as the ones required here. The idea

is to activate, using a low power cw laser, a photogalvanic current inside the material. This process leads to the formation of a space charge field inside the sample, that can be visualized as a refractive index variation inside the material. Therefore, by measuring the refractive index variation as a function of time, one can obtain the dynamics of the space charge field build up and from this calculate the sample photoconductivity, the photogalvanic current and the saturation value of the space charge field.

### 5.2.1. Space charge field recording

#### Transparent samples

As discussed in Sec. 1.7, for some specific illumination patterns it is possible to find analytical solutions to the Kukhtarev equations. In this case we choose to use a 1-D illumination profile, which is assumed to be uniform along the vertical direction and to have a Gaussian profile in the horizontal one, as sketched in figure 5.2.1. Neglecting beam diffraction and absorption, the intensity profile is thus given by Eq. 1.7.13, here reported for reader's convenience:

$$I(x) = I_0 \exp\left(-\frac{x^2}{2w^2}\right)$$

In this case, the space- and time- dependent evolution of the space charge field is given by [55]:

$$E(x,t) = -E_{sat}\left[\frac{I(x)}{I(x)+I_D}\right]\cdot\left[1-\exp\left(-\frac{t}{\tau_d(x)}\right)\right] \tag{5.2.1}$$

where we made use of the "local" approximation [54], which consists in using the solution of the Kukhtarev equations for the case of uniform illumination (see Sec. 1.7) also in the case of a slowly varying illumination profile, provided that the intensity - dependent quantities are expressed in terms of the "local" intensity value. Therefore (see Eqs. 1.7.10 and 1.7.11):

$$\tau_d(x)^{-1} = \frac{\sigma_{ph}(x)}{\varepsilon\varepsilon_0} = \frac{e}{\varepsilon\varepsilon_0}\mu_e\tau s N\phi\frac{I(x)}{h\nu}$$

Due to the electro-optic effect, the space charge field is readily mapped into a refractive index variation $\triangle n(x,t) = \frac{1}{2}r_{33}n_e^3E(x,t)$. Here $r_{33}$ is the pertinent component of the electro-optic tensor (Sec. 1.4) and $n_e$ is the extraordinary refractive index at the probe wavelength. In our setup (see next section) what is measured is the total phase shift accumulated by an optical wave travelling through the modified refractive index region, compared to the unchanged sample, so that:

$$\Delta\varphi = \frac{2\pi}{\lambda}d\Delta n \tag{5.2.2}$$

where $d$ is the sample thickness and $\lambda$ is the wavelength of the probe laser.

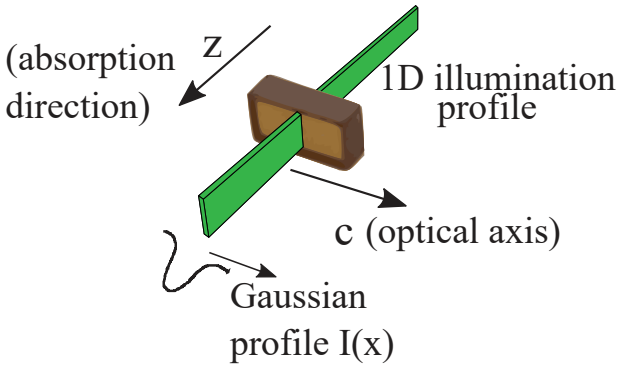


Figure 5.2.1.: 1D illumination scheme on the sample used for photorefractive measurements. The vertical direction is assumed to be uniform while the horizontal one have a Gaussian profile. The absorption direction, discussed later in paragraph "Absorbing sample", is also reported.

### Absorbing samples

Eq. 5.2.2 is valid only if the intensity profile is not changing along the propagation distance, i.e. $\alpha d \ll 1$, which is not true in the case of absorbing samples. If absorption is taken into account, the expression for $I(x)$ in eq. 5.2.1 must be substituted with:

$$I(x,z) = I_0 \exp\left(-\frac{x^2}{2w^2} - \alpha z\right)$$

where $\alpha$ is the absorption coefficient, measured in Sec. 4.3.1. This gives a $z$ dependence to $E(x,z,t)$ and therefore to $\Delta n(x,z,t)$. By integrating along the sample thickness:

$$\triangle\varphi\,(x,t) = \frac{2\pi}{\lambda}\int_0^d \triangle n\,(x,z,t)\,dz \tag{5.2.3}$$

and solving the integral in the centre of the illumination profile (assuming $I_0 \gg I_D$) we obtain the value of the phase modulation at $x = 0$, i.e. corresponding to an illumination intensity $I_0$

$$\triangle\varphi\,(0,t) = \frac{2\pi}{\lambda}\triangle n_{sat}\left\{d + \frac{1}{\alpha}\left[E_i\left(\frac{t\,e^{-\alpha d}}{\tau_d(0)}\right) - E_i\left(\frac{t}{\tau_d(0)}\right)\right]\right\} \tag{5.2.4}$$

where $E_i$ is the exponential integral function defined as $E_i\,(x) = -\int_{-x}^{\infty}\frac{e^{-t}}{t}dt$ and $\lambda = 632.8\,\text{nm}$ is the wavelength of the probe laser. It is now possible to fit the experimental results by equation 5.2.4 to extract the following parameters as a function of temperature:

$$\triangle n_{sat} = \frac{1}{2}r_{33}n_e^3 E_{sat} \tag{5.2.5}$$

and

$$\tau_d(0) = \frac{e}{\varepsilon\varepsilon_0}\mu_e\tau s N\phi\frac{I_0}{h\nu} \tag{5.2.6}$$

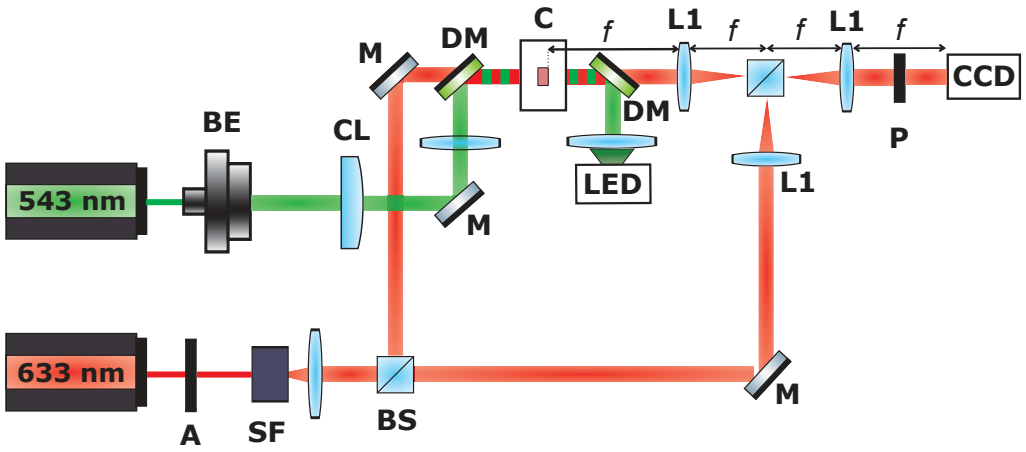


Figure 5.2.2.: Schema of the setup for continuous-wave measurement consisting of: beam expander (BE), cylindrical lens (CL) $f = 150\,\text{mm}$, mirrors (M), dichroic mirrors (DM), cryostat (C), focusing lens (L1) $f = 150\,\text{mm}$, polariser (P), attenuator (A), spatial filter (SF).

### 5.2.2. Digital Holographic setup

The digital holographic technique refers in general to the acquisition and processing of holograms by a digital sensor. This well known technique is applied [91, 92] to Fe:LN to measure the light-induced refractive index change in photorefractive materials. The advantage of this technique compared to other photorefractive characterizations [56] is that it is robust, insensitive to mechanical vibrations and not affected by the beam fanning problem (i.e. the beam self-defocusing) occurring in photorefractive Fe:LN. Those requisites are necessary due to the fact that in our experimental conditions, the measurements can be very slow.

To measure the photorefractive properties of Fe:LN as a function of the temperature, the setup schematically illustrated in figure 5.2.2 has been assembled and tested. The system is based essentially on a pump-probe scheme. The green line has as source a He-Ne laser $\lambda = 543\,\text{nm}$ with a power of $4\,\text{mW}$, expanded (BE) and focused on the sample with the aid of a cylindrical lens (CL), obtaining a vertical blade of light having uniform intensity profile along the vertical direction ($y$) and a nearly – Gaussian one in the horizontal one ($x$). In this condition the beam can be modelled as $I(x) = I_0 exp(-\frac{x^2}{2w^2})$ , where $w$ is the waist beam, in our case equal to $(75 \pm 1)\,\mu\text{m}$. The Rayleigh range of the beam is about 1 cm and the sample is placed in the middle of it, so that the profile of the green beam can be considered to remain almost constant inside the sample. The sample is mounted with the crystallographic $\hat{c}$ direction perpendicular to the light blade and short-circuited by a conductive paste painted on the sample edges. The temperature control is obtained in the range between $100\,\text{K}$ and room temperature with a stability of $0.1\,\text{K}$ by a double-chamber nitrogen optical cryostat with quartz windows. The maximal temperature stability at low temperature guaranteed by the system is three hours. The peak intensity of the green laser arriving on the sample surface has been

Figure 5.2.3.: Example of the interferometric image acquired with the CCD at $T = 240\,\mathrm{K}$ after 20 minutes of exposure to the green beam.

measured by taking into account losses due to the cryostat windows and is given by $I_0 = 280\,\mathrm{W/m^2}$. This value assure that in the subsequent analysis the one centre model approximation can be used and that two-photon process can be neglected. Finally, a green LED of incoherent light covering the whole sample surface is used to "clean" it after each measurement runs, exploiting the reversible feature of the photorefractive effect.

The second part of the setup is a Mach-Zehnder interferometer and it is conceived to monitor the variation of the refractive index as a function of the time. The light source is a He-Ne laser $\lambda = 632.8\,\mathrm{nm}$ having a power of $5\,\mathrm{mW}$ spatially filtered (SF) and attenuated to not alter the $\triangle n$ induced by the green laser. The object beam is superimposed to the green beam and transmitted through the sample using two dichroic mirrors (DM). and the interferometric figure obtained recombining the object and reference beam is measured by a CCD with $1280\times7800$ pixels array (pixel dimension $3\,\mu\mathrm{m}$). The set of lenses (L1) forms a $4\,f$ system and it is set in order to create an image of the sample's output surface at the CCD plane. In this way the measurement is performed in near field conditions, just after the sample surface, so that the fact that the beams can be eventually distorted by the photorefractive effect in the far field is not a problem. Finally a polariser setted in front of the CCD selects only the extraordinary component of $\triangle n$. A typical output of this system is shown in figure 5.2.3 where the fringes distortion is due to the modulation of $\triangle n$ produced by the green beam.

The system is fully computer controlled by a dedicated software, allowing to perform a set of measurement cycles in the same conditions but at different temperatures. In particular the time exposure of the two lasers and of the LED is controlled by shutters, the CCD is directly connected to the PC and takes a picture of the sample according to a time step decided by the user. Also the temperature controller of the cryogenic system is computer-controlled, permitting to monitor the temperature at every time frame.

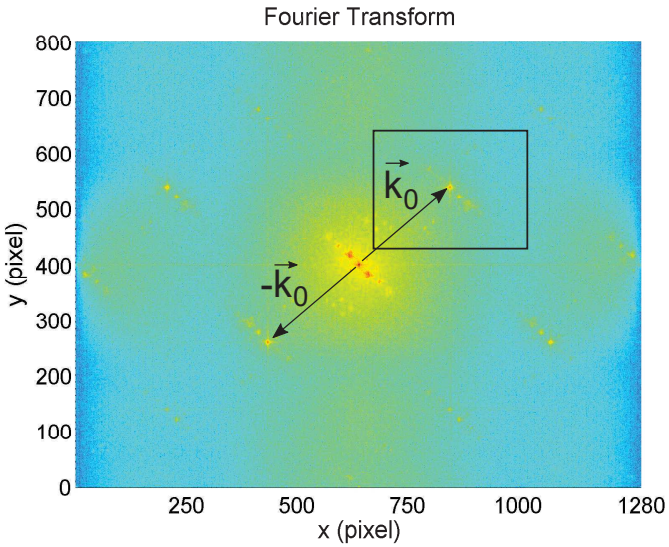


Figure 5.2.4.: Fourier transform of the image 5.2.3 with the applied bandwidth filter on the peak centred at $\mathbf{k} = +\mathbf{k_0}$ .

### 5.2.3. Measurements and analysis

The experimental measurement consists in studying the temporal evolution of the refractive index at a given temperature. To achieve this purpose, interferometric figures, similar to the one reported in figure 5.2.3, are stored in a computer as a function of time, starting from the moment the green laser is switched on. The time of the measurement must be chosen to cover the full temporal evolution of $\triangle n$ and in this way reduce the error in the estimation of the saturation value. Subsequently all the images are analysed with the mathematical algorithm reported in [91], here briefly presented. On the CCD plane, the complex amplitude due to the object beam can be written as:

$$o\left(x,y\right) = o_0 e^{i\varphi(x,y)} \tag{5.2.7}$$

assuming that the crystal is a pure phase object and the variation of the refractive index affect only the phase. On the other hand, the complex amplitude of the reference beam is:

$$r\left(x,y\right) = r_0 e^{i2\pi(\nu_x x + \nu_y y)} \tag{5.2.8}$$

where $\boldsymbol{k_0} = 2\pi \begin{pmatrix} \nu_x \\ \nu_y \end{pmatrix}$ is the wave vector of the reference beam projected on the CCD plane. In this vision the intensity in the CCD plane, collected by images as the one shown in figure 5.2.3, can be described by $I\left(x,y\right) = \left|o\left(x,y\right) + r\left(x,y\right)\right|^2$. By Fourier transforming the interferometric image, three main peaks appear in the frequency space as shown in figure 5.2.4. One centred at $\mathbf{k} = 0$ corresponding to the spatial average of the image (the main peak in the centre of the image), and two satellites symmetrically placed at $\mathbf{k} = \pm\mathbf{k_0}$. These two peaks carry the information on the object creating the

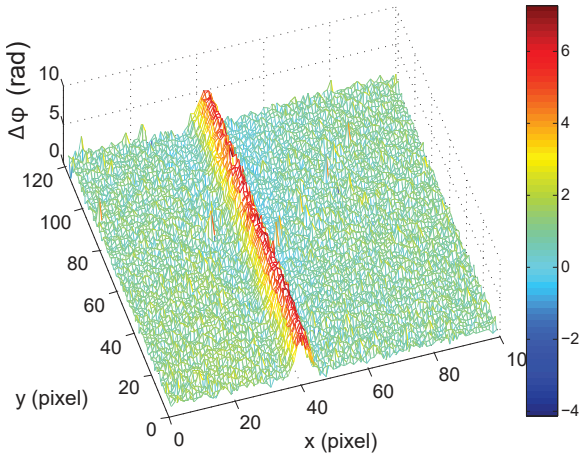


Figure 5.2.5.: Typical phase variation map obtained through Fourier analysis. This particular map is obtained for the sample B/0.82/19.0 at $T = 295\,\mathrm{K}$ after 30 minutes of exposure to the green beam.

$\triangle\varphi$ distortion on the interference fringes. In the particular case of this work, fringes in the real space are tilted at 45° with respect to the vertical light blade. Accordingly, the two satellite peaks are located at the same angle of the Fourier image. All others peaks present in the Fourier transform image 5.2.4 correspond to spurious reflections, creating others interferometric patterns on the real image. The information carried out by the fringes can be isolated from other components applying a bandwidth filter in the Fourier space, i.e. selecting a window centred at $\mathbf{k_0}$. Shifting it in the centre of the frequency space and back transforming the results, it is possible to calculate the complex amplitude of the object beam $o(x, y)$. The 2D wrapped phase of the object beam is then obtained in a straightforward manner by computing

$$\varphi(x, y) = arctg\left\{\frac{Im\left[o(x, y)\right]}{Re\left[o(x, y)\right]}\right\} \tag{5.2.9}$$

Due to the non-invertibility of the arctan function out of the $[0, 2\pi]$ interval, the results are correct *modulo* $2\pi$, i.e. the image is *wrapped*. The 2D phase unwrapping procedure of a real image is not trivial because several sources of errors can affect the result, such as technical noise, under sampling or abrupt phase changes [93]. Additionally an error in processing one single pixel in the wrapped phase image can affects several other pixels within the image provoking the error propagation. A typical wrapped phase image analysed in this work normally contain hundreds of thousands of pixels so a stable algorithm to analyse images is necessary: a phase unwrapping algorithm that processes one single pixel incorrectly may make all the phase information in the image unusable. The most stable algorithm for the type of analysis presented here results is the 2D-SRNCP based on non-continuous paths [94]. In addition the information carried by the matrix is also affected by the phase front shape of the beam, the intrinsic transmittivity of the sample, surface defects etc. so a reference image without

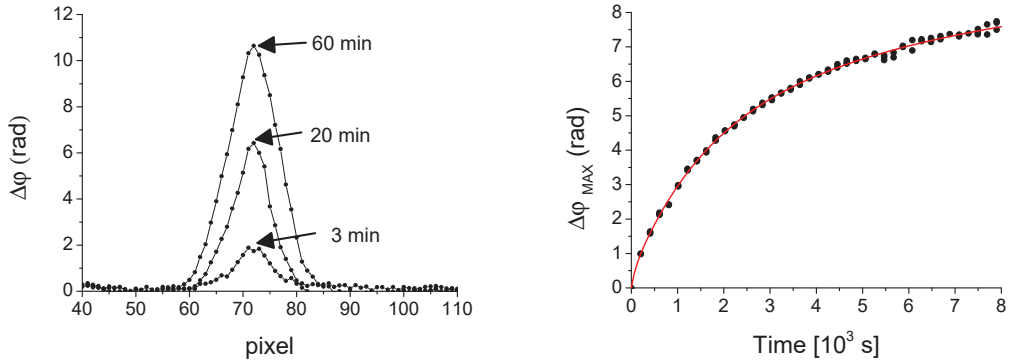


Figure 5.2.6.: (left) 1D profile obtained from the integration of figure 5.2.5 along the vertical direction at $T = 300\,\mathrm{K}$. (right) Time dependence of the maximum amplitude of the phase map obtained at $T = 140\,\mathrm{K}$, the red line is a fit with Eq. (5.2.4). Both images are extracted from the analysis of the near stoichiometric sample C/1.94/6.39 .

$\triangle n$ modification has to be acquired as background and subtracted from others images to overcome this problem.

All this procedure giving the $\triangle\varphi\,(x, y, t)$ map as a function of the time was completely automatized in Matlab. A typical result is presented in Figure 5.2.5. The phase profile is integrated along the vertical direction to improve the signal to noise ratio,obtaining a 1D profile $\triangle\varphi\,(x, t)$(figure 5.2.6 left). This procedure is repeated for all the frames recorded during the exposure of the crystal to the beam. The resulting set of 1D profile are fitted one by one with a peak function to determine precisely the peak maximum $\triangle\varphi\,(0, t)$ as a function of the time, obtaining graphs as the one reported in the right side figure 5.2.6. Those data are fitted by Eq. 5.2.4 to obtain $\triangle n_{sat}$ and $\tau_d(0)$ as a function of temperature. We stress here that if the same datasets were fitted by Eq. 5.2.2 an evident misfit would have been present in the long time part of the curve and the resulting parameters would have been affected by a large systematic error, especially in the determination of $\tau_d(0)$.

# Part III.

# Results

# 6. Transient measurements

The first task to undergo before any modelling of the transport phenomena is to establish what is the role played by the different polaronic centres. Indeed up to this date, polaron formation and decay is described by models restricted in terms of certain temperature ranges, stoichiometry and dopings [66, 71, 95] which, though consistent in itself, reveal serious inconsistencies when connected. The restrictions of these models naturally contradict to the demand of a comprehensive microscopic model for lithium niobate.

In particular in the first part of this chapter, an extension at low temperature of the Herth model [66], describing the behaviour of Fe:LN samples for the conditions adopted in this study, is discussed.

Having established the general scenario of our system, in the second part of the chapter, transient measurements are analysed with the Monte Carlo simulations to tune the microscopic parameters of the hopping frequency rate, such as the orbital length and the polaron energy.

## 6.1. Light induced absorption results

In Fig. 6.1.1 LIA measurements on the samples series A, characterized by an increasing concentration of deep traps, is shown at $T = 298\,\mathrm{K}$ and $198\,\mathrm{K}$, probing simultaneously the transient absorption at different combination of the wavelengths 488, 445, 785, 633, 1310 nm. The pump intensities in the various experiments were adjusted to maximize the signal to noise ratio of the experimental decay: A/1.84/19.0: $I \sim 100\,\mathrm{MW/cm^2}$; A/0.5/19.0: $I \sim 40\,\mathrm{MW/cm^2}$: A/0.36/19.0 $I \sim 60\,\mathrm{MW/cm^2}$; A/0.87/19.0 $I \sim 200\,\mathrm{MW/cm^2}$. For what concerns the sample A/0.36/19.0, whose results are not reported, the 785 nm probe shows a signal similar to the one reported for other samples while the signal at 488 nm remains below the limit of detectability.

All the data demonstrates the previously reported behaviour: after the pulse, a marked increase of the absorption is detected at all the probe wavelengths, which decay to the dark value after some time, with a dynamics that depends on the probe wavelength. The amplitude of the LIA signal in the red/infrared correlates directly with the concentration $\left[\mathrm{Fe}^{2+}\right]$ present in the samples (see Table 4.3.1), suggesting that $\left[Fe^{2+}\right]$ is the main source for photoexcitation of the centres probed at 785 nm [86](see 2.4). The blue absorption instead, appears to be almost insensitive to the $\left[\mathrm{Fe}^{2+}\right]$ content.

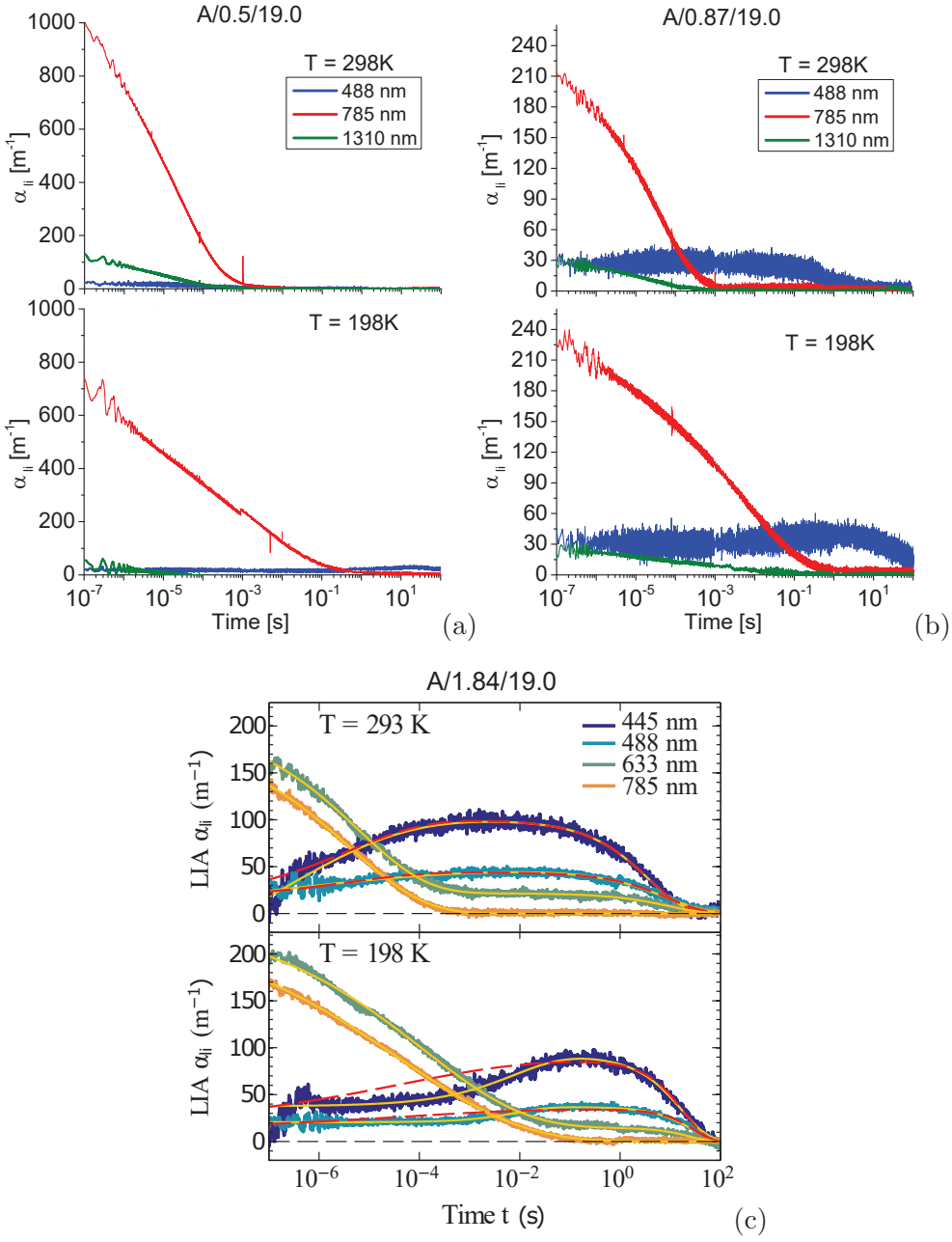


Figure 6.1.1.: Experimental results of light induced absorption on the samples A/0.5/19.0 (a), A/0.87/19.0 (b) and A/1.84/19.0 (c). For each sample, the results at room and low temperature are shown. [Data obtained in collaboration with School of Physics of the Osnabrück University. Figure (c) reprint courtesy of S. Messerschmidt, School of Physics, Osnabrück University]

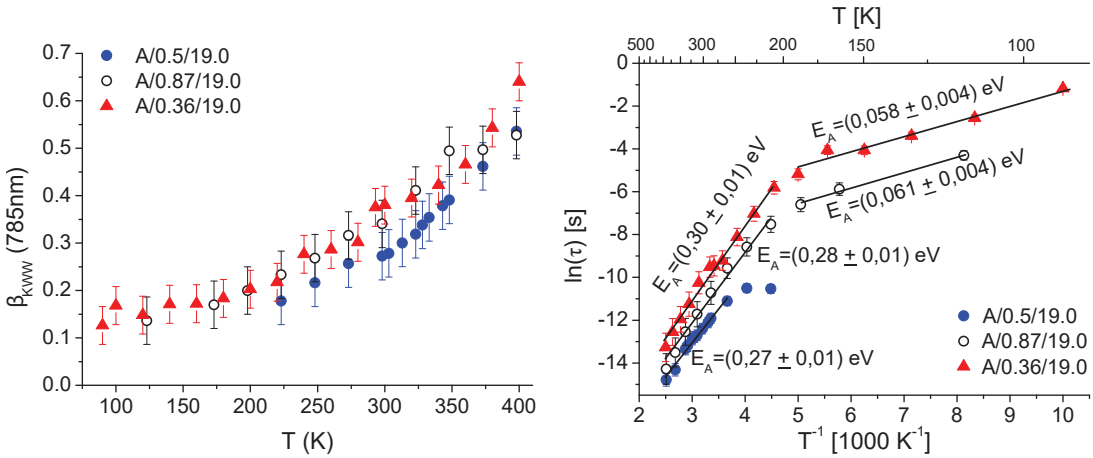


Figure 6.1.2.: Temperature dependence of the stretching factor $\beta$ (left). Arrhenius plot of the characteristics time $\tau$ (right) for the wavelength of 785 nm obtained from fitting with KWW-function of LIA decays on samples A/0.36/19.0, A/0.5/19.0 and A/0.86/19.0 [97].

At room temperatures, the transient absorption in the red spectral range vanishes almost completely within a few milliseconds, while the absorption in the blue spectral range increases in nearly the same period of time.

At $T = 198\,\mathrm{K}$, the curve dynamics are slowed down. However in the blue spectral range a striking new feature is revealed in the shape of the decays. This signal is not only slowing down but appears also stretched, so that after the pump pulse, a constant non-zero absorption change is observed at 445 nm and 488 nm up to the millisecond time regime, followed by a significant increase of $\alpha_{li}$ in the time regime where the red absorption has almost vanished completely. The blue absorption signal vanishes to zero after a duration of tens of seconds.

The observed decay spectra are in general described using an empirical stretched exponential function, named after Kohlrausch, Williams, and Watts [96]. This so-called KWW function is given by:

$$\alpha_{li}(t) = \alpha_{li}^{0} exp[-(t/\tau)^{\beta}] \tag{6.1.1}$$

where $\alpha_{li}^{0}$ is the absorption coefficient at $t = 0$ (not to be confused with the experimentally determined amplitude at the beginning of the time window of our data), $\beta$ is the stretching factor $0 < \beta < 1$, where $\beta = 1$ denotes the case of a mono-exponential relaxation and $\tau$ the characteristic lifetime. Berben *et al.* [31] were the first to apply equation 6.1.1 or a weighted sum of up to two KWWs to describe the decay of $\alpha_{li}(t)$ in $LiNbO_3 : Fe$. In addition they observed that this stretched exponential decay is not a peculiarity of $LiNbO_3 : Fe$, but it is common to a range of doping elements.

**785nm** According to previous absorption measurements on small polarons [31, 77] the absorption at 785/633 nm is attributed mainly to the presence of $Nb_{Li}$ (See table

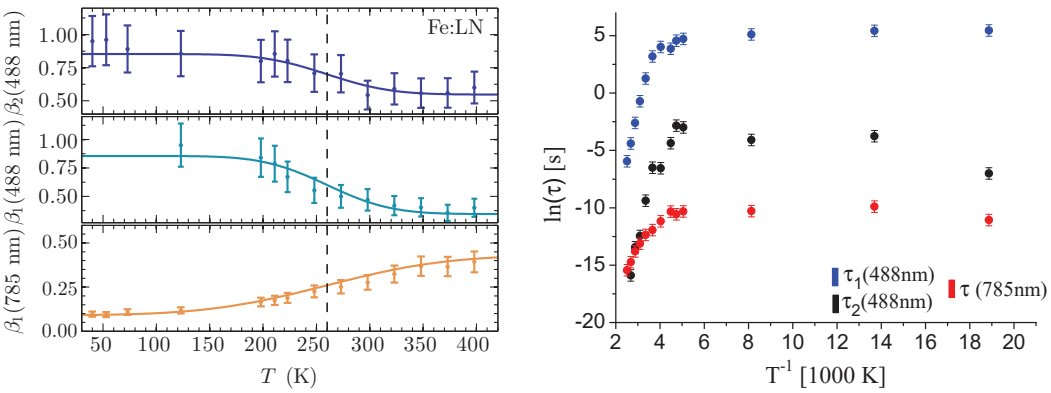


Figure 6.1.3.: Temperature dependence of the stretching factor $\beta$ (left) and the characteristics time $\tau$ [97] (right) obtained from fitting with KWW-function of LIA decays on sample A/1.84/19.0 .[Left plot reprint courtesy of S. Messerschmidt, School of Physics, Osnabrück University]

2.1.2). This curve can be fitted by a single KWW, as it is shown for sample A/1.84/19.0 in Fig. 6.1.1 (c). Repeating this analysis on samples A/0.36/19.0, A/0.5/19.0 and A/0.86/19.0 we obtain the values of $\beta(785\,\text{nm})$ and of $\tau(785\,\text{nm})$ in the whole temperature range (Fig. 6.1.2). It can be seen that $\beta(785\,\text{nm})$ shows an increasing trend with the temperature for all the samples. The temperature dependence of the characteristic time is expressed in an Arrhenius plot, where a slope break is visible for all the samples, at a temperature between 200 K and room temperature.

**488/445nm** The probe wavelength of 488/445 nm according to absorption cross section of the different polarons (see Table 2.1.2), is sensitive to $Fe^{2+}$, $Nb_{Li}^{4+}$, bipolarons and hole polarons. Due to this polaron mix these wavelengths show a more complicated behaviour, as it is reflected by the non trivial shape of $\alpha_{li}$ which initially increases and after decreases. This signal can be described as a sum of two stretched exponential functions:

$$\alpha_{li}(t) = \alpha_1^0\, exp[-(t/\tau_1)^{\beta_1}] + \alpha_2^0\, exp[-(t/\tau_2)^{\beta_2}] \tag{6.1.2}$$

This wavelength has been studied in more detail in sample A/1.84/19.0, due to an improved signal to noise ratio which allowed to obtain a reliable fit at these wavelengths. In this case, the most striking result is a different trend for the KWW $\beta_1(488/445\,\text{nm})$ and $\beta_2(488/445\,\text{nm})$ exponents of the blue probe as a function of temperature. Contrarily to the exponent of the infrared probe $\beta(785\,\text{nm})$ those exponents *decrease* with the temperature, as shown in Fig. 6.1.3. A second important point arises comparing the fitted parameters of the first (fast) component of the decay at 488/445 nm with the one at 785 nm, as shown in Table

| $T$ (K) | $\lambda_{probe}$ (nm) | $\alpha_1^0$ ($m^{-1}$) | $\tau_1$ ($\mu$s) | $\beta_1$ | $\alpha_2^0$ ($m^{-1}$) | $\tau_2$ ($\mu$s) | $\beta_2$ |
|---|---|---|---|---|---|---|---|
| 293 | 785 | $191 \pm 10$ | $4 \pm 2$ | $0.29 \pm 0.02$ | - | - | - |
| 293 | 445 | $-72 \pm 10$ | $5 \pm 3$ | $0.39 \pm 0.04$ | $99 \pm 10$ | $4 \pm 2$ | $0.61 \pm 0.06$ |
| 198 | 785 | $238 \pm 10$ | $40 \pm 10$ | $0.18 \pm 0.01$ | - | - | - |
| 198 | 445 | $-41 \pm 10$ | $(20 \pm 10) \cdot 10^3$ | $0.52 \pm 0.05$ | $82 \pm 10$ | $20 \pm 10$ | $0.9 \pm 0.1$ |

Table 6.1.1.: Parameters of the KWW functions used to describe the decays at 785 nm and at 445 nmfor the LIA data of the sample A/1.84/19.0 shown in Fig. 6.1.1 (c) [97]. While at $T = 293$ K the first part of the decays in the blue and in the IR seem to have the same characteristic parameters, at $T = 198$ K the two curves are clearly non-compatible.

6.1.1 for the wavelength of 445 nm. At room temperature, the characteristic parameters of the KWW function describing the decay at 785 nm, are quite close to the ones describing the first part of the curve at 445 nm. This suggests that the two curves are somehow related, in agreement with ref. [66] discussed in Sec. 6.2.1. However, the low-T data clearly point out that this similarity is not a general feature, as in these conditions the decay at 785 nm and the first part of the curve at 445 nm are described by two completely different KWW functions. To better illustrate this aspect, in Fig. 6.1.1(c) the fitted functions at 445 nm (solid lines) are compared with a second fit (dashed line) in which the constrain $\tau_1(785\,\text{nm}) = \tau_1(445\,\text{nm})$ is imposed, showing an evident misfit out of experimental incertitude. The same result is obtained for 488 nm.

**1310nm** The probe at 1310 nm is sensitive mainly to free polarons and also to antisite-bound ones (Table 2.1.2). The shape of the decay can also be fitted by a single KWW function and the value of the obtained fitting parameters coincide, within experimental accuracy, to the ones of the curve at 785 nm for all the experimental conditions considered here. This indicates that the absorption at 1310 nm is most probably a replica of the one at 785 nm and therefore that this absorption feature can be attributed to bound polarons. The presence of free polarons could not be detected in our LIA experiments for the conditions reported here.

## 6.2. Discussion: multi-specie polaron transport

### 6.2.1. Polaronic species involved in transport phenomena

The first task to accomplish, before going to a quantitative analysis of the decay curves, is to establish a model for the relaxation process with a clear understanding of the types of polaron involved. We will start by considering the five known species of polaronic centres, namely free ($F$), antisite - bound ($P$), Fe ($Fe$), holes ($H$) and bipolarons ($BP$)

and show that it is not possible to explain the totality of our observations by considering only these ones. We then discuss the possibility that non-optically active self-trapped excitons ($STE$) play a role in transport phenomena and propose an extension of the Herth's model [66] for the recombination path of optically generated polarons.

### Free polarons

As discussed in Section 6.1, from our spectroscopic data we have no evidence of any absorption feature that can be unambiguously attributed to free polarons. This does not mean that free polarons are not playing any role, but simply that their concentration, in the time window considered for our measurement is so weak that they cannot be revealed by LIA. This is in agreement with the study conducted by Sasamoto *et al.* [61], which states that in presence of antisite defects, optically excited free polarons transform completely in bound ones in less than one picosecond. Therefore, the free polarons that are eventually present in our system are very scarce and are due to thermal excitation from deeper states.

### Number densities calculation

The transient absorption at a given wavelength $\alpha_{lia}(\lambda, t)$ is given by the contribution of the different polaronic specie weighted by their respective cross section:

$$\alpha_{lia}(\lambda, t) = \sum_i \sigma_i(\lambda) \cdot \triangle N_i(t) \cdot \tag{6.2.1}$$

where $\triangle N_i$ and $\sigma_i(\lambda)$ are the concentration and the cross section respectively of the $i{-}th$ polaron specie. By considering the signals from several probe wavelengths, $\lambda_1, \ldots \lambda_N$, we can construct the following matrix equation for any fixed time step $t$:

$$\begin{pmatrix} \alpha_{lia}(\lambda_1, t) \\ \vdots \\ \alpha_{lia}(\lambda_N, t) \end{pmatrix} = \begin{bmatrix} \sigma_1(\lambda_1) & \ldots & \sigma_M(\lambda_1) \\ \vdots & \ddots & \vdots \\ \sigma_1(\lambda_N) & \ldots & \sigma_M(\lambda_N) \end{bmatrix} \begin{pmatrix} \triangle N_1(t) \\ \vdots \\ \triangle N_M(t) \end{pmatrix} \tag{6.2.2}$$

Since the cross sections for the different polaron centres are known [77] (See Table 2.1.2), if the number of probe wavelengths is not less than the number of species involved ($N \geqq M$), one can try to invert the matrix and find a quantitative estimate for the concentrations of the different species. The procedure can be repeated for any time step so that finally one can obtain explicitly the evolution of the different species concentration. It is however important to notice that we need to choose *a priori* which polaron species are involved in the transport mechanism. From the setup geometry, the measurements are limited to the use of four probe lasers contemporarily, implying that no more than four polarons types can be considered. Fortunately, as explained in the preceding paragraph, free polarons can be disregarded and, in this hypothesis,

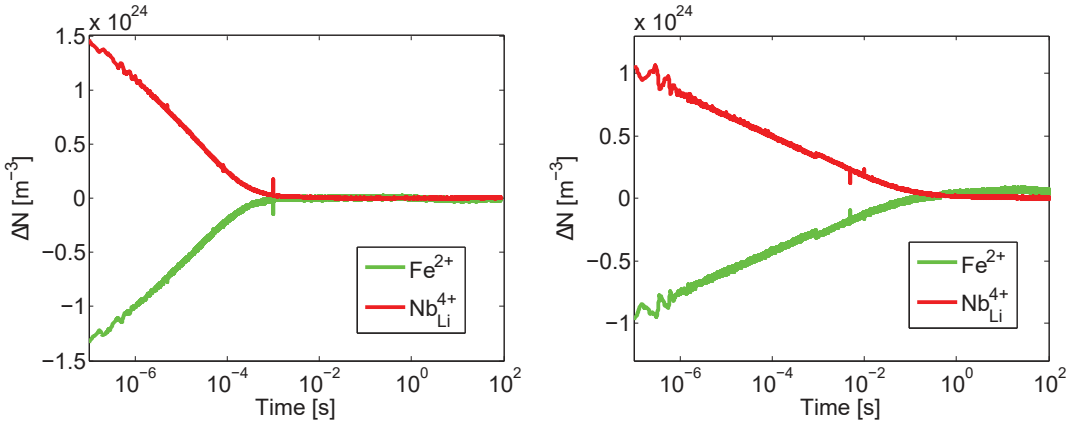


Figure 6.2.1.: Small polaron population variation calculated from $\alpha_{li}(785\,\text{nm}, 488\,\text{nm})$ in sample A/0.5/19.0 strongly reduced (left) at room temperature $T = 298\,\text{K}$ and (right) at low temperature $T = 198\,\text{K}$, assuming a model involving only $Fe^{2+}$ and $Nb^{4+}_{Li}$.

the remaining types of polarons are exactly four. It should be kept in mind that this procedure is strongly affected by the incertitudes in the cross section values, which in some cases are difficult to estimate. We consider therefore this approach only as a semi-quantitative test of our modelling.

### Fe - P model

The simplest model that one can test is the model in which a direct excitation from $Fe^{2+}$ creates $Nb^{4+}_{Li}$ bound polarons (free polaron formation can be considered as a very short intermediate step, as explained above, and be disregarded). The bound polarons then relax back to Fe traps by thermally activated hopping, cancelling out the absorption changes. The motivation for this model is that, in agreement with section 2.4, in reduced samples it may be expected that one-photon excitation from $Fe^{2+}$ is the dominating mechanism. As it is possible that some holes can be created by exciting one electron from the valence band to $Fe^{3+}$ traps by two-photon absorption, we test this model in the most favourable case of the strongly reduced sample (A/0.5/19.0, see Tab 4.3.1). By inverting the matrix equation 6.2.2 using the wavelength of 785 nm and 488 nm with the appropriate cross sections, one find the results reported in Figure 6.2.1. As it can be seen from graphs, while the model seems to give acceptable results at room temperature, at $T = 198\,\text{K}$ an apparent increase of the $Fe^{2+}$ concentration for long times is visible, even if the $P$ population has already disappeared. This result is obviously not physical and cannot be explained by the incertitude in the cross sections, because this would simply affect the graphs with a multiplicative factor. These kinds of results are even more evident in other samples (not shown), so that this simple modelling seems to be applicable only at room temperature and for reduced samples.

**Herth's Model** (Fe, P, H)

The first complete interpretation of results at *room temperature* of transient measurements in Fe:LN samples can be found in the article of Herth *et al.* [66] and sketched on figure 2.4.1. This model considers three polaronic centres involved in the transport: i.e. $Fe$, $P$, $H$ .

In the red spectral range, the initial absorption change $\alpha_{li}(\lambda, 298K)$ is attributed to the formation of $Nb_{Li}^{4+}$ bound electron polarons excited either from the valence band or $Fe_{Li}^{2+}$ to the conduction band by a two-photon or one-photon process, respectively. In detail a significant number of $Fe^{2+}$ centres is emptied by the green pump pulse via one-photon excitation and contemporarily hole polarons are created. The two-photon absorption is, in this way, a second independent generation path of polarons, besides the common $Fe^{2+}$ excitation. The initial absorption in the blue spectral range originates from the sum of a positive absorption change along with the formation of valence band holes plus the $Nb_{Li}^{4+}$ absorption, as well as a negative absorption change, i.e., a transparency, due to the disappearance of $Fe_{Li}^{2+}$. When the $Nb_{Li}^{4+}$ polarons decay (the red signal decreases), the repopulation of empty $Fe^{3+}$ centres leads to an increase of $\alpha_{li}$ in the blue spectral range. The best evidence for this explanation is the good agreement between the decay time of the small bound polaron at 785 nm and the rise time $\tau_1$ observed at 488/445 nm, as observed in Table 6.1.1. Finally from Fe centres they recombine within the lifetime $\tau_2$ with the hole polarons. In $Fe^{3+}$ traps electrons are comparably stable, so they recombine with the hole polarons on the longer time scale of seconds. No direct transition from $Nb_{Li}^{4+}$ to $O^-$ was observed by Herth.

A quantitative check of this model is performed on sample A/1.84/19.0, using $\lambda =$ 785 nm, 633 nm, 488 nm and reported in Figure 6.2.2 (left) at room temperature. Here the sample used has the same doping and reduction degree of the one used by Herth. It can be seen that the change in the concentration of bound polarons is smaller (in absolute) than the one of $Fe^{2+}$ of a factor $\sim 3$. However according to Herth's model, bound polarons are produced both by excitation from $Fe^{2+}$ and from $P{+}H$ dissociation. The bound polaron concentration change therefore must be always larger than that of $Fe^{2+}$.

Another inconsistency comes from the observation, already reported in Table 6.1.1 that the coincidence between the KWW parameters of the signal at 785 nm and the first part of the curve at 488/445 nm does no longer hold by going to low temperature. Additionally, the temperature dependence of the KWW parameters is completely opposed: while $\beta_1$(785 nm) increases upon heating, $\beta_1$(445/488 nm) decreases. These findings invalidate the idea that the initial increase of the blue absorption is the specular process of the decay in the infrared and thus negates the direct repopulation of $Fe^{3+}$ by bound polarons.

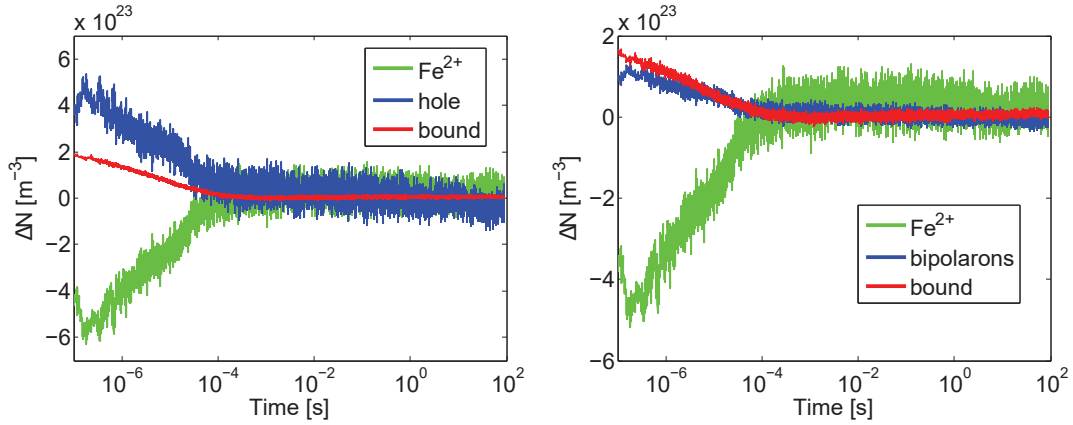


Figure 6.2.2.: Small polaron population variation calculated from $\alpha_{li}$ ($\lambda = 785\,\text{nm}, 633\,\text{nm}, 488\,\text{nm}$) at room temperature for sample A/1.84/19.0 assuming (left) Herth's model and (right) Akhmadullin's model. Cross sections are deduced from figure 2.1.6.

### Akhmadullin's model (Fe, P, BP)

An alternative model, based not on holes but bipolarons, can be tested following the idea proposed by Akhmadullin *et al.* [98], used to explain a change in the electrical conductivity in the low temperature regime in congruent LN. In this view, when two bound polarons come close to each other, one of the two can hop to the $Nb_{Nb}$ site in proximity of the other polaron's antisite $Nb_{Li}$, to create a more stable bipolaron state. The advantage of this model is that it can explain the absorption in the green-blue spectra because bipolaron absorption is sufficiently strong to compensate the transparency following from $Fe^{2+}$ depletion (Table (2.1.2)). Moreover, being negatively charged, BPs fulfil more easily than holes the charge conservation requirement, see Figure 6.2.2 (right). The same result is found with different combination of wavelengths, at low temperatures, and also with other samples. Finally the bipolaron exhibits a higher stability at low temperatures [68], which could explain the long KWW characteristic time of the blue absorption.

Some points however remain unclear also in this case. First of all, to consider this situation, it is necessary to suppose that only the one-photon absorption from $Fe^{2+}$ is the dominant process, even if it seems not to be the case due to the intensity pulse and the sample reduction degree ($R \sim 3\%$). Second, it seems very unlikely that polarons can create the bipolaron metastable state instead of recombining directly with a deep more stable $Fe^{3+}$ which are present in abundant concentration. Third, according to [68] bipolarons formation is very sensitive to the oxidation degree of the sample, while our results seems to be quite independent on the sample reduction degree (Fig. (6.1.1)). Fourth and perhaps conclusive argument against this model, is that the constant non-zero blue absorption at low temperature was found also in a Mg-doped ($[Mg = 6.5] mol\%$) crystal at room temperature, where antisite defects are completely compensated by Mg and therefore bipolaron formation cannot occur [99].

### Self-trapped exciton model

To resume the observations detailed up to this point, it appears that, although highly reduced samples at room temperature can be described considering a simple two-species model (Fe and bound polarons), at least one additional centre has to be considered in the relaxation of light -induced polaron population to provide a more general description valid in all the explored conditions. Its characteristics are:

1. an absorption feature in the blue-green spectral range compensating for the light-induced transparency expected from depletion of $Fe^{2+}$ donors;

2. strongly temperature-dependent relaxation time, making its influence negligible at room temperature in a strongly reduced sample;

3. a dependence from the stoichiometry, to explain results at room temperature on a Mg:LN doped above threshold;

4. a valence preserving the charge conservation;

5. a temperature-dependent $\beta(T)$ explaining the behaviour of $\beta_1\,(488\,\mathrm{nm}, \mathrm{T})$ and $\beta_2\,(488\,\mathrm{nm}, \mathrm{T})$ in equation 6.1.2.

We believe that a new centre can be considered as a possible candidate to explain our data. This centre would be formed by an electron - hole pair self trapped in the same Nb-O octahedron. This centre would therefore be very similar to the self-trapped exciton (STE) described in Section 2.1, therefore formed by an electron - hole pair self trapped in the same Nb-O octahedron, however it has to be mentioned that a luminescence signal in the time range typical of the STE recombination was not detected using our ns - setup. This fact indicates that STEs under consideration do not decay radiatively (dark-STE). It is necessary to postulate that in congruent Fe:LN not all the STE annihilate by emission of a photon and may live for a longer time and decay either by nonradiative annihilation or by dissociation into an electron and a hole polaron. Our view suggests that the population of dark-STEs decays exponentially.

As pointed out by [70] the trapped hole and electron, which a STE consists of, can be excited optically and show a near UV and near-infrared absorption, respectively. In particular its radiative recombinations in LN leads to a broad band spectra centred around 500 nm, therefore it can be assumed that the hole of a STE in LN, similarly to hole polarons, might absorb in the blue spectral range. The same assumption can be done also for the dark-STE so that the hole of a dark-STE might absorb in the blue spectral range, which is one of the criterion for the X centre to fulfil. The increased delay of the absorption in the blue spectral range is observed by both (i) a decrease of temperature and (ii) a doping with the antisite defect compensating material Mg. It is known from luminescence measurements that these conditions largely increase the STE number density [71, 74], fulfilling the second point of the above-mentioned list.

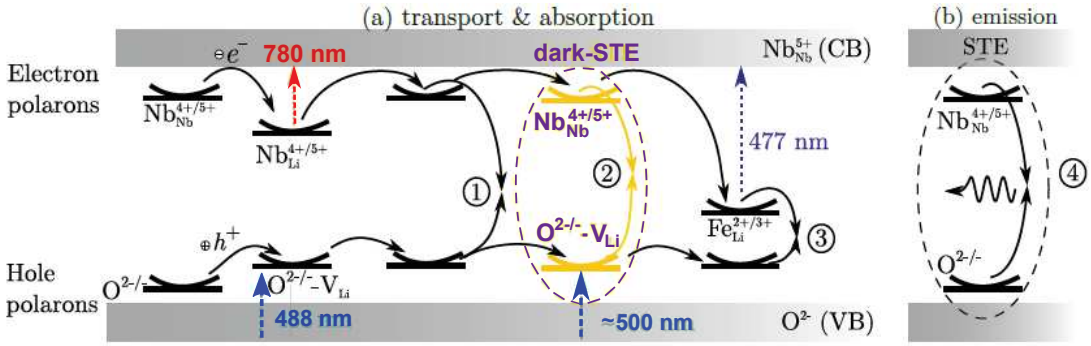


Figure 6.2.3.: (a) Transport and absorption model with included proposed dark-STE as well as (b) the intrinsic light emitting STE for lithium niobate after pulse exposure. The numbers denoting different annihilation processes between holes and electrons. For more details see text. [Reprint courtesy of S. Messerschmidt, School of Physics, Osnabrück University].

The temperature dependent stretching exponent in the initial part of the transient absorption in the blue (Fig. 6.1.3) shows the same behaviour as the one obtained from time-resolved luminescence measurements [75]. Even if these two phenomena occur on very different time scales they reflect the same microscopic mechanism, i.e. a possible superposition of decay paths with different characteristic times. In this sense, STEs show an increase of the beta exponent at low T because local relaxation processes become more probable. We can therefore interpret the increase of $\beta_1(445\,\mathrm{nm})$ by decreasing $T$ assuming that a higher fraction of the electron-hole pairs prefer to annihilate rather than dissociate and hop away.

From a structural point of view we guess that, in comparison with STE, the dark-STE has to be bound to a defect with increasing binding energy. The most probable candidate for the defect centre is the lithium vacancy $V_{Li}$ where the hole is trapped, similarly to the hole polaron. However, it can also be possible that in congruent material the STE is trapped in the neighbourhood of an antisite defect or, in Mg-doped samples, next to an $Mg_{Nb}$-centre [100].

Figure 6.2.3 shows the proposed transport and absorption model with included dark-STE intermediate state as well as the intrinsic light emitting STE. The excitation mechanism is not affected by this modification, an electron is either excited from a $Fe^{2+}_{Li}$ centre or from the valence band to the conduction band by one- or two-photon process respectively, forming an electron polaron and leaving a $Fe^{3+}_{Li}$ or a hole. After the excitation process electrons and holes move through the lattice as free polarons and free holes hopping from one lattice site to another. The most holes are trapped next to an lithium vacancy ($V_{Li}$) and forming bound hole polarons. The electron is captured by a $Nb^{5+}_{Li}$ antisite defect forming a bound polaron which delays the further transport. Four different recombination paths can be distinguished: (1) an electron formerly bound to an antisite defect recombines directly with a hole polaron. (2) An electron formerly bound to an antisite defect and an hole polaron, self trapped in the

same Nb-O octahedron, forms firstly a dark- STE in the presence of a defect, and subsequently dissociates in a bound and a hole polarons. An electron formerly bound to an antisite defect or bound in a dark-STE is thus caught by iron and forms $Fe_{Li}^{2+}$ polarons. (3) Such a $Fe_{Li}^{2+}$ polaron recombines finally with a hole. (4) Furthermore, a STE bound with strong coupling to $Nb^{4+}$ and $O^{-}$ within a single niobium-oxygen-octahedron can annihilate by emitting light (not observed in our samples). We like to note that our approach can also be applied to the findings of Kampfe *et al.* [75] considering the dark-STE as intermediate bound state in the recombination process of small electron and hole polarons. In this case, it may become possible to get insight to a second luminescence decay channel, that was not observed in our measurements.

To conclude this discussion, for the experimental conditions used, in the samples A/0.36/19.0, A/0.5/19.0 and A/0.86/19.0 the main excitation path is the one-photon excitation from $Fe^{2+}$ to create $Nb_{Li}^{4+}$, while the main decay channel is constituted by the opposite process (Fig. 6.2.1). The small discrepancies observed for long times and for weak reduction degrees are ascribed to the presence of dark-STEs. Those STE may recombine and disappear without contributing to the transport. Otherwise they can "store" for a certain time an electron and a hole and dissociate after a given time to saturate a Fe trap and finally recombine with a hole. In this interpretation, this latter process is responsible for the small increase of the blue absorption at long times.

The individuation of the X centre is only the first step of the creation of a new model. A more deeper analysis on the transport mechanism in function of the deep traps and antisite concentration, as well as the external illumination, is now necessary. It could be interesting to understand in which situation one of the proposed recombination path can dominate on the other one. In addition to test quantitatively the proposed models it would be necessary to find the absorption cross section of this centre to complete and/or refine values of figure 2.1.6.

### 6.2.2. Lifetime of small bound polarons

Another important information that can be extracted from $\alpha_{lia}$ is the lifetime of small polarons. As discussed in the preceding sections, a direct solution of Eq. 6.2.2 is not reliable due to the incertitudes in the polaron cross section values. However, according to the discussion of Sec. 6.2.1 it can be considered that $\alpha_{lia}(785\,\mathrm{nm}, t)$ is proportional to the $P$ population $N_P(t)$.

In the analysis of relaxation data for Fe:LN using the KWW equation, generally in literature the lifetime of small bound polarons is taken equal to $\tau$ recovered from the KWW fit function. However it is more meaningful to calculate the average lifetime according to its mathematical definition:

$$\langle\tau\rangle = \int_0^\infty exp\left[-\left(\frac{t}{\tau}\right)^\beta\right] dt = \frac{\tau}{\beta}\Gamma\left(\frac{1}{\beta}\right) \tag{6.2.3}$$

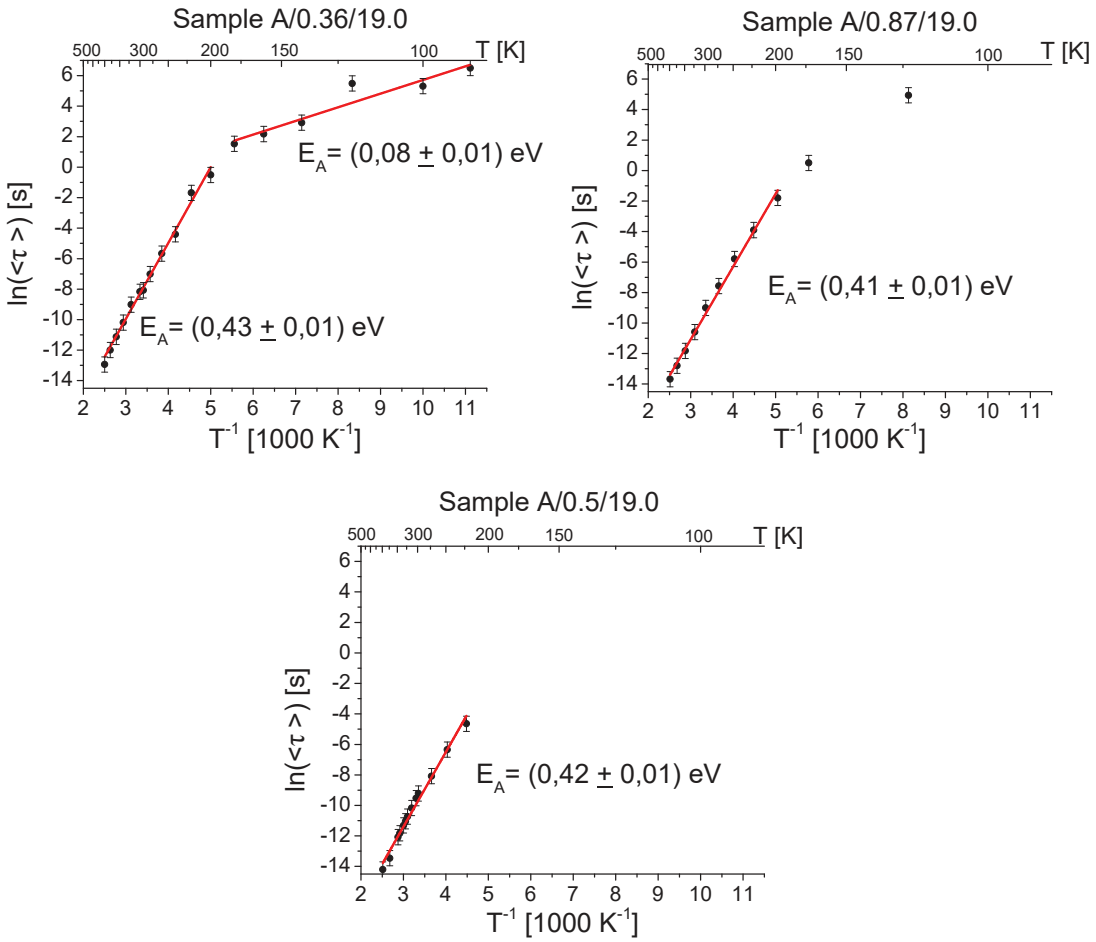


Figure 6.2.4.: Arrhenius plot of the mean life time of $Nb_{Li}^{4+}$ polaron, calculated using data of Fig 6.1.2 [97]. The plot evidence a change in the transport mechanism around 200 K. The high temperature regime is described by an activation energy of $E_A \sim 0.42\,\mathrm{eV}$ indicating a not well defined hopping mechanism (see figure 2.3.1).

where $\Gamma(x)$ is the gamma Euler function. This approach has the advantage of considering both the parameters $\tau$ and $\beta$, reported in figure 6.1.2, allowing for a comparison between decays with different $\beta$ [101].

The result of the $\langle\tau\rangle$ calculation for the three samples of the A series (see Table 4.3.1) is shown in figure 6.2.4 as a function of the temperature in an Arrhenius plot. It is informative to compare this results with the one obtained by the analysis of $\tau$, reported on figure 6.1.2. The difference between the two methods of analysis is more pronounced at low temperature, where the stretching factor is very low if compared to one. In the case of $\tau$ analysis, for example, the energies activation values differ considerably with respect to the one obtained analysing $\langle\tau\rangle$.

The results give evidence of two distinct activation energies with the transition temperature around 200 K for all samples. The high temperature activation energy is the same for all the three samples $U(T > 200\,\mathrm{K}) = (0.42 \pm 0.01)\,\mathrm{eV}$. At low $T$ , it was possible to measure an activation energy only for the less doped sample, providing $U(T < 200\,\mathrm{K}) = (0.08 \pm 0.01)\,\mathrm{eV}$.

The total mean lifetime can be viewed as the sum of the time of each hop, which in turn is the inverse of the corresponding hopping frequency, defined in Sec. 2.3:

$$\langle\tau\rangle = \sum_n \tau_n = \sum_n \nu^{-1}_{i(n)j(n)} \tag{6.2.4}$$

where $i(n)$ and $j(n)$ labels the types of initial and final site of the $n-th$ hop. According to the relaxation model adopted (Sec. 6.2.1), $i$, $j \in [P,\ F,\ Fe]$, so that the activation energy of $\langle\tau\rangle$ cannot in general be defined. It is however clear that if, on average, one specific type of hop occurs more frequently than the others, the activation energy will become closer and closer to the hopping barrier of the specific hop type:

$$\langle\tau\rangle \propto \tau_{0ij} e^{\frac{U_{ij}}{kT}} \tag{6.2.5}$$

where $\tau_0$ is the lifetime of the specific hop *ij*. In this vision, if the slope of the Arrhenius plot corresponds to one of the activation energies of figure 2.3.1, it would be possible to understand the dominant transport mechanism. It can thus be supposed that at low T the the most prominent process are the trapping hops $\mathrm{Nb}^{4+}_{\mathrm{Nb}} \rightarrow \mathrm{Nb}^{5+}_{\mathrm{Li}}$ or $\mathrm{Nb}^{4+}_{\mathrm{Li}} \rightarrow \mathrm{Fe}^{3+}$(expected energies: $U_{FP} = 0.069\,\mathrm{eV}$ and $U_{PFe} = 0.043\,\mathrm{eV}$), in agreement with the preliminary discussion of section 3.3 which pointed out that at low T the polarons are trapped in one single hop. At room and high temperatures, the activation energy appears to be intermediate between the hopping barriers for the hops $\mathrm{Nb}^{4+}_{\mathrm{Li}} - \mathrm{Nb}^{4+}_{\mathrm{Li}}$, $\mathrm{Nb}^{4+}_{\mathrm{Nb}} - \mathrm{Nb}^{4+}_{\mathrm{Nb}}$ or $\mathrm{Nb}^{4+}_{\mathrm{Li}} - \mathrm{Nb}^{4+}_{\mathrm{Nb}}$ ($U_{PP} = 0.290\,\mathrm{eV}$, $U_{FF} = 0.273\,\mathrm{eV}$, $U_{PF} = 0.634\,\mathrm{eV}$) indicating that all these processes are simultaneously taking place. We cannot however exclude that the energy barrier values, computed from published data, may need a refinement. This topic is reported in section 6.4.1, with the aid of a Monte Carlo simulation.

| Sample | $\left[Fe^{3+}\right]^{-1}$ | $[Fe_{tot}]^{-1}$ | $\ln(\tau_0)$ | $\tau_0$ |
|---|---|---|---|---|
| | $10^{-25}\,m^{-3}$ | $10^{-25}\,m^{-3}$ | | s |
| A/0.36/19.0 | 2.77 | 2.70 | $-24.9 \pm 0.4$ | $(1.5 \pm 0.6) \cdot 10^{-11}$ |
| A/0.87/19.0 | 1.15 | 1.05 | $-25.4 \pm 0.5$ | $(9 \pm 5) \cdot 10^{-12}$ |
| A/0.5/19.0 | 1.92 | 0.53 | $-26.1 \pm 0.6$ | $(5 \pm 3) \cdot 10^{-12}$ |

Table 6.2.1.: Prefactors of the exponential term in Eq. 6.2.5 determined from the data of Fig. 6.2.4. $[Fe^{3+}]$ is the $Fe^{3+}$ concentration in the dark, $[Fe^{3+}_{TOT}]$ is calculated assuming that after the pulse, all the Fe traps are empty.

The intercept $\tau_0$ of the linear part of the high temperatures datasets in Fig. 6.2.4 should be inversely proportional to the trap density according to Eq. 1.7.1. Values reported in table 6.2.1 evidence that this is not the case. We believe that this discrepancy can be attributed to the trap refilling effect discussed in Sec. 3.4, i.e. to the fact that just after the pulse the number of total Fe traps is not the one in the dark, since the pulse has emptied the largest part. This is confirmed by the fact that the lifetime prefactor correlates much better with the inverse of the total Fe content. This point will be considered again in Chapter 7.

## 6.3. Monte Carlo analysis of transient absorption decays

The aim of this section is to reproduce by the Monte Carlo code described in Chap. 3 the transient measurements for three different samples having different iron concentrations, belonging to sample series A. As discussed in section 3.6, in our simulation we consider primarily as free parameters the two orbital lengths $a$ and $c$, describing the distance dependence of the hopping frequency for the transport and trapping processes respectively.

The output of the MC code is the population decay of single polaron species. As already discussed in section 6.2.1 to achieve this purpose it is mandatory to convert the LIA signals into the population decay for every polaron species. Unfortunately this task cannot be fulfilled for the moment due to a lack of precise knowledge on the cross section values of the STE and of other centres. However, according to the discussion of Sec. 6.2.1, we may safely assume that in the experimental conditions here adopted, the signal at $\lambda = 785\,nm$ is proportional to the population of $Nb^{4+}_{Li}$ bound polarons, decaying towards Fe traps. This allows comparing directly the population variation resulting from the simulation with the absorption signal at $\lambda = 785\,nm$. Simulation are compared with experimental data in the time range from $10^{-7}$ seconds (the experimental range). Due to the incertitude in the exact cross section value and in the initial value of the absorption curve, which is sensitive to several experimental artefacts, the simulation and the experimental data are normalized to 1 at the initial

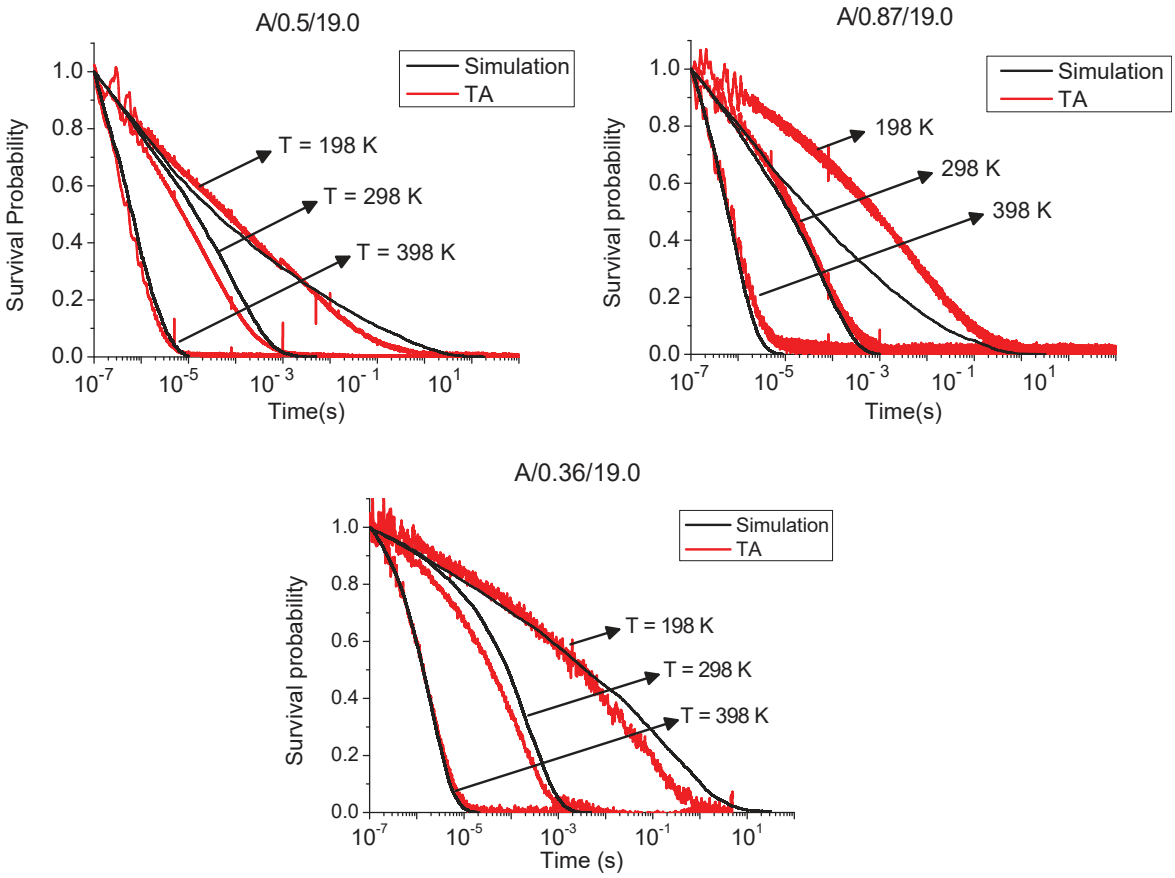


Figure 6.3.1.: Comparison between experimental results [97] (red) and MC simulations (black) for sample series A for three exemplary temperatures.

point.

By comparing the absorption coefficients with the peak photon fluence of our pump, we may consider that all $Fe^{2+}$ ions are likely to be ionized after the pulse [66, 86], so that the initial polaron concentration can be taken to be equal to the $\left[Fe^{2+}\right]$ concentration in the dark. Finally, since the polaron formation time ($< 1$ ps)[61] is much shorter than our pulse duration, we can assume that the polarons present immediately after the pulse are those that were able to perform several (eventually photo-assisted) hops from the position of the initial donor centre, so that their position after several ns can be considered to be completely uncorrelated from the initial photo-generation site. The so-produced light-induced polarons perform a random walk hopping among defective $Nb_{Li}$ sites (bound polarons) or regular $Nb_{Nb}$ sites (free polarons) until they are trapped by a $Fe^{3+}$ ion.

Systematic simulations with different input values for the orbital lengths $a$ and $c$ were performed in order to reproduce the experimental results reported in chapter 5.1 for all the samples and all the measured temperatures with a unique set of parameters. According to the experimental results of [60], the non-adiabatic approximation which our code relies upon is acceptable down to 150 K. However, to be more safe, we decided

to limit the comparison in the temperature range $200\,\mathrm{K} < \mathrm{T} < 400\,\mathrm{K}$.

A satisfactory agreement could not be reached, because at high temperature the simulation curves remained too slow in comparison to experimental ones. To improve the agreement we decided to use also the bound polaron DSE $E_P$ as free parameter. The reason for this choice is that (i) energetic parameters have the largest impact, together with orbital parameters, on the simulation results and (ii) the $E_P$ value reported in Tab. 2.1.1 was calculated assuming for the bound polaron the same phonon energy of the free one, but in fact no precise determination for this parameter is available, taking into account that the bound polaron is a defective site. On the other hand, the energetic parameters for the free polaron and for Fe appear to be well assessed (see Section 2.1) so they will be retained.

In figure 6.3.1 the best result of this procedure is reported. Although some misfits are still present, it should be stressed here that, by using only three parameters, we can correctly reproduce the decay shapes for all the temperatures and trap concentrations, with the only exception of sample A/0.87/19.0 and only for low $T$. The reasons for this disagreement are still not clear. A tentative explanation is connected to the observation that in this sample a pump intensity of $200\,\mathrm{MW/cm^2}$ was used to obtain a sufficient signal, which is significantly higher than the ones used for the other samples. This may somehow invalidate the basic assumptions of our modelling, i.e. that the signal at 785 nm is proportional solely to the $\mathrm{Nb_{Li}}$ population and that $\mathrm{Fe^{3+}}$ are the only recombination centres. In fact the agreement becomes much better in the same sample by increasing the temperature, which may hint that STEs contribute to this wavelength at low temperature. Besides this pathological case, all the other datasets are satisfactorily fitted by the simulation. A better agreement could probably be obtained by allowing more free parameters or using more complex models, but we expect no significant changes in the final values of $a$, $c$ and $E_P$ obtained by our procedure. The resulting set of three free parameters is:

$$E_P = (0.75 \pm 0.05)\,\mathrm{eV}$$

$$a = (1.6 \pm 0.1)\,\text{Å}$$

$$c = (1.5 \pm 0.1)\,\text{Å}$$

Concerning orbitals parameters result, the values are in the range expected from theoretical consideration of section 2.1, indicating that the electron wave-function of free and bound polarons are entirely confined in the oxygen octahedra, confirming their *small polaron* nature.

Another main result is the refinement of the value of $E_P$. The total $\mathrm{Nb_{Li}^{4+}}$ polaron energy is known from spectroscopic data be equal to $M = 2E_P + \varepsilon_P = 1.69\,\mathrm{eV}$, corresponding to $\varepsilon_P = 0.53\,\mathrm{eV}$ for $E_P = 0.58\,\mathrm{eV}$, as discussed in [58]. According to these values, the electron would be strongly bound to the antisite ($\varepsilon_P$) but the energy gained

| | | final site | | |
|---|---|---|---|---|
| | energy in eV | *Free (F)* | *antisite (P)* | *Fe* |
| initial site | *Free (F)* | 0.273 | 0.156 | 0.003 |
| | *antisite (P)* | 0.551 | 0.375 | 0.038 |
| | *Fe* | 1.378 | 1.018 | 0.350 |

Table 6.3.1.: Hopping energy barriers (equation 2.3.8) calculate for no applied electric field. In red color the ones which differ from values of figure 2.3.1 calculated with the new polaron energy $E_P = 0.75\,\text{eV}$.

from the local deformation of the lattice ($E_P$) would be close to the one of a free $Nb_{Nb}$ polaron, being $E_F = 0.54\,\text{eV}$ its deformation-stabilization energy.

Our Monte Carlo results imply that the binding energy has the lower value:

$$\varepsilon_P = (0.2 \pm 0.1)\,\text{eV}$$

This means that the Coulombic defect attraction of the bound polaron is relatively weak. This appears to be reasonable if we consider that the anionic environments of both polarons are very similar (a Nb atom inside an oxygen octahedron). We therefore can expect a similar charge density distribution and a similar Coulombic attraction for the electronic wavefunction. On the other hand, the cationic lattice structure of the two centres is quite different. The $Nb_{Li}$ site "feels" the proximity of the heavy $Nb_{Nb}$ atom, which has been uncovered as origin of the the large relaxation as being computed by the LDA methods in the bipolaron state $Nb_{Nb}^{4+} : Nb_{Li}^{4+}$ [62]. From the width of the $Nb_{Li}^{4+}$ polaron optical absorption band, proportional to $(E_P \hbar\omega_{LO})^{1/2}$(Eq. 2.1.5) our new estimate for $E_P$ gives $\hbar\omega_{LO} = (77 \pm 5)\,\text{meV}$. This is significantly less than the phonon energy of the $NbO_6$ breathing mode (109 meV, i.e. $871\,\text{cm}^{-1}$ according to Raman data [102]). In other words the self-trapping is favoured on $Nb_{Li}$ versus $Nb_{Nb}$ mainly because the surrounding lattice is softer.

The refined energy value allows to recalculate the energetic barriers for the different hopping processes (Table 6.3.1). This table therefore substitutes the one of figure 2.3.1 from now on.

## 6.4. Discussion

### 6.4.1. Hopping transport regimes

In the preceding paragraphs we established that, under low intensity illumination ($I < 10\,\text{MW/cm}^2$), which is the regime of interest for CW lasers, the main role in the transport phenomena is played by $Nb_{Nb}$ and $Nb_{Li}$ polarons hopping until a they are trapped by $Fe^{3+}$ centres. One of the most intriguing question concerns the understanding of the role played by the different types of polarons, by variation of the temperature, or of the $Nb_{Li}$

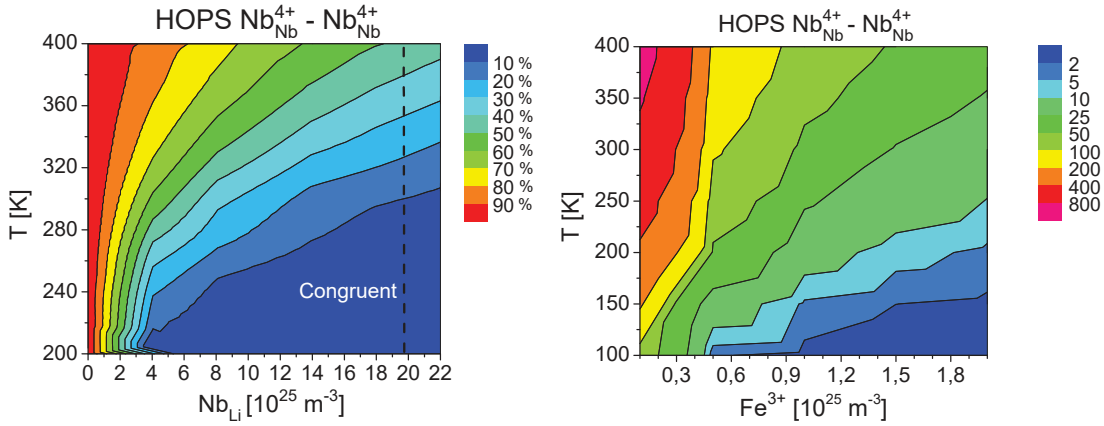


Figure 6.4.1.: (left) $N_{FF}/N_{tot}$ in function of the temperature and [$Nb_{Li}$] concentration for an undoped sample ($[Fe] = 0$). (right) $N_{FF}$ as a function of the temperature and $[Fe]$ concentration for a stoichiometric sample ($[Nb_{Li}] = 0$).

antisites and Fe concentration. With the analysis on the energy activation of the mean lifetime (see section 6.2.2) we got an indication that, depending on the temperature, different hopping processes can take place. It was only possible to conclude that at high temperature a mix transport made by $Nb_{Nb}^{4+}$ free and $Nb_{Li}^{4+}$ bound polarons plays the decisive role, while at low temperature the iron has a greater impact on the results. Their respective parts in light-induced transport are still an open question. The present section aims to study the interplay between these species and to predict which type of transport should predominate, depending on temperature and trap concentrations. This will be done with the help of the Monte Carlo simulation and of the refined microscopic parameters established in Sec. 6.3.

### Free polaron transport

Free polarons are generally believed to be the main charge carrier in LN [58]. To evaluate quantitatively their role in charge transport we can calculate, for an average polaron performing $N_{tot}$ hops from its birth to its death, the fraction $N_{FF}/N_{tot}$ of $Nb_{Nb}^{4+} \rightarrow Nb_{Nb}^{4+}$ hops performed as a free polaron. The calculation is performed by simulating 5000 polarons using the microscopic parameters determined in Sec. 6.3 together with the fixed ones reported in Sec. 3.3. The experimental conditions (antisites and Fe traps concentration and temperature) are varied, to explore the typical range of parameters encountered in standard situations.

In the left side of figure 6.4.1 we investigate the effect of the sample composition and of the temperature on the free polaron contribution to conduction. Here the Fe concentration is set to zero. This situation therefore describe the impact of the stoichiometry or of doping with photorefractive-resistant ions (Mg, Zn, Zr) on the conduction. It can be seen that at room temperature, the reduction of the [$Nb_{Li}$] concentration initially has a small influence on the amount of FF hops. It is necessary to eliminate about

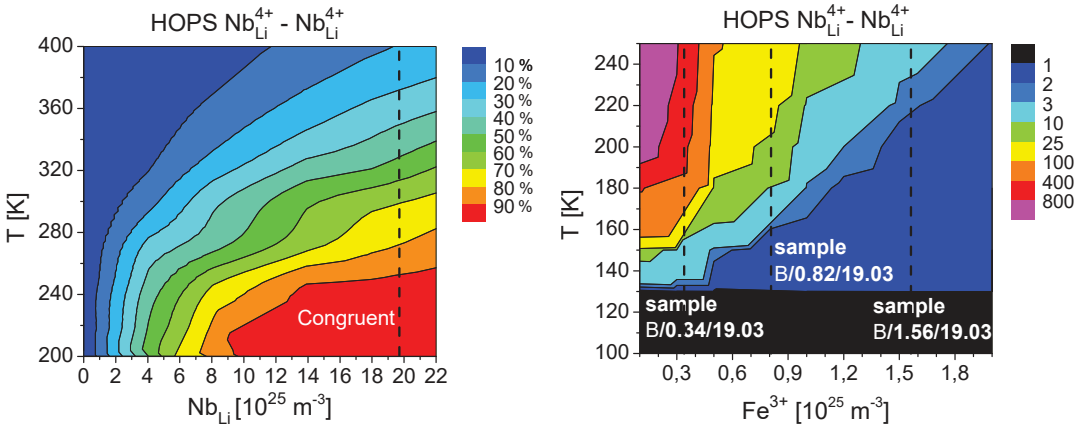


Figure 6.4.2.: (left) $N_{BB}/N_{tot}$ in function of the temperature and antisite concentration for an undoped sample ($[Fe] = 0$). (right) $N_{BB}$ as a function of the temperature and $[Fe]$ concentration for a congruent sample ($[Nb_{Li}] = 19.0 \cdot 10^{25}\,\mathrm{m}^{-3}$). Free polaron contribution has been disregarded for simplicity. Note the different temperature range in the two plots.

the 90% of the antisites before observing a steep increase in the free polaron contribution to the conduction. This result explains quantitatively the origin of the so-called *photorefractive threshold* which is necessary to surpass to observe a marked decrease of the photorefractive effect in undoped LN [1]. The situation is even more extreme at low temperatures and, conversely, more gradual by heating the sample.

In the right side of figure 6.4.1, we consider now the impact of Fe doping from the point of view of free polaron conduction. We consider a stoichiometric sample to distinguish from the effect of shallow [$Nb_{Li}$] traps. The qualitative behaviour is obviously similar. In this case it is interesting to note that at room temperature, even for high Fe concentrations ($2 \cdot 10^{25}\,\mathrm{m}^{-3}$), the free polarons are always able to perform on average several hops before being trapped. This is in contrast, as we will show below, for the behaviour of bound polarons.

### Bound polaron transport

As it has been shown in the above paragraph, when some antisites are present and for not too elevated temperatures, (Fig. 6.4.1 (left)) only a limited percentage of the hops that one polaron performs during its life are of the $Nb_{Nb}^{4+} \rightarrow Nb_{Nb}^{4+}$ type. In Fig. 6.4.2 (left) the same analysis is carried out for $Nb_{Li}^{4+} \rightarrow Nb_{Li}^{4+}$ hops. Here the situation is reversed: if the temperature is not too high and the antisite concentration is close to the congruent one, a large (on average) percentage of the total hops is constituted by direct hops among antisite defects. *This lead us to the important conclusion that in standard conditions, i.e. a congruent material at room temperature (and below), the dominating polaronic specie is the bound polaron, hopping directly among antisite defects.* This situation is completely different with respect to the free polaron case, because bound

| $E_P$ (eV) | $U_{PF}$ (eV) | $U_{FP}$ (eV) | $U_{P,Fe}$ (eV) | $U_{PP}$ (eV) |
|---|---|---|---|---|
| 0.58 | 0.635 | 0.07 | 0.043 | 0.290 |
| 0.75 | 0.551 | 0.156 | 0.038 | 0.375 |
| 0.84 | 0.516 | 0.211 | 0.036 | 0.420 |

Table 6.4.1.: Hopping barriers calculated from equation 2.3.8 for different values of $Nb_{Li}^{4+}$ energy, $E_P$.

polarons hop on a disordered lattice, for which standard diffusion equations (Eq. 2.3.5) may not be valid (see Chap. 8). Two important remarks are necessary: (i) the fact that a large percentage of hops is performed as a bound polaron, does not necessarily mean that charge transport is ruled by bound polarons: free polarons are so much more mobile than bound ones that, even if they are very scarce, they can carry charge in a very efficient way. (ii) Even if some hops are performed as free polarons, their concentration remains negligibly small, because they perform their hops very quickly before being very soon recaptured either by a $Nb_{Li}^{5+}$ shallow trap or by a $Fe^{3+}$ deep trap. Therefore, the number of conversion per unit of time at which free polarons are produced is much slower than the number of conversion per unit of time at which they disappear, so that their equilibrium concentration remains very limited. This is confirmed by our simulations that show that the free polaron population is always close to zero in standard conditions (Fig. 3.4.1) and by our experimental LIA results (see section 6.2.1).

The influence of iron traps on $Nb_{Li}^{4+}$ polarons is shown in Fig. 6.4.2 (right). In this case the contribution of free polaron can be disregarded because this analysis is performed at low temperature for congruent composition, this allow to reduce greatly the computational cost of this simulation. Here the situation is even more dramatic if compared to the free polarons case, because at low temperature, even with a relatively low concentration of deep traps, the bound polaron can perform at most one single jump. The numbers showed in Fig. 6.4.2 (right) are an overestimation because of the soft pair effect (see Sec. 3.1). In other words, the $Nb_{Li}$ polaron can perform in some cases a large number of hops between two close-by antisite defects, without contributing effectively to the transport. In any case, this graph can be used by looking the conditions for which the number of hops become smaller than one. This means that at low temperature, the bound polarons are directly trapped by a $Fe^{3+}$ and the transport process is no longer based on $Nb_{Li}^{4+} \rightarrow Nb_{Li}^{4+}$ hops but on $Nb_{Li}^{4+} \rightarrow Fe^{3+}$. This is in agreement with the results of Fig. 6.2.4 which show a change in the activation energy of the average hopping frequency by cooling down the sample. The measured activation energies are larger than the ones reported in Table 6.3.1. This is not surprising, as the results of the simulations describe an average situation and the case of strictly one single type of hopping process should be regarded as a limit situation. Therefore, the measured activation energy ($E_A = (0.08 \pm 0.01)$ eV) at low temperature in sample

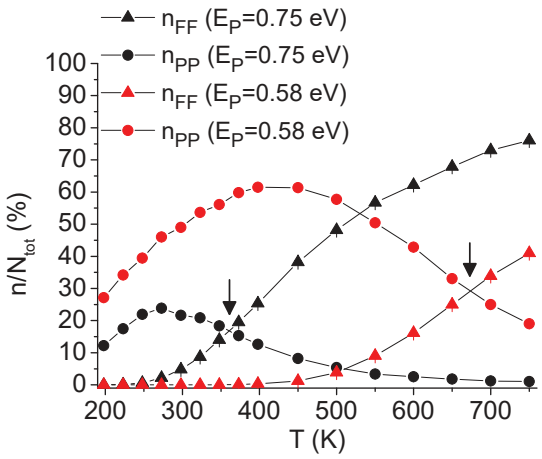


Figure 6.4.3.: Percentage fraction of hops per random walk performed as free ($n_{FF}$) or as bound ($n_{PP}$) polaron for $E_P = 0.75\,\text{eV}$ (black symbols) and for $E_P = 0.58\,\text{eV}$ (red symbols) in sample A/0.5/19.0.

A/0.36/19.0 corresponds to a mix of hopping processes of the type $\text{Nb}_{\text{Li}}^{4+} \rightarrow \text{Nb}_{\text{Li}}^{4+}$ and $\text{Nb}_{\text{Li}}^{4+} \rightarrow \text{F}e^{3+}$, with an apparent activation energy in between the corresponding ones ($U_{PP} = 0.375\,\text{eV}$ and $U_{PFe} = 0.003\,\text{eV}$ respectively).

To conclude this section, we stress here an important observation. If $a$ and $c$ are fixed, the temperature above which one type of hopping processes become relevant with respect to another is very sensitive to $E_P$ through the dependency on the energy barrier of the process (equation 2.3.8). By increasing $E_P$, the conversion barrier $U_{PF}$ for the bound to free hops is decreased, while the trapping barrier $U_{FP}$ from free to bound state would rise and thus reduce the efficiency of $\text{Nb}_{\text{Li}}$ as a free polaron trap (Table 6.4.1). In other words, by increasing $E_P$ we favour the hopping among regular $\text{Nb}_{\text{Nb}}$ sites with respect to antisites $\text{Nb}_{\text{Li}}$ at a given temperature. The significance of this vision stems in the fact that bound and free polarons possess a very different mobility, so that it is important to understand when the conduction becomes bound-polaron or free-polaron dominated. As observed before, the mobility of free polarons is much greater than the one of bound polarons, this explains why the observed decays previously reported in figure 3.6.3 become faster at high temperatures for a larger $E_P$ value. To better illustrate this finding, in Figure 6.4.3 it is shown the percentage of hops performed as a free ($n_{FF}/N_{tot}$) or as a bound polaron ($n_{PP}/N_{tot}$) for sample A/0.5/19.0 assuming $E_P = 0.75\,\text{eV}$ or the value $E_P = 0.58\,\text{eV}$ reported in literature [58]. It can be seen that, with the former value, at room temperature the polarons performs already a 5% of their hops among $\text{Nb}_{\text{Nb}}$ sites and a 22% among $\text{Nb}_{\text{Li}}$ ones, the rest of the hops being "conversions" $\text{Nb}_{\text{Li}} \rightarrow \text{Nb}_{\text{Nb}}$ and vice versa. Setting $E_P = 0.58\,\text{eV}$, it is necessary to increase the temperature up to about 600 K to have a similar free polaron contribution; in this case the transport, up to this temperature, would be composed at 50% by slow hops on the random lattice of the antisite defects.

We can define a conversion temperature $T_{conv}$ above which a thermal excitation of

the polaron from $Nb_{Li}$ to $Nb_{Nb}$ occurs as often as a hop to another $Nb_{Li}$. In Figure 6.4.3 this corresponds to the point where the curves relatives to $n_{FF}$ and $n_{PP}$ cross each other, $T_{conv} \sim 350\,\mathrm{K}$ for $E_P = 0.75\,\mathrm{eV}$, while this is $T_{conv} \sim 650\,\mathrm{K}$ in the other case.

### 6.4.2. Trap size effect

Results of Section 6.4.1 show that different thermally activated hopping regimes can exist on dependence of the sample composition and on the temperature. In this section we introduce a simple model that can help to visualize and interpret those results by resorting to the concept of trap size effect (TSE) first developed by Prof. L. Guilbert [103] and partially discussed in [104]. The main idea of this model is to associate to a deep (shallow) trap a spatial region around it, as shown in figure 6.4.4 and consider that any polaron going into this region will surely be captured by the trap, and surely not in the reverse case.

Given a polaron sitting on a certain site $i$ and a trapping site $j$ with lower energy at a distance $r_{ij}$ from the polaron, what is the probability for the polaron to be trapped by the deep level, i.e. to hop towards the lower energy state instead of hopping on an equivalent $i$ site? The answer is found by comparing the hopping frequencies of the two processes. From Eqs. 2.3.6, 2.3.7 and 2.3.8, depending on the values of the characteristic energies and on those of the orbital lengths $a_{ii}$ (for transport) and $a_{ij}$ (for trapping), the probability of being captured by the deep centre $j$ for a fixed temperature is a function of the distance between $i$ and $j$. We define the trapping radius $R_{ij}$ as the distance at which the probability of being captured by the deep centre is equal to the probability to hop on an equivalent site:

$$\nu_{ij}\left(R_{ij},\, T\right) = \nu_{ii}(r_{ii},\, T) \tag{6.4.1}$$

where $r_{ii}$ is the distance between two transport sites and $\nu_{ij}$ is given by Eq. 2.3.6. Clearly, if the distance between $i$ and $j$ is shorter than $R_{ij}$, the polaron is likely to be trapped, and *vice* versa. In Eq. 6.4.1 the hopping distance $r_{ii}$ between the shallow centres $i$, for the case of hopping on a disordered network, can be taken to be equal to the most probable distance between two sites $i$, $r_{ii} = (2\pi N_i)^{-1/3}$, where $N_i$ is the concentration of $i$ sites. For what is concerns the trapping radius, using the hopping frequency 2.3.6 and solving the above-mentioned equation 6.4.1 it is possible to give an analytical expression of $R_{ij}$:

$$R_{ij}(r_{ii}, T) = a_{ij}\left[2\ln\left(\frac{J_{ij}^0}{J_{ii}^0}\right) - \frac{1}{2}\ln\left(\frac{E_i + E_j}{2E_i}\right) + \frac{r_{ii}}{a_{ii}} + \frac{U_{ii} - U_{ij}}{kT}\right] \tag{6.4.2}$$

The last part of the formula shows that there is a dependence on $r_{ii}$ and $1/T$, evidencing that the trapping radius becomes larger by decreasing the concentration of $i$ centres

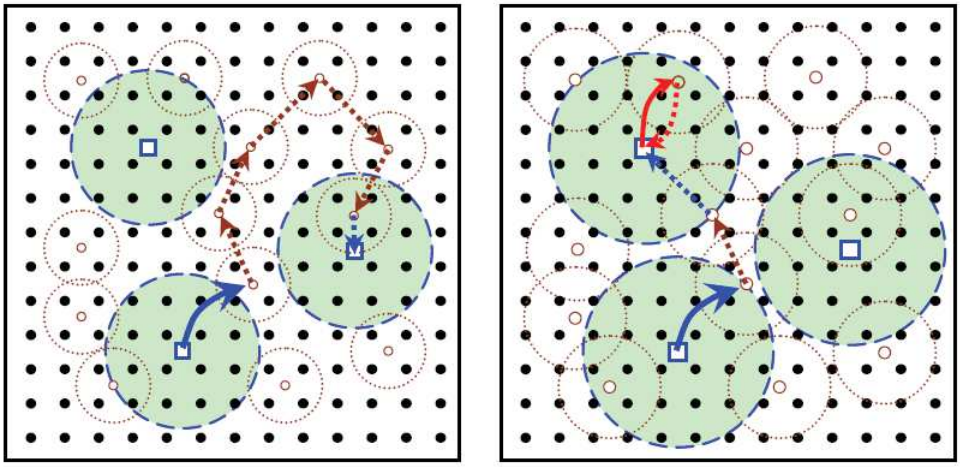


Figure 6.4.4.: Trap size effect versus temperature. Brown dotted circles are trapping spheres surrounding $Nb_{Li}$ traps (brown dots), dashed blue circles are trapping spheres surrounding $Fe_{Li}$ traps (blue squares). Random walks (dotted arrows) shorten at decreasing temperature until they are reduced to a single hop when the trapping spheres overlap. Efficient photoexcitations (blue arrow) are those for which the polaron is formed outside the Fe trapping sphere. Inefficient photoexcitations (red arrow) are those in which the polaron is formed inside the trapping sphere.

and/or decreasing the temperature.

As said, the trapping radius is the distance below which a polaron hopping on $i$ is more likely to be trapped by $j$ rather than continuing to hop. A detailed calculation shows that, for the microscopic parameters used in this work, the trapping probability $p(r_{ij})$ depends on the distance $r_{ij}$ between the $i$ and the $j$ centres according to a step-like function. It is therefore useful to introduce what we call the *black-hole approximation* which amounts to approximate $p(r_{ij})$ with the Heavyside function $1 - H\,(r - R_{ij})$, i.e. to consider that if a polaron finds itself on a $i$ site which is contained into a sphere of radius $R_{ij}(r_{ii}, T)$ centred onto a $j$ centre, it will be certainly trapped in the next hop [103].

Let us consider for example the situation demonstrated in Fig. 6.4.1 (left). For a congruent sample and no Fe traps, the number of hops performed as a free polaron decrease by decreasing the temperature, being almost zero for $T < 200\,\mathrm{K}$. This result can be interpreted in the framework of the TSE by considering that $Nb_{Li}$ antisite traps are surrounded by a trapping volume of radius $R_{FP}$ which depends on temperature. By decreasing $T$, the trapping radius grows, according to Eq. 6.4.2. When its value becomes comparable with the average distance between the $Nb_{Li}$ antisites, the number of hops performed as free polaron decrease drastically (see Fig. 6.4.4). Ultimately, when the $Nb_{Li}$ traps saturate the space, no free polaron can exist in the system: as soon as they form, they become immediately captured by an antisite. For a congruent

| | 400 K | 300 K | 200 K |
|---|---|---|---|
| $R_{PFe}$ | 24 Å | 29 Å | 38 Å |
| $R_{FP}$ | 7 Å | 9 Å | 13 Å |
| $R_{FFe}$ | 14 Å | 18 Å | 25 Å |

Table 6.4.2.: Trapping radius values calculated for a congruent sample at various temperatures.

composition the average distance between antisites is $r_{PP} = 9$ Å. From the Monte Carlo fitting of transient absorption measurements (Sec. 6.3) we know that $a_{FP} = a_{FF} = a = 1.6$ Å, and $E_i = E_F = 0.54$ eV. $E_j = E_P = 0.75$ eV while $J^0$ and $U$ calculation are described in in section 3.3 and 2.3. For the free polaron the typical hopping length is $r_{FF} = 3.765$ Å, the inter-cationic distance. From these microscopical parameters we calculate a trapping radius $R_{FP} = r_{PP} = 9$ Å at $T = 300$ K, meaning that free polarons can perform some hop starting from room temperature and above, in good agreement with our data.

The same reasoning can be applied to other centres. In Table 6.4.2 the radius for different trapping processes are calculated for different temperatures. In the case of antisite defects trapped by iron, the average distance between $Fe^{3+}$ is about 36 Å for sample B/0.34/19.0, 26 Å for sample B/0.82/19.0 and 21 Å for sample B/1.6/19.0. At 200 K the trapping radius of $Fe^{3+}$ is 38 Å so that an antisite-bound polaron at this temperature there can be only direct trapping $Nb_{Li}^{4+} \rightarrow Fe^{3+}$, as recognized in the precedent paragraphs. On the other hand, at e.g. $T = 300$ K we can have multi-hop conduction in the less doped sample B/0.34/19.0, but not in the other two. At $T = 400$ K, bound polarons can hop in all samples except the most doped one. However, at this temperatures, bound to free conversion become active so that the situation is a little more complicated: the trapping radius of Fe towards F polarons is smaller than the one of Fe towards $Nb_{Li}$ and free polarons can be present and contribute to the multi-hopping transport.

Formula 6.4.2 provides a simple tool to estimate approximately the dominant hopping process, permitting to tailor in advance samples characteristics and temperature of work according to the experimental application.

# 7. Continuous-wave measurement

Having established in Chap 5.1 the roles of the different centres as a function of temperature and sample composition, and having tuned the parameters of the MonteCarlo code, we are now ready to test those findings against charge transport under continuous illumination. The situation in this case is a little different: instead of a decaying population of polarons, we have here a quasi-equilibrium situation, in which the trapped charges are continuously replaced by photo-excited ones. Moreover, due to the low intensity used in our measurements ($I_0 < 300\,\mathrm{W/m^2}$), the presence of holes and STEs can safely be neglected. The major experimental novelty of these experiments, compared to results reported in literature (see e.g. [5]), is the dependence of macroscopic quantities such as $\sigma_{ph}$ and $j_{pg}$ from the temperature: this will constitute a tough workbench to test our approach. These studies were done on sample series B and C, i.e. in function of the deep trap and the shallow trap concentration respectively.

## 7.1. Photorefractive measurements results

Using the setup described in Sec. 5.2.2, we recorded the dynamic of the space charge field formation under continuous illumination at different temperatures on the two series of samples B and C (see Tabs. 4.3.2 and 4.3.3). We recall that the first series is characterized by a fixed antisite concentration and a variable deep trap concentration, while the second series has a fixed deep trap content and a varying antisite concentration. From the analysis, detailed in Sec. 5.2, the dielectric rise time $\tau_d$ of the space charge electric field, and the refractive index variation in the stationary situation $\triangle n_{sat}$ , are computed (see Fig. 5.2.4 and Eq. (5.2.4)).

Next we make use of Eqs. 5.2.5 and 5.2.6 to obtain from those data the transport-related quantities $\phi\mu_e\tau$ and $E_{sat}$. In doing this calculation we made use of the known sample characteristics and of the experimental parameters obtained from our setup characterization. The dependence of $r_{33}$ on the temperature (see Fig 1.4.1) has been taken into account. Changes in the dielectric constant due to temperature and sample composition were instead disregarded because their contribution is expected below our experimental accuracy (See Section 1.3).

### 7.1.1. Drift coefficient

The quantity $\mu_e\tau$ obtained from our experimental data using Eq. 5.2.6, derives from Kukhtarev's original formulation, which assumed band-like transport (see Sec. 1.7).

The physical meaning of $\mu_e\tau$ is the distance $L_{drift}$ run by one particle from its birth to its death per unit electric field; we call this quantity *drift coefficient* $\Lambda$:

$$\mu_e\tau = \frac{L_{drift}}{E} = \Lambda \tag{7.1.1}$$

Kukhtarev's formulation was based on a normal diffusion approach, according to which the mobility of a carrier is independent on the time. However, as it will be shown in Chapter 8, this assumption may not hold for bound polaron conduction, which were shown to be the main carriers in Fe:LN in standard conditions in Chapter 5.1. For this reason we prefer here to be more general and use Eq. 7.1.1 as an operative definition of $\Lambda$ as the ratio $L_{drift}/E$, without giving any explicit formulation for it. In Chapter 8 it will be shown that this is a good definition because, even in presence of anomalous diffusion, the drift length $L_{drift}$ is proportional to the applied field $E$. On the other hand, the drift coefficient $\Lambda$ is nothing but the photoconductivity normalized to the charge photo-generation rate $es\frac{I_0}{h\nu}N$.

In Figure 7.1.1 our experimental results are given in terms of $\Lambda$ times the unknown charge photogeneration efficiency $\phi$ for the two samples series as a function of temperature. The first striking result is that all the samples demonstrate qualitatively the same dependence upon cooling: after an initial decrease, the $\phi\Lambda$ product tends to a constant value, showing that the transport process becomes athermal. Second, all the curves appear to be inversely proportional to the deep trap concentration as in a log plot they are just shifted one from the other (Fig. 7.1.1 (top)). This is in agreement with photorefractive literature [105, 106, 33], according to which the drift length should be inversely proportional to the deep trap concentration. The effect of antisite concentration appear modest (Fig. 7.1.1 (bottom)), and the small differences between the three samples of the C series appear to be related to the small change in the Fe content (shown in Figure).

Those data can be put in relation with the findings of Chapter 5.1. As shown in Fig. 6.2.4 the slope break occurring in sample A/0.36/19.0 occurs in the same temperature range of the slope change obtained in photoconductive measurements. This was related in Sec. 6.4.1 to a change in the hopping process. Schematically, we can expect at low $T$ a single-hop regime, in which the newborn polarons are directly trapped $Nb_{Li}^{4+} \rightarrow Fe^{3+}$. Slightly below room temperature, a multi - hop regime is expected with polarons hopping on the disordered $Nb_{Li}$ antisite lattice and a negligible contributions of free polarons. Finally, above room temperature, a mixed conduction regime with both free and bound polarons contribution is expected. However, as shown in Figs. 6.4.1 and 6.4.2 those regimes should depend also on the Fe concentration. This can be understood using the Trap Size Model of Sec. 6.4.2 [103]. Assuming that the Fe traps are surrounded by a finite size trapping region with a temperature-dependent radius that become smaller upon heating. At low temperature the trapping spheres are large and overlap: in this situation the polarons are immediately trapped. This situation

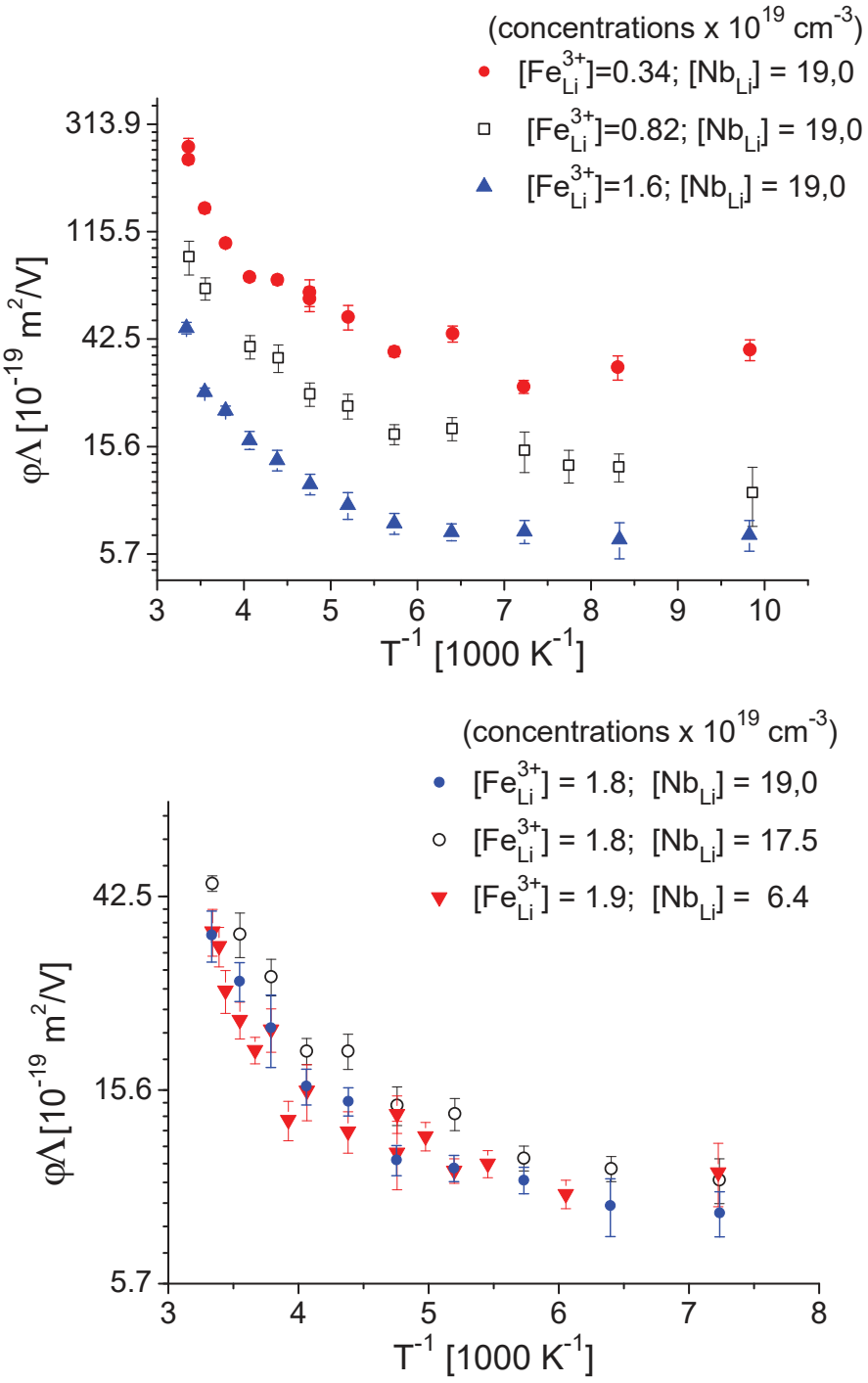


Figure 7.1.1.: Arrhenius plot of the normalized photoconductivity for different deep trap concentrations (top) and shallow trap concentrations (bottom).

would correspond to the single-hop regime. By heating, the trap size is reduced and when the spheres do not overlap any more, the multi-hop regime is enabled. Logically, samples with a low Fe concentration should attain this regime before the others, which means that in Fig. 7.1.1 we should observe e.g. a slope change for the sample B/0.36/19.0 at a lower temperature with respect to sample C/1.94/6.35. This seems not to be the case here, as all the samples present more or less the same temperature dependence. A possible explanation is that the Fe content is too similar between the six samples to evidence a clear change in the conduction mechanism. Concerning samples of the C series, the weak effect of the antisite concentration on the drift coefficient is expected from the general results of Sec. 6.4.1, in which it was shown that in order to raise significantly the free polaron contribution at room temperature, it is necessary to kill the 90% of the antisites present in a congruent material. Moreover the high iron doping level of about $1.9 \cdot 10^{25}\,\mathrm{m}^{-3}$ is sufficient to ensure the single-hop regime for bound antisite polarons till quite high temperatures, and most probably to mask the effect of the different shallow trap concentration. An interesting observation in this respect is that the linear dependence of $\phi\Lambda$ is conserved also at low temperatures. This means that even in the single hop regime the drift coefficient is inversely proportional to $[Fe^{3+}]$.

### 7.1.2. Saturation Space Charge Field

The information on $\triangle n_{sat}$ is converted to an information on the saturation space charge field using Eq. 5.2.5. According to Eqs. 1.7.12 and 7.1.1, $E_{sat} = \frac{L_{pg}}{\Lambda}$ so the results here obtained give an independent information on $\Lambda$ which can be compared with the results of the preceding sections. In particular, it should be noted that here the $E_{sat}$ is independent on the charge photogeneration efficiency $\phi$. This result will be exploited in the next sections.

Experimental data are reported in figure 7.1.2 for the sample series B and C. From experimental values $E_{sat}$ grows by decreasing the temperature, as already mentioned in [107]. It is also possible to see that $E_{sat}$ is proportional to the $[Fe^{3+}]$ concentration, as expected from the photoconductivity measurements and in agreement with the literature [33]. Coherently with the results of Sec 7.1.1, the samples of the C series show very similar results.

### 7.1.3. Photogalvanic length

By multiplying together the two experimental determinations of $\Lambda$ and $E_{sat}$ for each temperature, we obtain also an estimation for the effective photogalvanic length, introduced in Sec. 1.5 and given by $\phi L_{pg}$. The results are shown in Fig. 7.1.3. Although some scattering is present, all the data, both from series B and C, seem to collapse on a single curve which shows a weak temperature dependence. This is expected because the photogalvanic length is a microscopic parameter that should depend essentially on the

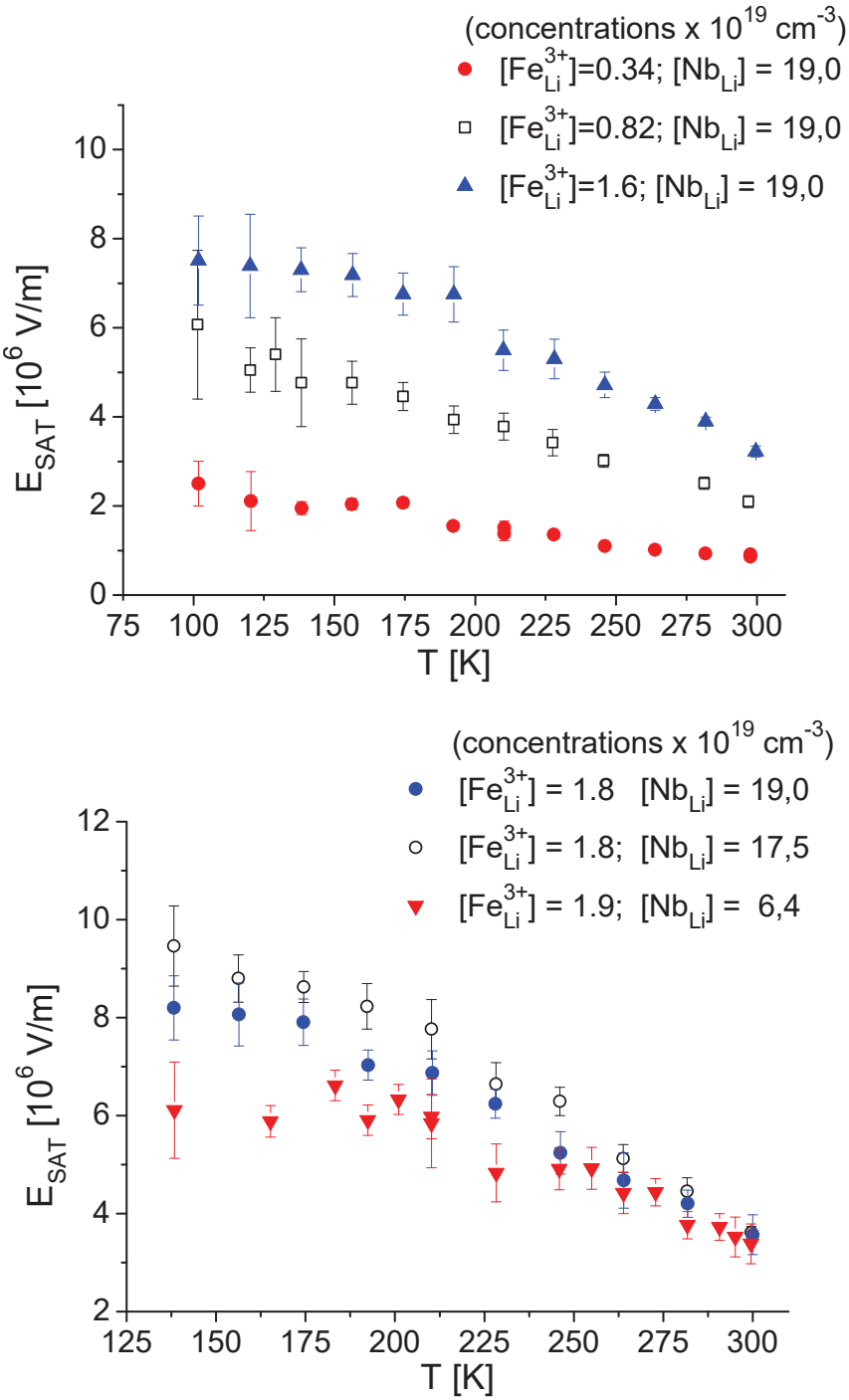


Figure 7.1.2.: Saturation space charge field for the sample series B and C, having respectively a different $Fe^{3+}$ and $Nb_{Li}$ concentrations.

donor element (in our case Fe) and on the excitation wavelength (in our case 534 nm). In particular, our data do not confirm the trend reported in [33] where the specific bulk photovoltaic constant $\beta^* = j_{pg}/(I\, c_{Fe^{2+}})$ shows a small increasing in function of the total iron concentration. Concerning the room temperature value of $\phi L_{pg}$, our results are in line with the values published by Grousson *et al.* [108] which in a sample iron doped with 0.015 wt% (0.28 mol%) obtained at room temperature $\phi L_{pg} = 0.2$ Å with $\lambda = 546$ nm.

Also those data contains the influence of the unknown parameter $\phi$. In principle, the photogalvanic length $L_{pg}$ is an intrinsic property of the material, and this may suggest that the weak temperature dependence is contained only on the free carrier generation probability $\phi$. This would not be surprising: as discussed in Sec. 2.2 the efficiency $\phi$ is determined by a thermally activated hopping process. A rough theoretical estimates for $L_{pg}$ reports 1 Å [43]; assuming this value as independent on $T$, this leads to an order of magnitude for $\phi \sim 10\%$ at room temperature and few percent at low $T$ .

## 7.2. Monte Carlo analysis of photorefractive results

The results of the photorefractive measurements reported in the preceding section did not allow to gain much insight on the microscopic charge transport process; in this paragraph we will resort to the Monte Carlo analysis described in Chap. 3 to extract as much information as possible.

Our simulation code permits to build a statistic of the positions of reached by a bound polaron launched in an infinite medium under the influence of an electric field $E$, assumed along the $c$ axis, to conform to the geometry of our photorefractive measurements (see Fig. 5.2.1). By calculating the first moment $< z >$ of the final polaron distribution, we can compute numerically the drift coefficient defined in Eq. 7.1.1:

$$\Lambda_{num} = \frac{< z >}{E}$$

The electric field is chosen equal to $5 \cdot 10^6$V/m for all the simulations, which is of the order of magnitude of the experimentally determined space charge field values and enough to evidence a shift of the particle distribution, but not too strong to ensure that the dynamic of the system remains stochastic (see paragraph 3.5). The mean shift value $< z >$ induced by this field is in the order of few angstroms as shown in Figure 3.5.1 and it decreases by decreasing the temperature. To reduce the error on the final value of $< z >$ it is necessary to simulate a great number of polarons. The maximum number of polarons simulated at low temperature is $10^6$, a compromise choice between the error on the result and the simulation time, of the order of several days. The microscopic parameters were set in accordance with Sections 3.3 and 6.3, in particular $a = 1.6$ Å, $c = 1.5$ Å, $E_P = 0.75$ eV and $J \sim 0.1$eV.

The result of the simulation cannot be compared directly with our data of Fig. 7.1.1

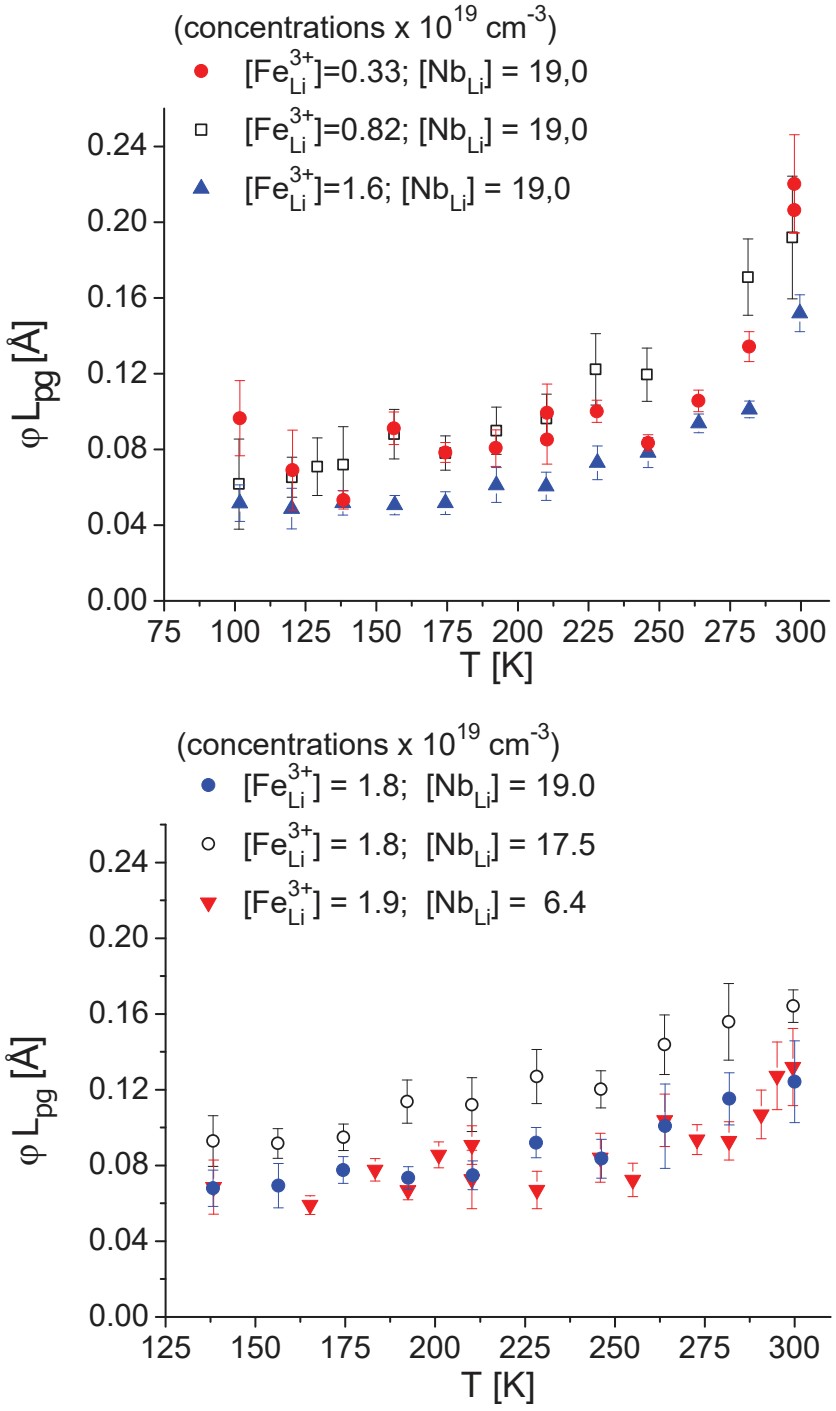


Figure 7.1.3.: Temperature dependence of $\phi L_{pg}$ (normalized photogalvanic current) for the sample series B and C, having respectively a different $Fe^{3+}$ and $Nb_{Li}$ concentrations.

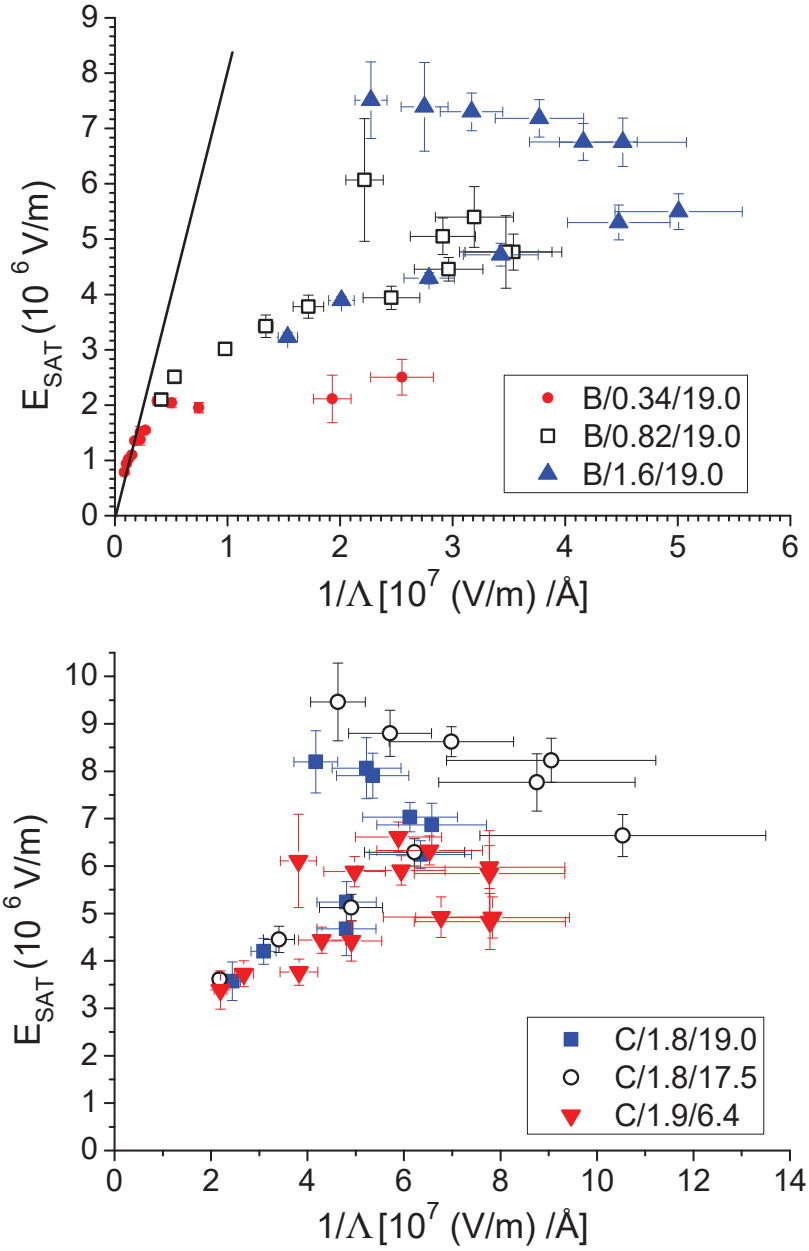


Figure 7.2.1.: Graphs report the value of experimental $E_{sat}$ in function of $1/\Lambda$, computed from simulations for sample series B (top) and C (bottom) setting $a = 1.6\,\text{Å}$, $c = 1.5\,\text{Å}$, $E_P = 0.75\,\text{eV}$, $E_F = 0.54\,\text{eV}$, $E_{Fe} = 0.70\,\text{eV}$, $J = 0.1\text{eV}$ and $E = 5 \cdot 10^6\text{V/m}$. From the linear fit (black line) of sample B/0.34/19.0 it is possible to calculate $L_{pg}$.

because of the presence of the unknown quantity $\phi$. To circumvent this problem, we compare the result of the simulations with $E_{sat}$, (Fig. 7.1.2) because in this quantity the only unknown is the value of the photogalvanic length $L_{pg}$ which is relatively safe to assume as a constant, independent on the sample and on the temperature. We therefore operated as follows: for all the samples of the series B and C and for all the temperatures we calculate the value of $\Lambda_{num}$ by setting the appropriate input conditions. We then construct a graph in which the experimental $E_{sat}$ values measured in the same conditions are plotted against $1/\Lambda$. If the relation $E_{sat} = L_{pg}/\Lambda_{num}$ holds, a straight line should be observed whose slope gives directly the value of $L_{pg}$. In figure 7.2.1 the results of this procedure are reported. It can be seen that the linear trend is obeyed only for the sample B/0.34/19.0 and only for the points corresponding to the longest values of $\Lambda_{num}$. When the simulated drift length becomes too small, $\langle z \rangle \leq 2\,\text{Å}$, corresponding to $1/\Lambda \geq 2 \cdot 10^6 (\text{V/m})/\text{Å}$, the results start to exhibit a nonlinear deviation and are no longer in line with the expectations. An inspection of the results indicates that the linear condition is attained when the transport process is in multi-hop regime. When this regime is lost, i.e. by increasing the Fe content and/or decreasing the temperature, our estimation of $\Lambda_{num}$ appears to be no longer reliable. The reason for this behaviour are still under investigation. However it appears clear that they are somehow connected to direct trapping regime, for which the drift distances are very small and require an extremely high accuracy. We believe however that the simulation's result in the multi-hop regime are reliable. This is confirmed also by the fact that the slope of the linear part of Fig. 7.2.1(top) gives $L_{pg} = (0.80 \pm 0.04)$ Å, in excellent agreement with the value reported by Glass et al. [2].

Assuming that this value is independent on the material composition and on the temperature, we can use it to evaluate the temperature dependence of $\phi$ by dividing the data of Fig. 7.1.3 by $L_{pg}$. The result is reported in Figure 7.2.2, whose value go from about 10% at low temperature to increase to about 15% at room temperature.

Finally by the knowledge of $\phi$ it is possible to correct the data of Fig. 7.1.1 to deduce an experimental determination of the drift coefficient $\Lambda$, Fig. 7.2.3. As expected this value is greater for the less doped sample and according with graphs it depends only on the amount of deep traps. It can be seen for example that at room temperature for the sample having $[\text{Fe}^{3+}] = 1.54 \cdot 10^{19}\text{cm}^{-3}$ with an applied electric field of $5 \cdot 10^6\,\text{V/m}$ the polarons shifts along the z direction of $< z >= 1.2\,\text{Å}$.

Considering accurate the simulation for the multi-hop regime, we can resort to the results of the preceding section (Figure 6.4.2) to obtain some microscopic insight on the measured results. In fact sample B/0.34/19.0 is the only one reaching a significant hop number starting from a temperature $T > 200\,\text{K}$. This is in agreement with the experimental data of Fig. 7.2.3 which shows for the sample B/0.34/19.0 an increase of $\Lambda$ starting from about $T = 200\,\text{K}$. Figure 6.4.3 shows that in a congruent material, up to 250 K the transport is accomplished by bound polarons $\text{Nb}_{\text{Li}}^{4+}$ hopping between antisite defects. In this case, the increase of $\Lambda$ with the temperature is explained by

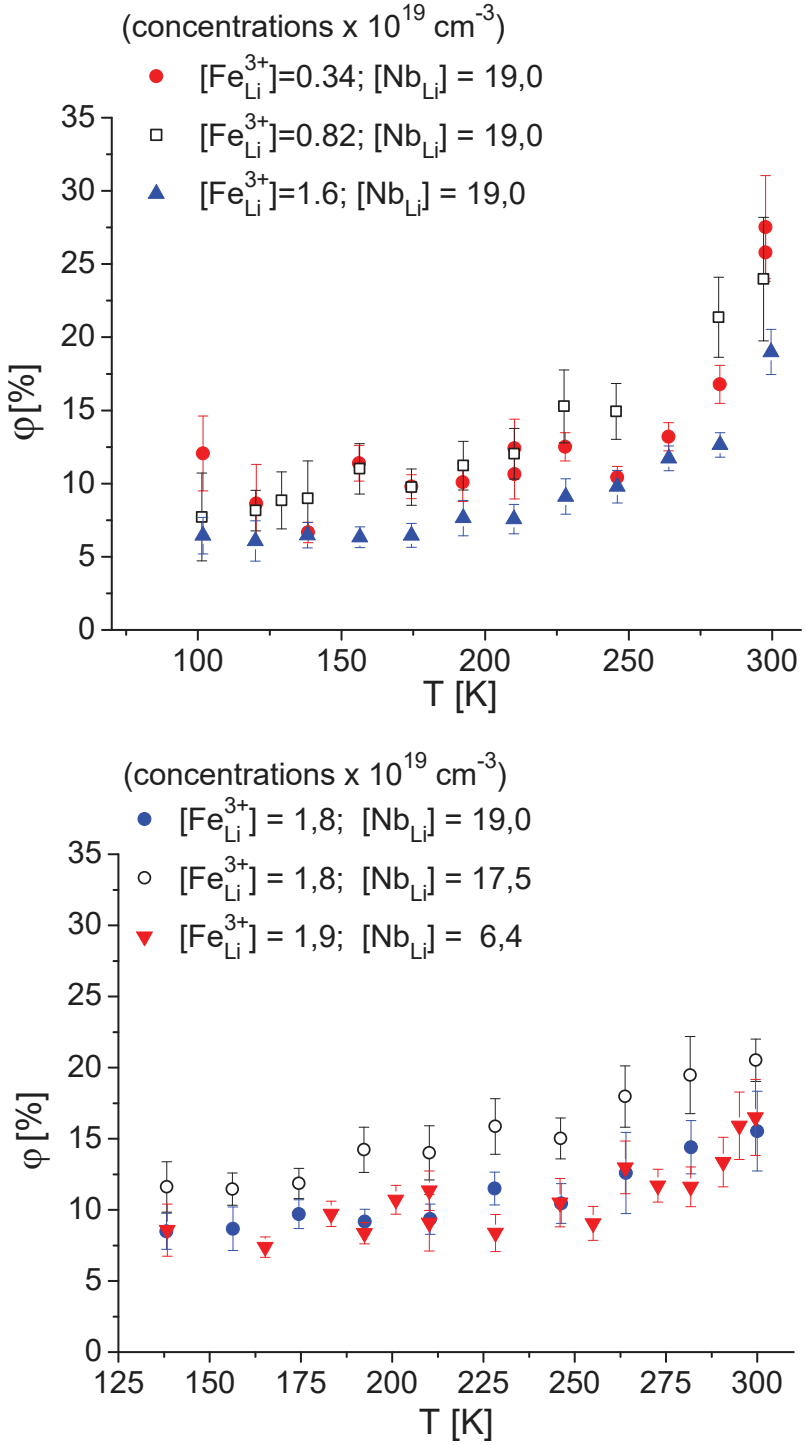


Figure 7.2.2.: Results on the probability value that an electron generated by the absorbed photon is not re-trapped in the initial site, but participate to the transport. Values are reported for sample series B and C.

the fact that the trapping probability becomes less efficient, as it can easily visualized using the trapping radius concept explained in Sec. 6.4.2. Above 250 K, the additional free polaron contribution start to become effective further increasing the mobility.

In conclusion, the obtained results demonstrate that our Monte Carlo code can be used to calculate quantitatively the drift coefficient of iron-doped lithium niobate as a function of temperature and composition, at least for not too doped samples and not too low temperatures. This is precisely the situation encountered in practical applications, where the Fe concentration is generally kept not too high and the sample is at room temperature (or above). From the knowledge of $L_{pg}$ and of $\phi$ a complete microscopic modelling of photorefractive phenomena is possible.

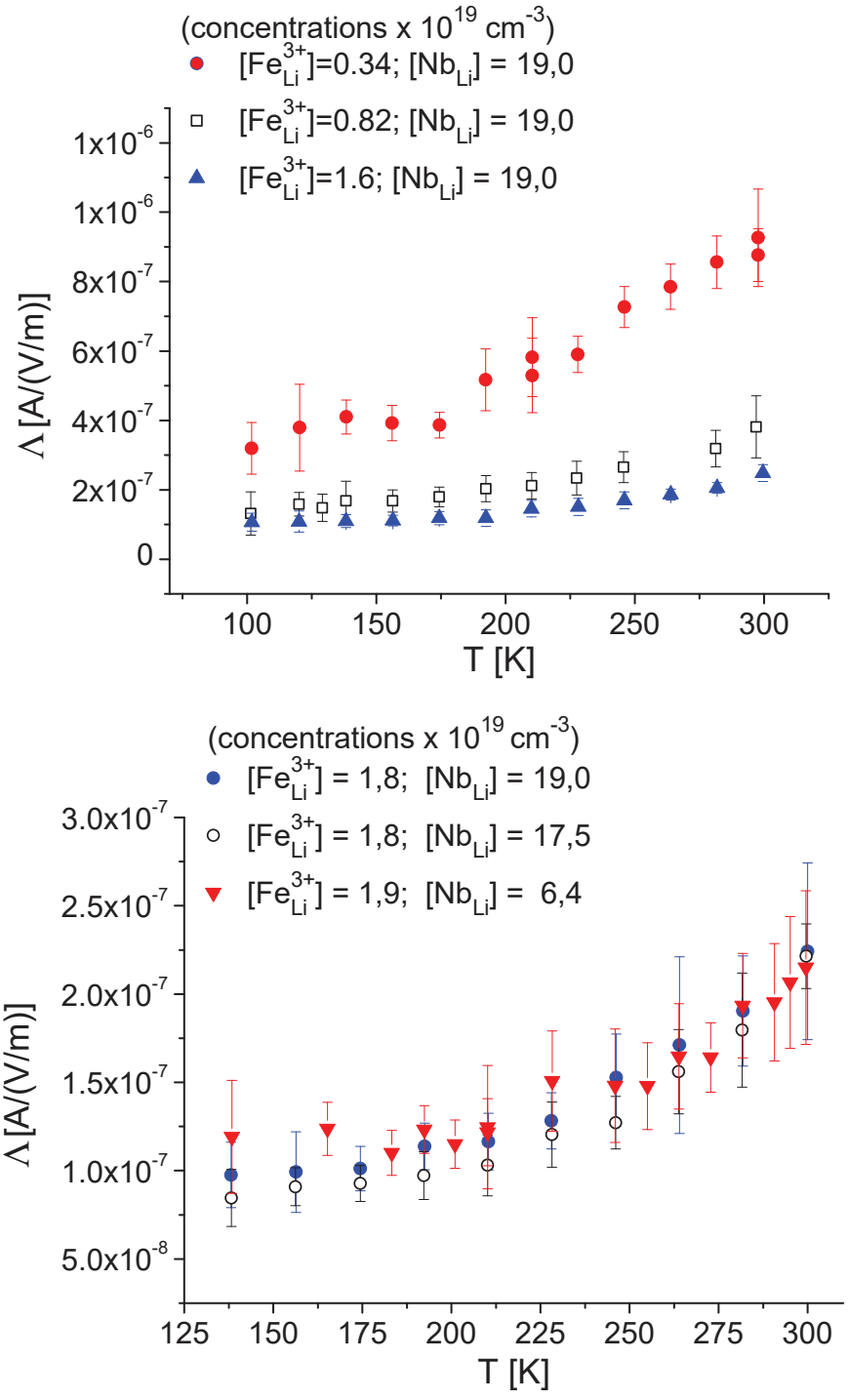


Figure 7.2.3.: Experimental drift coefficient of a particle under the action of an electric field E in function of the temperature for sample series B and C obtained from figure 7.1.1 and corrected by the factor $\phi$.

# 8. Anomalous polaron diffusion

In the last chapter, we provided experimental and numerical results on the drift coefficient $\Lambda$ using an operative definition (Eq. 7.1.1). In this chapter we attempt a more detailed modelling of this parameter. The two main problems we have to deal with are (i) a realistic description of the diffusion process for polarons and (ii) a theoretical expression for their lifetime, in dependence of the diffusion mechanism and of the microscopic details of the trapping process. For the moment we stick to the first problem by assuming a material free of deep traps. The study of the electrons diffusion in the material plays a key role because it permits to study and eventually predict the photo-electric transport properties, such as the mobility of the system when an electric field is applied. The diffusion, at a microscopic level, is related to the random motion of individual particles in the material, and for lithium niobate a large literature is found only in the case of free polarons diffusion, because, moving in the fix structure of niobium site, their motion satisfies the hypothesis of the Brownian motion, for which the normal diffusion theory, such as the second Fick's law and the Einstein relation linking diffusion and mobility, are valid [80]. Unfortunately this case resolves only a very restrict range of practical applications, in particular the one of a stoichiometric sample or the one of a congruent sample but only in high temperatures applications, where the hopping F-F dominates (see section 6.4.1). For the moment, the standard case of the congruent composition at room temperature or low temperatures, where the antisite-bound polarons plays a key role, cannot be completely modelled. The problem arises from the fact that this centre diffuses in a random lattice. The idea here is to show how to deal with this problem by applying the theory of *anomalous diffusion* to the case of lithium niobate, for which the standard diffusion of free polarons becomes a special case.

## 8.1. Normal diffusion

It is useful to recall some concepts from standard diffusion theory. A particle is considered to be subjected to *normal diffusion* if its motion is of Brownian random walk type. The latter is schematically displayed on a two dimensional lattice in figure 8.1.1. In discrete time steps of span $\Delta t$, the test particle is assumed to jump to one of its nearest neighbour sites, here displayed on a square lattice with lattice constant $\Delta x$, with a random direction. If this random walk is followed for a very long time, a "normal" behaviour appears in the sense that the small steps cannot be seen, and the overall

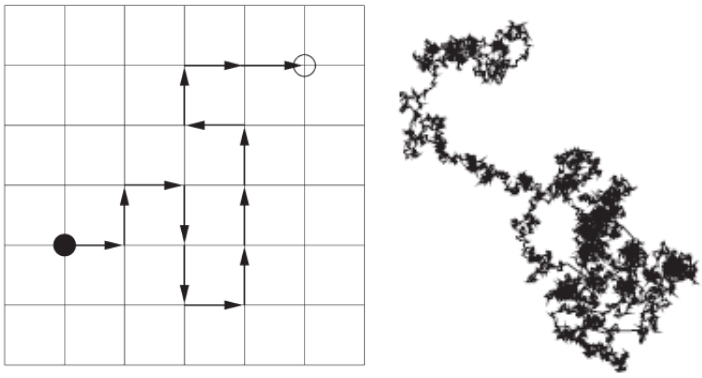

Figure 8.1.1.: Schematic representation of a Brownian random walk. The walker jumps at each time step $t = 0, \Delta t, 2\Delta t, ..., n\Delta t$ to a randomly selected direction, thereby covering the distance $\Delta x$, the lattice constant [109].

motion is determined by the average effect of all of the steps.

To describe this situation mathematically, let us consider particle diffusion along the z-coordiante in a 1D space. The equation describing this phenomena is expressed by the equation (Fick's second law):

$$\frac{\partial W(z,t)}{\partial t} = K\frac{\partial^2 W(z,t)}{\partial z} \tag{8.1.1}$$

where $K$ is the diffusion coefficient and $W$ the probability density function (PDF), which specifies the probability that a particle is located at position z at time $t$. The diffusion equation 8.1.1 is one of the most fundamental equations in physics, being a direct consequence of the central limit theorem. The solution of this equation, if the particle start from a point source $W(z,0) = \delta(z)$ at $z = 0$, $t = 0$ , is:

$$W(z,t) = \frac{1}{\sqrt{4\pi Kt}} e^{-z^2/4Kt} \tag{8.1.2}$$

This one represents a Gaussian distribution with mean value equal to zero and variance $\langle z^2 \rangle = \sigma^2 = 2Kt$ growing linearly with the time.

If only free polarons hopping occurs, the diffusion can be completely described by equation 8.1.1, because electrons move in a random way in the ordered structure of the niobium sublattice, where all site are equivalent, as request in a Brownian motion.

## 8.2. Anomalous diffusion

The starting point for a mathematically rigorous understanding of anomalous diffusion is the Continuous Time Random Walk (CTRW) model. This one is a generalization of the Brownian motion model of diffusion, and was introduced first by Montroll and Weiss in 1965 [110]. In the CTRW, a particle moves toward a given distance, and then waits for a certain time before moving again. The diffusive transport described

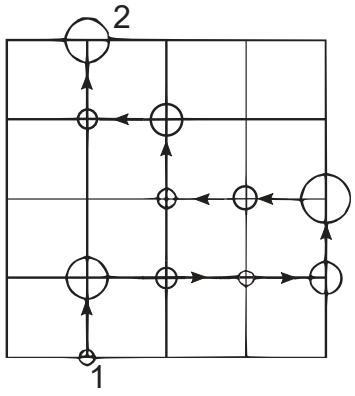


Figure 8.2.1.: Continuous time random walk (CTRW) model. CTRW process on a two-dimensional lattice, generalising the Brownian situation from Fig. 8.1.1. The waiting times are symbolised by the waiting circles the diameter of each is proportional to the waiting time which is to be spent on a given site before the next jump event occurs. In this schema jump lengths are still equidistant [109].

in this theory refers to the movement in space of an ensemble of particles of a given species, accomplished by random motions caused by thermodynamic fluctuations. The main challenge from the normal to the anomalous theory concerns the change in the definition of step length of the random walk. The CTRW model is based on the idea that the length of a given jump, as well as the waiting time elapsing between two successive jumps, follows some heavy tailed distribution drawn from a common PDF $\psi(x,t)$, which will be referred to as the *jump probability distribution function* (PDF). From $\psi(x,t)$, the *jump length pdf* assumes the form of $\lambda(x) = \int_0^\infty \psi(x,t)dt$ while the *waiting time pdf* is $\omega(t) = \int_{-\infty}^{\infty} \psi(x,t)dx$. A schematic cartoon of the CTRW model is drawn in Fig. 8.2.1. Different types of CTRW processes can be categorised by the characteristic waiting time $\tau = \int_0^\infty \omega(t)tdt$ and the jump length variance $\sigma^2(t) = \int_{-\infty}^{\infty} \lambda(x)x^2dx$, being finite or diverging, respectively.

In this vision the general master equation governing the diffusion assumes the form [109]:

$$\frac{\partial W(z,t)}{\partial t} =_0 D_t^{1-\alpha} K_\alpha \frac{\partial^2 W(z,t)}{\partial z^2} \tag{8.2.1}$$

where $K_\alpha$ assumes the meaning of a generalized diffusion constant, having the dimension $[K_\alpha] = \mathrm{m}^2\mathrm{s}^{-\alpha}$ and the fractional derivative operator for $0 < \alpha < 1$ is defined as:

$${}_0D_t^{1-\alpha} W(z,t) = \frac{1}{\Gamma(\alpha)} \frac{\partial}{\partial t} \int_0^t dt' \frac{W(z,t')}{(t-t')^{1-\alpha}} \tag{8.2.2}$$

and for this reason it is known also as *time-fractional* diffusion processes. The appearance of fractional derivatives, inspite of the mathematical complexity of the formula, is a very appealing approach, due to its formal proximity to the analogous standard equations. $\alpha$ is the key parameter classifying the type of diffusion; for $\alpha = 1$, Eq.

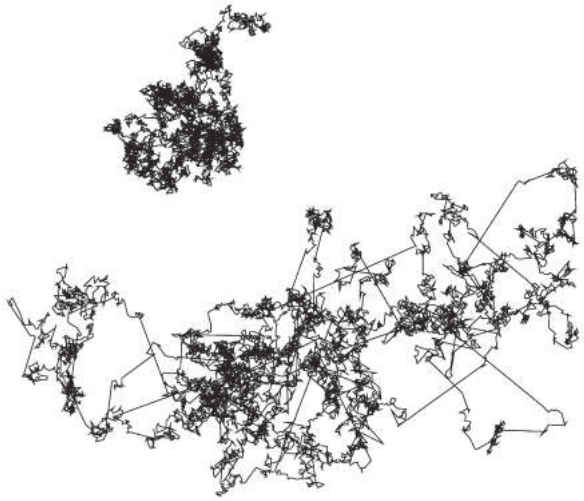

Figure 8.2.2.: Comparison of the trajectories of a subdiffusive random walk (top) and a Lévy walk (bottom). Whereas both trajectories are statistically self-similar, the Lévy walk trajectory possesses a fractal dimension, characterising the island structure of clusters of smaller steps, connected by a long step. Both walks are drawn for the same number of steps (approx. 7000) [109].

8.2.1 becomes the standard Fick's equation so that this case describes the normal diffusion while all other cases are termed anomalous. The case $\alpha > 1$ forms the family of *super-diffusive* processes, for which the characteristic waiting time $T$ is finite and the jump length variance $\sigma^2$ diverges, while the case $\alpha < 1$ gives the *sub-diffusive* family, where the characteristic waiting time $T$ diverges, but the jump length variance $\sigma^2$ is still kept finite. These two situations are depicted in picture 8.2.2. In the bottom it is shown the super-diffusive motion, named Lévy walk, where the overall position is nearly completely determined by the long, rare steps - the "flights" and which are followed by efficient trapping of particles in localized spatial regions, in contrast to the more homogeneous picture of subdiffusion, in the top of the figure.

In the case of polarons diffusing in LN, as it will be shown below, it is found $\alpha < 1$, for this reason we restrict the following theory only to the the sub-diffusive case.

The most general fundamental solution of equation 8.2.1 is given in terms of Fox H-function [111]:

$$W(z,t) = \frac{1}{\sqrt{4\pi K_\alpha t^\alpha}} H_{1,2}^{2,0}\left[\frac{|z|^2}{4K_\alpha t^\alpha}\Big|_{(0,1),(1/2,0)}^{(1-\alpha/2,\alpha)}\right]. \tag{8.2.3}$$

This is a very useful representation on dealing mathematically with infinite expressions whose coefficients involves gamma functions, naturally present in this formulation according to the definition of the fractional derivative 8.2.2. Equation 8.2.3 describes the time evolution of the spatial distribution of an ensemble of sub-diffusive particles starting at the same position, analogously to what is done with normal diffusion.

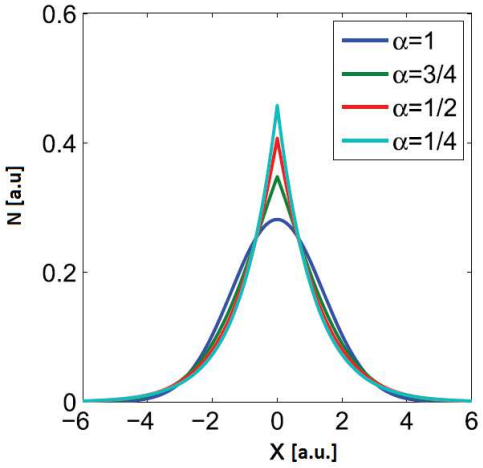


Figure 8.2.3.: 1D Fox H-function after a time $t = 1$ for different values of $\alpha$ [112]. The case of $\alpha = 1$ represents the Gaussian distribution of the normal diffusion.

An alternative formulation of the Fox function based on a series expansion is available, helping the implementation on a personal computer [109]:

$$W(z,t) = \frac{1}{\sqrt{4K_\alpha t^\alpha}} \sum_{n=0}^{\infty} \frac{(-1)^n}{n!\Gamma(1+\alpha[n+1]/2)} \left( \frac{z^2}{K_\alpha t^\alpha} \right)^{n/2} \tag{8.2.4}$$

For $\alpha = 1$, Equation 8.2.3 reduces to the Gaussian diffusion profile, Eq. 8.1.2, as it can be seen in figure 8.2.3, where the solution of 8.2.1 is plotted for various $\alpha$ using the formulation 8.2.4 truncated at the $30^{th}$ order. The variance of the distribution 8.2.3 is not trivial to compute, but in 1D case a solution is possible, leading to the generalization of the Einstein-Stokes-Smoluchowski relation [109]:

$$\left\langle z^2(t) \right\rangle = \frac{2K_\alpha t^\alpha}{\Gamma(1+\alpha)} \tag{8.2.5}$$

where the variance of the distribution is no longer proportional to the time. As for the normal diffusion, in the anomalous case it is possible from the time evolution of the variance to compute the diffusion coefficient and, in addition, the degree of anomaly $\alpha$.

## 8.3. Sub-diffusion under a constant bias

In this section, the treatment of normal and anomalous diffusion problems under the influence of an external *constant* electric field is discussed.

In the case of normal diffusion, one of the simplest way to model the system is in terms of the Fokker-Planck equation (FPE):

$$\frac{\partial W(z,t)}{\partial t} = \left[ \frac{\partial}{\partial z} \frac{V(z)}{\mu} + K \frac{\partial^2}{\partial z^2} \right] W(z,t) \tag{8.3.1}$$

where $\mu$ is the mobility and $V(z)$ is the potential associated to the presence of the

electric field $E$. In this framework, it is possible to calculate the mobility of the diffusing particles from the diffusion coefficient , trough the well known Einstein's relation:

$$\mu = \frac{eK}{k_B T} \tag{8.3.2}$$

The solution of equation 8.3.1 is once again a Gaussian distribution, with the only difference that the first momentum of the distribution, i.e. its the mean value, is no longer zero but is equal to:

$$< z(t) >_F = \frac{eE < z^2(t) >}{2 k_B T} = eE \frac{Kt}{k_B T} \tag{8.3.3}$$

where the last expression is obtained substituting equation 8.2.5 to $< z^2(t) >$. Also in this case single modes of the Fokker-Planck equation relax exponentially in time.

For the description of anomalous transport in the presence of an external field, a fractional extension of the Fokker-Planck equation 8.3.1 is introduced, namely the *fractional* Fokker-Planck equation (FFPE) [109]:

$$\frac{\partial W(z,t)}{\partial t} =_0 D_t^{1-\alpha} \left[ \frac{\partial}{\partial z} \frac{V(z)}{\mu_\alpha} + K_\alpha \frac{\partial^2}{\partial z^2} \right] W(z,t) \tag{8.3.4}$$

where $\mu_\alpha$ now is the generalized mobility of the system. With this mathematical description a generalisation of the Einstein-Stokes-Smoluchowski relation is possible, so that the generalised mobility and diffusion coefficients are connected via the relation:

$$\mu_\alpha = \frac{eK_\alpha}{k_B T} \tag{8.3.5}$$

The solution of the fractional Fokker-Planck equation equation remains a Fox H-function with the difference that first momentum of the distribution in 1D case is equal to:

$$\langle z(t) \rangle_F = E \frac{\mu_\alpha t^\alpha}{\Gamma(1+\alpha)} = v_\alpha t^\alpha \tag{8.3.6}$$

where $v_\alpha$is the "sub-velocity", defined as:

$$v_\alpha(F) = lim_{t\to\infty} \Gamma(1+\alpha) \frac{\langle z(t) \rangle}{t^\alpha} \tag{8.3.7}$$

Thanks to this theory, keeping constant the structure of all formulas, if compared to the normal case, it is possible to show that all formulas recovered for standard normal diffusion can be easily extended to the anomalous case, provided that the generalization quantity now have to been considered. One example of this is the standard formula of the mobility for polaron diffusion expressed in function of the hopping frequency $\nu$ and the hopping length $d$ (Eq. 2.3.5):

$$\mu = \frac{ed^2\nu}{kT} \tag{8.3.8}$$

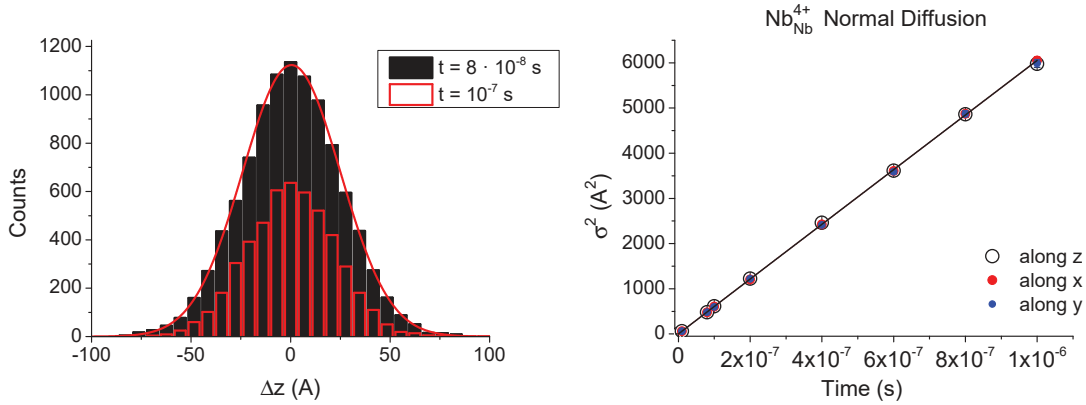


Figure 8.4.1.: (left) Final electron position distribution of a system containing only free polarons in two different time instant. The histogram corresponding to $t = 8 \cdot 10^{-8}$ s is fitted with a Gaussian distribution. (right) Variance of the distribution as a function of the time. Results evidence a normal diffusion of free polarons.

which in the framework of the subdiffusion theory must be substituted by:

$$\mu_\alpha = \frac{ed^2\Gamma(1+\alpha)\nu^\alpha}{kT} \tag{8.3.9}$$

It is also possible to understand better the microscopic meaning of $\Lambda$. $L_{drift}$ is none other than the first momentum of the distribution in presence of the electric field, so from equation 8.3.6 and 8.3.9:

$$\Lambda = \frac{ed^2 < n >^\alpha}{kT} \tag{8.3.10}$$

where $< n >= \nu\tau$ is the average number of hops, given by the polaron lifetime $\tau$ multiplied by the hopping frequency.

## 8.4. Results

### 8.4.1. Diffusion behaviour of free and $\mathbf{Nb_{Li}^{4+}}$ polarons

Making use of the Monte Carlo code developed in the preceding chapters, we try here to test how the analytical model of anomalous diffusion can be applied to the case of polarons diffusing in Lithium Niobate. In all the following paragraphs, the input parameters of the code are chosen according to the values determined in Sections (3.3) and (6.3). The concentration of deep traps is here set equal to zero, to study the pure diffusion problem.

#### Free polarons

The simplest case that can be studied is a LN sample containing only free polarons. This situation would ideally correspond to the case of a slightly reduced, stoichiometric

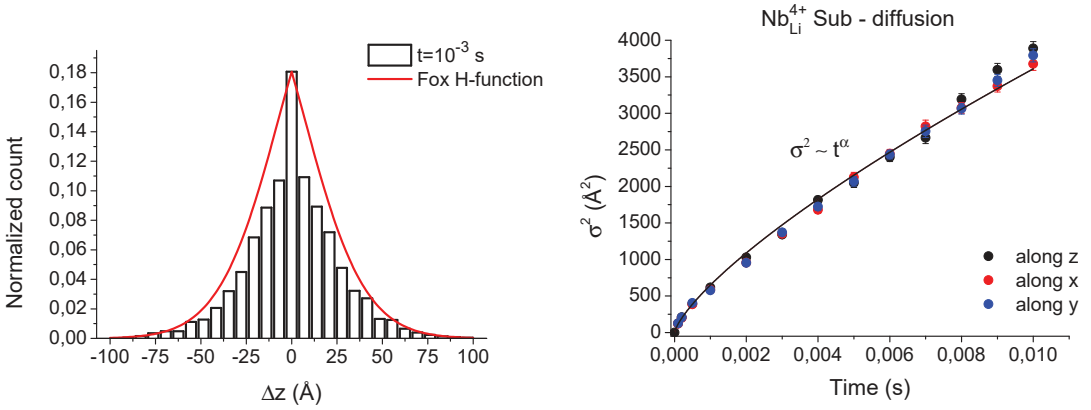


Figure 8.4.2.: (left) Final polaron position distribution of a system containing only antisite-bound polarons at a given time instant. The histogram is reproduced by a Fox H-function distribution (red line) using $\alpha$ and $K_\alpha$ calculated from the study of $\sigma^2(t)$. (right) Variance of the distribution as a function of time. Results evidence a sub-diffusion behaviour of $\mathrm{Nb}_{\mathrm{Li}}^{4+}$ polarons. The red line is the best fit with a function $\sigma^2 = 2K_\alpha t^\alpha/\Gamma(1+\alpha)$.

undoped sample or alternatively to the case of a compensated LN sample above the photorefractive threshold. We simulate the distribution of free polarons after a given time in a sample without antisite shallow defects. The result of the simulations is reported in figure 8.4.1 for $T = 300\,\mathrm{K}$. Graphs show clearly that the final polaron distribution is a Gaussian function. By calculating the variance of the distribution, it can be seen that it increases linearly with time. Free polarons thus diffuse normally and isotropically in the three directions, as expected.

The analytical expression for the diffusion coefficient in the case of normal diffusion in a cubic lattice is easily calculated as $K_{anal} = 6d^2\nu_{FF}$, where $d = 3.76\,\text{Å}$ is the $\mathrm{Nb_{Nb}} - \mathrm{Nb_{Nb}}$ distance on the cationic sublattice and $\nu_{FF}$ is the free polaron hopping frequency given by Eq. 2.3.6, from which we have $K_{anal} = 6 \cdot 10^9\,\text{Å}^2/\text{s}$, in perfect agreement with the output of the simulation. This obviously validates the use of Eq. 2.3.5 for the case of free polaron conduction. We note here that, this result, obtained at room temperature would be valid at any temperature (only the diffusion coefficient would change, due to the temperature dependence of the hopping frequency), since the hopping processes are always of the same type ($F \to F$) and therefore the temperature factor in the hopping frequency act simply as an overall multiplicative constant.

### Bound polarons

We consider now an hypothetical case in which the conduction can occur only by bound polarons hopping among the antisite network. This case would correspond to a congruent sample at moderate or low temperature (see Section 6.4.1). This situation has been implemented in our Monte Carlo code by setting to zero the $J^0_{PF}$ transfer integral prefactor for the hops $P \to F$ (see Sec. 3.3).

The result of this study, performed at $T = 300\,\mathrm{K}$ is reported in figure 8.4.2. In the left side of the figure the distribution of final particle position is reported after the fixed time of $t = 10^{-3}\,\mathrm{s}$. The distribution, characterized by a pronounced peak at the starting position, is clearly not Gaussian. By computing the variance of the distribution along the three axis of the material as a function of time, shown in the left side of figure 8.4.2, the anomalous behaviour is confirmed . In particular a fit with the equation distinctive of the anomalous diffusion $\sigma^2 = \frac{2K_\alpha t^\alpha}{\Gamma(1+\alpha)}$ gives:

$$K_\alpha = (51000 \pm 4000)\,\mathrm{\mathring{A}^2 s^{-\alpha}}$$

$$\alpha = 0.74 \pm 0.01$$

highlighting that bound polarons *sub-diffuse*. This study performed at room temperatures evidences the same subdiffusive exponent $\alpha$ at any temperature (as confirmed by a similar test at 100 K) which is therefore the characteristic exponent for bound polaron transport. This is expected as in the case of the normal diffusion: what changes is the diffusion coefficient, which have a Boltzmann dependence on the temperature. Using the fitted value for $K_\alpha$ and $\alpha$ in Eq. 8.2.4 we are able to correctly reproduce the bound polaron distribution after a given time (Figure 8.4.2 (left)).

### 8.4.2. Diffusion in an undoped congruent sample

As it was shown in the preceding paragraphs, free polarons diffuse with a characteristic exponent $\alpha = 1$, while bound polarons diffuse with $\alpha = 0.74 \pm 0.01$ for all temperatures. The natural question is to understand what is the behaviour of a real case, the undoped congruent LN sample in which both species contribute to the transport. In this case the maps 6.4.1 and 6.4.2 show that the conduction is for 70% made on antisite-bound polarons and for the 20% by free-free hops at 300 K. The rest of hops are conversion between these two sites. Moreover, these percentages are temperature - dependent.

The result is shown in figure 8.4.3 where a simulation of the LN congruent system was performed at room temperature using the same parameters as before. Considering the bound and free polarons as two possible ways to perform the diffusion process, we suppose that the overall second moment of the final distribution is the convolution of the two respective distributions. We guess that the variance of the total process should not be much different from the weighted sum of the respective variances, so that in conclusion we expect for the congruent LN case a law of this kind:

$$\sigma^2 = A \cdot 2Kt + B \cdot 2\frac{K_\alpha}{\Gamma(1+\alpha)}t^\alpha \tag{8.4.1}$$

where $K$, $K_\alpha$ and $\alpha$ are the characteristic parameters for free and bound polaron diffusion respectively, and fixed to values determined in the preceding paragraphs, while

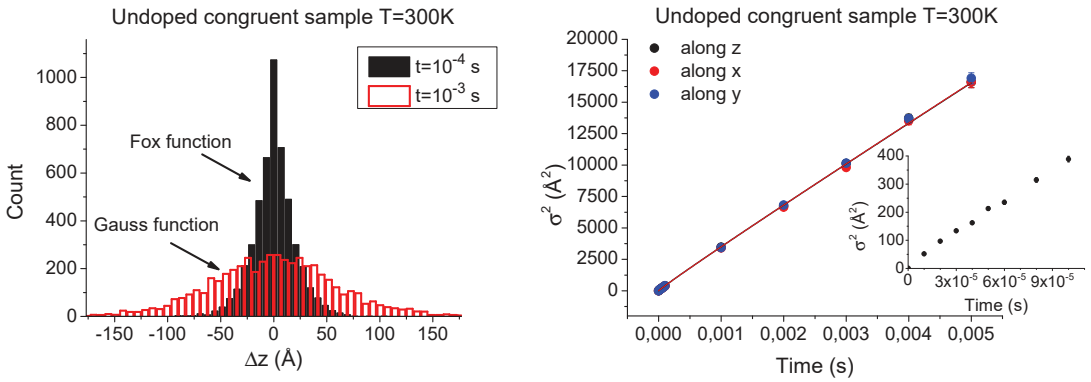


Figure 8.4.3.: (left) Distribution of the polarons final position at two given times. For short times the distribution is a Fox type while at long time it becomes a Gaussian one. (right) Study of the variance of the distribution along x,y and z direction in function of the time. The inset shows a zoom at short times. The black line is a fit of the data with Eq. 8.4.1.

parameters A and B are the weight associated to the normal and anomalous diffusion respectively. A fitting of data in Fig. 8.4.3 evidences a good agreement with the proposed equation. The results of the fit are: $A = (2.01 \pm 0.06) \cdot 10^{-4}$ and $B = (0.83 \pm 0.09)$: the linear contribution has a much lower weight, as expected from the fact that only a limited percentage of the total hops is performed as free polarons. However in view of their much higher mobility, this behaviour dominates for long times. For short times instead, the anomalous behaviour is more evident, as shown in the inset of Figure 8.4.3. These findings are reflected also by the distribution shape, reported in the left side of figure 8.4.3, which evidences that for the short time scale $\left(t \lesssim 10^{-4}\,\mathrm{s}\right)$ a Fox H-function describes correctly the results, while for long times the Gaussian one is more appropriate. These data explain why at cw intensities and for long times the usual Kukhtarev's equations predicts very well materials characteristics as normal diffusion theory is a good approximation of the real case. On the contrary in the pulsed regime, for example in the ns regime as the case of experiments performed in Section 6.1, the sub-diffusion theory is more appropriate.

The same type of study is effectuated at low temperature, and reported in figure 8.4.4. In this regime from maps 6.4.1 and 6.4.2 conduction is for 98% made on antisite-bound polarons and for the 0.1% by free-free hops. The diffusion coefficients at this temperature are estimated by rescaling with a proper Boltzmann factor the values obtained at room temperature (the energy barriers are taken from Tab. 6.3.1) and are: $K = 6.5 \cdot 10^7\,\mathrm{Å}^2/\mathrm{s}$ and $K_\alpha = (102 \pm 8)\,\mathrm{Å}^2/\mathrm{s}^\alpha$. By repeating the same analysis performed above for the case at room temperature, we obtain $A = (1.5 \pm 0.9) \cdot 10^{-6}$ and $B = 6.8 \pm 0.7$. The large relative error in the $A$ parameter is due to the fact that by cooling down the temperature, the diffusion process is greatly slowed down and the "normal" diffusion behaviour is not developed yet, so that our fit bears a large uncertainty for the timescale considered. On the other hand, the smallness of $A$ against

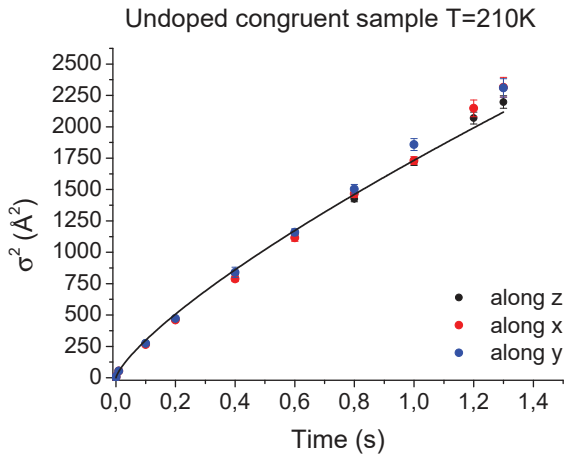


Figure 8.4.4.: Study of the variance of the distribution along x,y and z direction in function of the time at $T = 210\,\mathrm{K}$. From the fit the anomalous coefficient is $\alpha = 0.75 \pm 0.01$.

$B$ indicates that in those conditions bound polaron conduction is dominating. However, if a sufficient time is waited, the normal diffusion behaviour would be restored. Once again, the appearance of normal or anomalous diffusion is a matter of the chosen time window, which in turn is set by the shortest between the measurement time or the polaron lifetime.

### 8.4.3. Polaron mobility in an undoped congruent sample

By combining Eq. 8.3.3 with 8.4.1 we can see that for the drift length a similar relation giving the two independent contributions of free and bound polarons is obtained:

$$< z(t) >_{F,P} = \frac{eE}{kT}\left[A \cdot Kt + B \cdot \frac{K_\alpha}{\Gamma(1+\alpha)} t^\alpha\right] \tag{8.4.2}$$

According to the formula 8.4.2 the first momentum of the distribution, $\langle z \rangle$ grows linearly with the electric field but not with the time. An example of the dependence with the time is shown for the undoped congruent sample, simulated this time with a fixed electric field of $E = 5 \cdot 10^6\,\mathrm{V/m}$ at room temperature (Fig. 8.4.5). In this case the timescale of the process is set by the lifetime of the polaron. In a perfect material where polarons could live very long times (> ms), or where bound polarons are very scarce, normal diffusion would dominate and the drift length would be proportional both to the field and to the polaron lifetime, as in usual theoretical descriptions. Assuming that the polaron lifetime is inversely proportional to the trap density, this would ultimately give the standard relation for the drift coefficient (See Section 7.1.1):

$$\Lambda \sim \mu\tau = \frac{\mu}{\gamma[N_{trap}]}$$

However, for short lifetimes, according to our approach, a more correct description

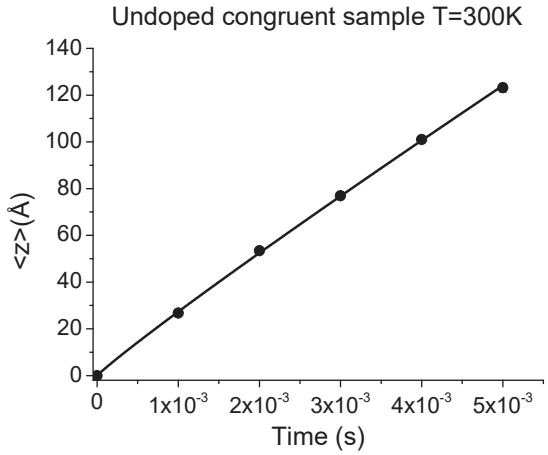


Figure 8.4.5.: Mean value of the position's distribution for given times in the case of undoped congruent sample with an applied electric field of $E = 5{\cdot}10^6$ V/m at room temperature

would be instead:

$$\Lambda \sim A \cdot \mu\tau + B \cdot \mu_\alpha \tau^\alpha$$

where the drift coefficient is no longer inversely proportional to the trap density. Note that for the samples used in this work the polaron lifetime at room temperature is less than $10^{-4}$ s, so that probably we are in this regime. This finding should have some measurable consequences on the photoconductivity (Eq. 1.7.11) and on the saturation space charge field (Eq. 1.7.12). Unfortunately, the quality of our results in Fig. 7.1.1 is not sufficient to evidence this behaviour. The obtained results may be formulated in a more explicit way:

$$\Lambda = \frac{e^2}{kT}\left[A \cdot d_{FF}^2 \nu_{FF} \tau + B \cdot d_{PP}^2 \nu_{PP}^\alpha \tau^\alpha\right]$$

where $\tau$ is the polaron lifetime. The products $A\nu_{FF}\tau$ and $B\nu_{PP}^\alpha\tau^\alpha$ have the physical meaning of "effective number of hops performed as free or as bound" and therefore correlate directly with the results of Fig. 6.4.3. In total we get the simple formula:

$$\Lambda = \frac{e^2}{kT}\left[d_{FF}^2 \langle n_{FF}\rangle + d_{PP}^2 \langle n_{pp}\rangle^\alpha\right]$$

where all the microscopic details are embedded in the effective number of hops, $\langle n_{FF}\rangle$ and $\langle n_{pp}\rangle$. Unfortunately, an analytical way to compute those parameters has still not been worked out.

# Conclusion

In this thesis the charge transport in iron - doped lithium niobate was investigated from the point of view of polaron physics. The motivation for this work resides on the fact that, despite the central role of polarons in this materials has been nowadays accepted, charge transport is still described by equations which are derived considering a band-like transport. The key issue in this respect are the impossibility to relate the phenomenological parameters of the model to a true microscopic understanding.

A set of dedicated experiments were set up to this goal: several samples were produced by Czochralski growth, prepared and characterized with tailored characteristics for this investigation. They were subsequently analysed by a set of complementary techniques providing, to our knowledge for the first time, a comprehensive investigation of charge transport in a wide temperature range. A setup for temperature-dependent photorefractive characterization was designed and realized, and a dedicated simulation software has been written and tuned to describe with sufficient predictive power the charge transport processes. Finally, polaron diffusion in LN was for the first time considered as a case of anomalous transport and the consequences were derived.

One of the main results of this analysis relates to the understanding that in Fe:LN several polaronic species are contributing in parallel to the transport, the relative contribution of each of them being established by the choice of the sample composition or of the experimental conditions. We proved, both by experimental and numerical results, that for typical compositions at low temperature ($T < 270\,\mathrm{K}$) the polarons prefer to hop directly between intrinsic $\mathrm{Nb_{Li}}$ antisite defects, so that their mobility is defined by this process which obeys the laws of anomalous diffusion with a characteristic exponent $\alpha = 0.74 \pm 0.01$. At higher temperatures, some hops start to occur between regular $\mathrm{Nb_{Nb}}$ sites. In this case the diffusion tends to become more and more normal ($\alpha = 1$) and standard equations apply. In general the transport appears as a mixture of the two and, again, which of the two aspects dominates is established by the experimental conditions and how the system is stimulated. The presence of other centres such as holes or self-trapped excitons was discussed as well and shown to be necessary to be taken into account when the system is pumped with a sufficiently high intensity ($I \sim 100\,\mathrm{MW/cm^2}$).

A large part of this work was devoted to develop a simulation code which was tested against experimental data in order to determine a value for some poorly known microscopic parameters. The following results in particular were obtained: (i) orbital parameters ruling the transfer integral for polaron hopping and trapping on a Fe site,

$a = (1.6 \pm 0.1)$ Å and $c = (1.5 \pm 0.1)$ Å respectively. (ii) Stabilization energy provided to the antisite-bound small polaron by the lattice deformation $E_P = (0.75 \pm 0.05)$ eV. This result, significantly higher than previously published results was interpreted with considerations on the lattice structure around the defect. (iii) photogalvanic length for $Fe^{2+}$ donors excited at 543 nm with low intensity light, $L_{pg} = (0.80 \pm 0.04)$ Å. (iv) an estimation of the charge photo-generation efficiency as a function of temperature in the range between 150 and 200 K. The knowledge of those parameter, together with the developed code permits to simulate quantitatively the behaviour of the sample as a function of the experimental parameters. This is a powerful tool of great interest to design materials for applications requiring tailored polaron dynamics, such as for example real time ns- polaron holography [4].

Our studies evidenced that at sufficiently low temperature (depending on the sample composition), the charge transport process is no longer a diffusive one but occurs by a two step excitation-recombination process. This regime, named single-hop regime, is characterized by very short drift lengths and athermal behaviour. In those conditions high values of the space charge field can be easily obtained: also this aspect can be of interest for applications, for example for the realization of highly efficient photorefractive diffraction gratings.

We also discussed the application of a simple model [103, 104] that helps to interpret in a simple way almost all the experimental situations considered here. Although this model cannot substitute a numerical computation, it comes handy to develop a general understanding of the sample behaviour.

The perspective opened by our results are very wide. On one hand the application of the anomalous diffusion theory to polaron transport is, to our knowledge, an absolute novelty, whose effects should be especially visible on the short time scale and below room temperature, which is precisely the regime of application of Transient Absorption spectroscopy. In this context it would be interesting to realize a set of tailored experiments to put in evidence the peculiarities of anomalous diffusion. From a theoretical point of view it would be interesting to investigate the connection between anomalous transport and stretched exponential relaxations, generally assumed as a phenomenological description of the polaron decay. The missing element in this respect is the calculation of the survival probability of an anomalously diffusing particle in a medium with distance-dependent trapping.

A second important and necessary development is re-expression of the Kukhtarev's equation taking into account the special characteristics of polaron transport. The expression for the photoconductivity generally used is rigorously valid only as approximation for normally diffusing (free) polarons and is not accurate in the short time limit or at low temperature when bound polarons are involved. Also the trapping probability, normally assumed to be proportional to the trap concentration, can be regarded as the Smoluchowski's limit for a normally diffusing particle in a medium with diluted traps [113] and its validity needs to be better tested in the light of our results.

From a computational point of view, it would be interesting to check the values of the microscopic parameters obtained by us with theoretical estimates obtained by *ab initio* methods. Also, the Monte Carlo code could be improved to add the effect of other centres, such as hole recombination or to model the effect of energetic disorder in the hopping frequency. This is expected to be an important point, especially at low temperature [103].

From an experimental point of view, some new activities are already on the way. The main limit of the samples used in this work is that they are characterized by a Fe concentration which limited the study to temperatures above 200 K, as below this temperature the single-hop regime is attained. It would be interesting to produce a new series of less doped samples and test on them the methodology developed here. We expect to be able to simulate the charge transport in a larger range and with great accuracy, in order to confirm the results here obtained. Another possibility would be to increase the temperature range towards higher temperatures by performing direct electrical I-V characterization. In this way it would be possible to distinguish between light induced and ionic conduction and explore a transport regime with a large number of hops. Finally, the role of the photo-excitation processes needs to be investigated. It would be very interesting, also in view of photovoltaic applications [7], to understand the mechanisms determining $L_{pg}$ and the photo-emission efficiency $\phi$. Those quantities are determined, as explained in [43], arise from an interplay between coherent (band-like) and hopping transport so that it can be expected that the insights provided by this work could be used also to better understand how to model and master them.

# A. Holographic Measurement

The standard technique normally exploited to measure indirectly macroscopic quantities connected to photorefractive and photogalvanic effect is the holographic technique, schematically represented in Fig. A.0.1. In the case of this thesis this technique is not well suited to extract all the desired experimental quantities. The complete mathematical description can be found in [56] and here only main concepts are briefly described, to highlight the problem connected with this approach.

The interference of two plane waves produces a pattern of light described by:

$$I = I_0 \left[1 + |m| cos\left(Kx + \phi\right)\right] \tag{A.0.1}$$

where $I_0$ is the sum of the intensities of the two beams, $m$ is the fringes visibility and $K$ their spatial frequency. The fringes modulate the charges spatially and create, via the photorefractive effect, a modulated space charge field $E_{SC}$. Therefore this field has a spatial dependence in addition to the well known temporal one. If the "first spatial harmonic approximation" is assumed, i.e. $m \lll 1$, the electric field can be analytically described in a simple way as a periodic real functions of coordinate $x$ of the type :

$$E_{SC}\left(x,t\right) = E_{sat}\left(1 + m\, cos\left(Kx\right)\right)\left(1 - e^{-\frac{t}{\tau}}\right) \tag{A.0.2}$$

This produces in turn in the sample a refractive index modulation having the same modulation of the space charge field. The refractive index modulation is always in phase or counter-phase with the space-charge field and represents a volume phase grating or hologram. The latter diffraction efficiency is computed experimentally as:

$$\eta_{exp} = \frac{I_d}{I_d + I_t} \tag{A.0.3}$$

where $I_d$ is the the diffracted intensity while $I_t$ the transmitted one. Formula A.0.3 can be also theoretically described by the Kogelnik formula [114]:

$$\eta_{teo} = sin^2\left(\frac{\pi \Delta n\, d}{\lambda\, cos\theta}\right) \tag{A.0.4}$$

where $d$ is the grating thickness, $\lambda$ is the beam wavelength and $2\theta$ is the angle between the incident beams. Equation A.0.4 assumes the simplifying approximation of an uniform refractive index modulation along the sample's thickness, so that this one coincide to the grating thickness.

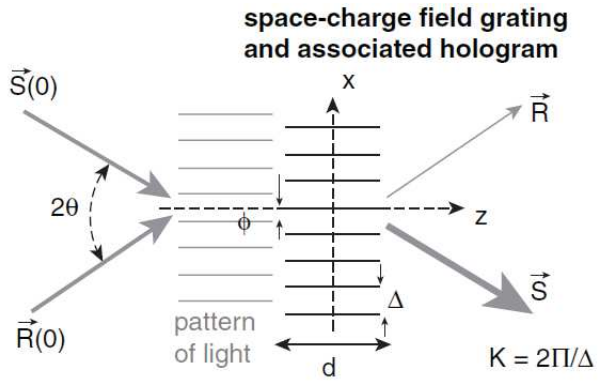


Figure A.0.1.: Sinusoidal pattern of fringes and resulting space-charge field grating.

As already discussed, the photoconductivity of the material is express by the formula $\sigma_{ph} = \frac{\varepsilon\varepsilon_0}{\tau}$, therefore the parameter we are interested in is the characteristic rise/decay time $\tau$ of electric space charge field. This is experimentally realized monitoring the rise/decay of the diffraction efficiency, in fact substituting equation 1.4.3, expressing the refractive index variation $\triangle n$, and equation A.0.2, describing the temporal evolution of the space charge electric field, in A.0.4 and inverting the formula, the diffraction efficiency is linked to the electric space charge field by the expression:

$$E_{SC}(t) \propto \sin^{-1}\sqrt{\eta_{exp}(t)} \tag{A.0.5}$$

To resume, from $I_d$ and $I_t$ it is possible to compute $\tau$ by en exponential fit of the right hand part of the equation A.0.5.

Even if this method is the most employed to extract information on photoconductivity it has some limitations. One of the main restriction for this work, which aim to investigate all microscopic parameters governing photo-generated transport phenomena in Fe:LN, is the impossibility to know the exact value of the space-charge electric field. From equation A.0.5 this one can be computed only up to a multiplicative constant $A$. This in turn prevents the possibility to know the exact value of the photogalvanic current $j_{pg} = \sigma_{ph}E_{sat}$, obliging to develop a dedicated experiment to study this quantity. In principal the multiplicative constant $A$ can be calculated, known the setup geometry and sample's characteristics but one of the main error source is the simplification that the grating and sample thickness coincide and are equal to $d$. Samples considered in this work have a thickness and an absorption coefficient so high that this approximation is not well satisfied. Moreover, from an experimental point of view, the high refractive index of $Fe : LiNbO_3$ may cause a lenslike effect: beams in the sample may be focused or defocused in a different manner, passing through slightly different paths along the crystal, affecting the quality of the interference pattern. In addition, due to the holographic nature of the experiment, the result is very sensitive to vibrations of the system, and this influences adversely measurements at low temperatures due to vibration reported by the cryogenic mechanical system. The dielectric relaxation time

constant $\tau$ is this regime is in the order of hours and the system stabilization is very highly cost demanding.

For all this reasons a different method was exploited, based on a direct measure of the refractive index variation induced by a laser beam and not on the measurement of the diffraction efficiency of a grating.

# B. Input parameters for Monte Carlo simulations

This is a typical input file for the Monte Carlo code developed in this work.

SAMPLE PARAMETERS

Shallow trap concentration $\left[10^{25}\,\mathrm{m}^{-3}\right]$= 19.0

Initial deep trap concentration $\left[10^{25}\,\mathrm{m}^{-3}\right]$ = 0.36

Photo-excited carriers concentrations $\left[10^{25}\,\mathrm{m}^{-3}\right]$ = 0.01

EXPERIMENT PARAMETERS

Temperature [K] = 300

Electric field [V/m] = $5 \cdot 10^6$

SIMULATION PARAMETERS

Polaron creation (possible choice: Nb or $\mathrm{Nb_{Li}}$) = $\mathrm{Nb_{Li}}$

Polaron numbers = 5000

Max hop per polaron = 10000

Experimental time [s] = $10^{-2}$

Soft-pair threshold [$0.5 < SPT < 1$]= 0.9

Cell size x = 80

Cell size y = 80

Cell size z = 80

End site [possible choice: Fe or not significant] = Fe

Memory effect [possible choice: yes or no] = yes

POLARON PARAMETERS

Elastic energies [eV]

| | |
|---|---|
| Deep | 0.70 |
| Shallow | 0.75 |
| Free | 0.54 |

Polaron resonance energy [eV]

| | |
|---|---|
| Deep | 2.62 |
| Shallow | 1.69 |
| Free | 1.09 |

Orbital characteristics length $\left[\text{Å}\right]$

| | Deep | Shallow | Free |
|---|---|---|---|
| Deep | - | $c = 1.5$ | $c = 1.5$ |
| Shallow | $c = 1.5$ | $a = 1.6$ | $a = 1.6$ |
| Free | $c = 1.5$ | $a = 1.6$ | $a = 1.6$ |

Transfer integral prefactor $J_{ij}$ [eV]

| | Deep | Shallow | Free |
|---|---|---|---|
| Deep | - | $J_2 = 0.12$ | $J_2 = 0.12$ |
| Shallow | $J_2 = 0.12$ | $J_1 = 0.11$ | $J_1 = 0.11$ |
| Free | $J_2 = 0.12$ | $J_1 = 0.11$ | $J_1 = 0.11$ |

# Bibliography


[1] T. Volk and M. Wöhlecke, *Lithium Niobate*, Springer-Verlag Berlin Heidelberg, 2009.

[2] A. M. Glass, D. von der Linde, and T. J. Negran, "High voltage bulk photovoltaic effect and the photorefractive process in $LiNbO_3$," *Applied Physics Letters* **25**(4), pp. 233–235, 1974.

[3] B. I. Sturman and V. Fridkin, *The Photovoltaic and Photorefractive Effects in Noncentrosymmetric Materials*, Clarendon, Oxford, 1996.

[4] M. Imlau, H. Badorreck, and C. Merschjann, "Optical nonlinearities of small polarons in lithium niobate," *Applied Physics Reviews* **2**(4), p. 040606, 2015.

[5] P. Günter and J.-P. Huignard, *Photorefractive Materials and Their Applications 1*, vol. 113 of *0342-4111*, Springer New York, 2006.

[6] M. Bazzan and C. Sada, "Optical waveguides in lithium niobate: Recent developments and applications," *Applied Physics Reviews* **2**(4), p. 040603, 2015.

[7] J. He, C. Franchini, and J. M. Rondinelli, "Lithium niobate-type oxides as visible light photovoltaic materials," *Chemistry of Materials* **28**(1), pp. 25–29, 2016.

[8] N. V. Kukhtarev, V. B. Markov, S. G. Odulov, M. S. Soskin, and V. L. Vinetskii, "Holographic storage in electrooptic crystals. I. steady state," *Ferroelectrics* **22**(1), pp. 949–960, 1978.

[9] B. Sturman, F. Agulló-López, M. Carrascosa, and L. Solymar, "On macroscopic description of photorefractive phenomena," *Applied Physics B* **68**, pp. 1013–1020, May 1999.

[10] L. D. Landau, "Uber die Bewegung der Elektronen im Kristallgitter," *Phys. Z. Sowjetunion* **3**, pp. 664 – 665, 1993.

[11] D. Emin, "Small polarons," *Phys. Today* **35**(6), p. 34, 1982.

[12] D. Emin, *Polarons*, Cambridge University Press, 2013.

[13] K. Lengyel, A. Péter, L. Kovács, G. Corradi, L. Pálfalvi, J. Hebling, M. Unferdorben, G. Dravecz, I. Hajdara, Z. Szaller, and K. Polgár, "Growth, defect structure, and THz application of stoichiometric lithium niobate," *Applied Physics Reviews* **2**(4), p. 040601, 2015.

[14] L. Arizmendi, "Photonic applications of Lithium Niobate crystals," *Physica Status Solidi (a)* **201**(2), pp. 253–283, 2004.

[15] W. H. Zachariasen, "Untersuchungen ueber die Kristallstruktur von Sesquioxyden und Verbindungen $ABO_3$," *Skrifter utgitt av det Norske Videnskaps-Akademi i Oslo 1: Matematisk- Naturvidenskapelig Klasse* **4**, pp. 1–165, 1928.

[16] A. A. Ballman, "Growth of piezoelectric and ferroelectric materials by the Czochralski technique," *Journal of the American Ceramic Society* **48**(2), pp. 112–113, 1965.

[17] A. Reisman and F. Holtzberg, "Heterogeneous equilibra in the system $Li_2O - Ag_2O - Nb_2O_5$ an oxide models," *J. Am. Chem. Soc.* **80**(24), pp. 6503–6507, 1958.

[18] H. Hatano, K. Kitamura, and Y. Liu, *Growth and Photorefractive Properties of Stoichiometric* $LiNbO_3$ *and* $LiTaO_3$, pp. 127–164. Springer New York, New York, NY, 2007.

[19] A. Rauber, *Current Topics in Material Science*, vol. 1, North-Holland, 1978.

[20] R. S. Weis and T. K. Gaylord, "Lithium niobate: Summary of physical properties and crystal structure," *Applied Physics A* **37**, pp. 191 – 203, Aug 1985.

[21] F. A. Kröger, *The chemistry of imperfect crystals: Applications of imperfection chemistry - solid state reactions and electrochemistry*, vol. 3, American Elsevier - North-Holland, 1974.

[22] P. Lerner, C. Legras, and J. Dumas, "Stoechiométrie des monocristaux de métaniobate de lithium," *Journal of Crystal Growth* **3**, pp. 231 – 235, 1968.

[23] S. C. Abrahams and P. Marsh, "Defect structure dependence on composition in lithium niobate," *Acta Crystallographica Section B* **42**, pp. 61–68, Feb 1986.

[24] N. Iyi, K. Kitamura, F. Izumi, J. Yamamoto, T. Hayashi, H. Asano, and S. Kimura, "Comparative study of defect structures in lithium niobate with different compositions," *Journal of Solid State Chemistry* **101**(2), pp. 340 – 352, 1992.

[25] O. F. Schirmer and D. von der Linde, "Two-photon- and x-ray-induced $Nb^{4+}$ and $O^-$ small polarons in $LiNbO_3$," *Applied Physics Letters* **33**(1), pp. 35–38, 1978.

[26] T. S. Bush, C. R. A. Catlow, A. V. Chadwick, M. Cole, R. M. Geatches, G. N. Greaves, and S. M. Tomlinson, "Studies of cation dopant sites in metal oxides by EXAFS and computer-simulation techniques," *J. Mater. Chem.* **2**, pp. 309–316, 1992.

[27] G. Zhong, J. Jin, and Z. Wu, "Measurements of optically induced refractive-index damage of lithium-niobate doped with different concentrations of MgO," *J. Opt. Soc. Am.* (70), p. 631, 1980.

[28] T. Vitova, J. Hormes, M. Falk, and K. Buse, "Site-selective investigation of site symmetry and site occupation of iron in Fe-doped lithium niobate crystals," *Journal of Applied Physics* **105**(1), p. 013524, 2009.

[29] M. G. Clark, F. J. DiSalvo, A. M. Glass, and G. E. Peterson, "Electronic structure and optical index damage of iron-doped lithium niobate," *The Journal of Chemical Physics* **59**(12), pp. 6209–6219, 1973.

[30] B. Dischler, J. Herrington, A. Räuber, and H. Kurz, "Correlation of the photorefractive sensitivity in doped $LiNbO_3$ with chemically induced changes in the optical absorption spectra," *Solid State Communications* **14**(11), pp. 1233 – 1236, 1974.

[31] D. Berben, K. Buse, S. Wevering, P. Herth, M. Imlau, and T. Woike, "Lifetime of small polarons in iron-doped lithiumniobate crystals," *Journal of Applied Physics* **87**(3), pp. 1034–1041, 2000.

[32] M. V. Ciampolillo, A. Zaltron, M. Bazzan, N. Argiolas, and C. Sada, "Quantification of iron (Fe) in lithium niobate by optical absorption," *Appl. Spectrosc.* **65**, pp. 216–220, Feb 2011.

[33] K. Peithmann, A. Wiebrock, and K. Buse, "Photorefractive properties of highly-doped lithium niobate crystals in the visible and near-infrared," *Applied Physics B* **68**, pp. 777–784, May 1999.

[34] C. Herzog, G. Poberaj, and P. Günter, "Electro-optic behavior of lithium niobate at cryogenic temperatures," *Optics Communications* **281**(4), pp. 793 – 796, 2008.

[35] E. H. Turner, F. R. Nash, and P. M. Bridenbaugh, "Dependence of linear electro-optic effect and dielectric constant on melt composition in lithium niobate," *Journal of Applied Physics* **41**(13), pp. 5278–5281, 1970.

[36] U. Schlarb and K. Betzler, "Refractive indices of lithium niobate as a function of temperature, wavelength, and composition: A generalized fit," *Phys. Rev. B* **48**, pp. 15613–15620, Dec 1993.

[37] M. Luennemann, U. Hartwig, G. Panotopoulos, and K. Buse, "Electrooptic properties of lithium niobate crystals for extremely high external electric fields," *Applied Physics B* **76**, pp. 403–406, Apr 2003.

[38] J. de Toro, M. Serrano, A. G. Cabañes, and J. Cabrera, "Accurate interferometric measurement of electro-optic coefficients: application to quasi-stoichiometric $LiNbO_3$," *Optics Communications* **154**(1), pp. 23 – 27, 1998.

[39] A. Mendez, A. Garcia-Cabanes, E. Dieguez, and J. M. Cabrera, "Wavelength dependence of electro-optic coefficients in congruent and quasistoichiometric $LiNbO_3$," *Electronics Letters* **35**, pp. 498–499, Mar 1999.

[40] T. Fujiwara, M. Takahashi, M. Ohama, A. Ikushima, Y. Furukawa, and K. Kitamura, "Comparison of electro-optic effect between stoichiometric and congruent $LiNbO_3$," *Electronics Letters* **35**, pp. 499–501(2), March 1999.

[41] V. M. Fridkin, "Bulk photovoltaic effect in noncentrosymmetric crystals," *Crystallography Reports* **46**, pp. 654–658, July 2001.

[42] V. Fridkin and R. Magomadov, "Anomalous photovoltaic effect in $LiNbO_3 : Fe$ in polarized light," *JETP Letters* **30**, pp. 686–688, 1979.

[43] O. F. Schirmer, M. Imlau, and C. Merschjann, "Bulk photovoltaic effect of $LiNbO_3 : Fe$ and its small-polaron-based microscopic interpretation," *Phys. Rev. B* **83**, p. 165106, Apr 2011.

[44] H. G. Festl, P. Hertel, E. Krätzig, and R. von Baltz, "Investigations of the photovoltaic tensor in doped $LiNbO_3$," *physica status solidi (b)* **113**(1), pp. 157 – 164, 1982.

[45] S. I. Karabekyan *Sov. Phys. Solid State* **33**, p. 363, 1991.

[46] P. Günter and J.-P. Huignard, *Photorefractive effects and materials*, pp. 7–73. Springer Berlin Heidelberg, Berlin, Heidelberg, 1988.

[47] A. Ashkin, G. D. Boyd, J. M. Dziedzic, R. G. Smith, A. A. Ballman, J. J. Levinstein, and K. Nassau, "Optically induced refractive index inhomogeneities in $LiNbO_3$ and $LiTaO_3$," *Applied Physics Letters* **9**(1), pp. 72–74, 1966.

[48] F. S. Chen, "Optically induced change of refractive indices in $LiNbO_3$ and $LiTaO_3$," *Journal of Applied Physics* **40**(8), pp. 3389–3396, 1969.

[49] D. L. Staebler and W. Phillips, "Fe-doped $LiNbO_3$ for read-write applications," *Appl. Opt.* **13**, pp. 788–794, Apr 1974.

[50] R. Orlowski and E. Krätzig, "Holographic method for the determination of photoinduced electron and hole transport in electro-optic crystals," *Solid State Communications* **27**(12), pp. 1351 – 1354, 1978.

[51] J. Feinberg, D. Heiman, A. R. T. Jr., and R. W. Hellwarth, "Photorefractive effects and light-induced charge migration in barium titanate," *Journal of Applied Physics* **51**(3), pp. 1297–1305, 1980.

[52] I. Nee, M. Müller, K. Buse, and E. Krätzig, "Role of iron in lithium-niobate crystals for the dark-storage time of holograms," *Journal of Applied Physics* **88**(7), pp. 4282–4286, 2000.

[53] A. A. Zozulya and D. Z. Anderson, "Propagation of an optical beam in a photorefractive medium in the presence of a photogalvanic nonlinearity or an externally applied electric field," *Phys. Rev. A* **51**, pp. 1520–1531, Feb 1995.

[54] T. Hall, R. Jaura, L. Connors, and P. Foote, "The photorefractive effect - A review," *Progress in Quantum Electronics* **10**(2), pp. 77 – 146, 1985.

[55] S. Bian, "Estimation of photovoltaic field in $LiNbO_3$ crystal by Z-scan," *Optics communications* **141**(5), pp. 292–297, 1997.

[56] J. Frejlich, *Photorefractive Materials: Fundamental Concepts, Holographic Recording and Materials Characterization*, Wiley, 2006.

[57] D. Emin, "Optical properties of large and small polarons and bipolarons," *Phys. Rev. B* **48**, pp. 13691–13702, Nov 1993.

[58] O. F. Schirmer, M. Imlau, C. Merschjann, and B. Schoke, "Electron small polarons and bipolarons in $LiNbO_3$," *Journal of Physics: Condensed Matter* **21**(12), p. 123201, 2009.

[59] T. Holstein, "Studies of polaron motion," *Annals of Physics* **8**(3), pp. 343 – 389, 1959.

[60] B. Faust, H. Müller, and O. F. Schirmer, "Free small polarons in $Fe : LiNbO_3$," *Ferroelectrics* **153**(1), pp. 297–302, 1994.

[61] S. Sasamoto, J. Hirohashi, and S. Ashihara, "Polaron dynamics in lithium niobate upon femtosecond pulse irradiation: Influence of magnesium doping and stoichiometry control," *Journal of Applied Physics* **105**(083102), 2009.

[62] H. H. Nahm and C. H. Park, "First-principles study of microscopic properties of the Nb antisite in $LiNbO_3$: Comparison to phenomenological polaron theory," *Phys. Rev. B* **78**, p. 184108, Nov 2008.

[63] S. Sanna, "Bound electron polarons in lithium niobate," in *2015 Symposium on Piezoelectricity, Acoustic Waves, and Device Applications (SPAWDA)*, pp. 523–527, Oct 2015.

[64] A. Sanson, A. Zaltron, N. Argiolas, C. Sada, M. Bazzan, W. G. Schmidt, and S. Sanna, "Polaronic deformation at the $Fe^{2+/3+}$ impurity site in $Fe : LiNbO_3$ crystals," *Phys. Rev. B* **91**, p. 094109, Mar 2015.

[65] O. F. Schirmer, "$O^-$ bound small polarons in oxide materials," *Journal of Physics: Condensed Matter* **18**(43), p. R667, 2006.

[66] P. Herth, T. Granzow, D. Schaniel, T. Woike, M. Imlau, and E. Krätzig, "Evidence for light-induced hole polarons in $LiNbO_3$," *Phys. Rev. Lett.* **95**, p. 067404, Aug 2005.

[67] L. Halliburton, K. Sweeney, and C. Chen, "Electron spin resonance and optical studies of point defects in lithium niobate," *Nuclear Instruments and Methods in Physics Research Section B: Beam Interactions with Materials and Atoms* **1**(2), pp. 344 – 347, 1984.

[68] O. F. S. J. Koppitz and A. I. Kuznetsov, "Thermal dissociation of bipolarons in reduced undoped $LiNbO_3$," *EPL (Europhysics Letters)* **4**(9), p. 1055, 1987.

[69] O. Schirmer, S. Juppe, and J. Koppitz, "Electron-spin-resonance, optical and photovoltaic studies of reduced undoped $Fe : LiNbO_3$," *Crystal Lattice Defects and Amorphous Materials* **16**(1-4), pp. 353–357, 1987.

[70] R. Williams and K. Song, "The self-trapped exciton," *Journal of Physics and Chemistry of Solids* **51**(7), pp. 679 – 716, 1990.

[71] D. M. Krol, G. Blasse, and R. C. Powell, "The influence of the Li/Nb ratio on the luminescence properties of $LiNbO_3$," *The Journal of Chemical Physics* **73**(1), pp. 163–166, 1980.

[72] G. Zatryb, A. Podhorodecki, J. Misiewicz, J. Cardin, and F. Gourbilleau, "On the nature of the stretched exponential photoluminescence decay for silicon nanocrystals," *Nanoscale Research Letters* **6**, p. 106, Jan 2011.

[73] F. Klose, M. Wöhlecke, and S. Kapphan, "Uv-excited luminescence of $LiNbO_3$ and $LiNbO_3 : Mg$," *Ferroelectrics* **92**(1), pp. 181–187, 1989.

[74] C. Fischer, M. Wöhlecke, T. Volk, and N. Rubinina, "Influence of the damage resistant impurities Zn and Mg on the $UV - Excited$ luminescence in $LiNbO_3$," *physica status solidi (a)* **137**(1), pp. 247–255, 1993.

[75] T. Kämpfe, A. Haußmann, L. M. Eng, P. Reichenbach, A. Thiessen, T. Woike, and R. Steudtner, "Time-resolved photoluminescence spectroscopy of $Nb_{Nb}^{4+}$ and $O^-$ polarons in $LiNbO_3$ single crystals," *Phys. Rev. B* **93**, p. 174116, May 2016.

[76] H. Kurz, E. Krätzia, W. Keune, H. Engelmann, U. Gonser, B. Dischler, and A. Räuber, "Photorefractive centers in $LiNbO_3$, studied by optical-, Mössbauer- and EPR-methods," *Applied physics* **12**, pp. 355–368, Apr 1977.

[77] C. Merschjann, B. Schoke, D. Conradi, M. Imlau, G. Corradi, and K. Polgár, "Absorption cross sections and number densities of electron and hole polarons in congruently melting $LiNbO_3$," *Journal of Physics: Condensed Matter* **21**(1), p. 015906, 2009.

[78] Y. Qiu, K. B. Ucer, and R. T. Williams, "Formation time of a small electron polaron in $LiNbO_3$: measurements and interpretation," *physica status solidi (c)* **2**(1), pp. 232–235, 2005.

[79] J. Carnicero, M. Carrascosa, G. García, and F. Agulló-López, "Site correlation effects in the dynamics of iron impurities $Fe^{2+}/Fe^{3+}$ and antisite defects $Nb_{Li}^{4+}/Nb_{Li}^{5+}$ after a short-pulse excitation in $LiNbO_3$," *Phys. Rev. B* **72**, p. 245108, Dec 2005.

[80] I. G. Austin and N. F. Mott, "Polarons in crystalline and non-crystalline materials," *Advances in Physics* **50**(7), pp. 757–812, 2001.

[81] S. Abrahams, J. Reddy, and J. Bernstein, "Ferroelectric lithium niobate. 3. single crystal X-ray diffraction study at 24C," *Journal of Physics and Chemistry of Solids* **27**(6), pp. 997 – 1012, 1966.

[82] R. A. Marcus, "On the theory of oxidation-reduction reactions involving electron transfer. I," *The Journal of Chemical Physics* **24**(5), pp. 966–978, 1956.

[83] A. Dhar and A. Mansingh, "Optical properties of reduced lithium niobate single crystals," *Journal of Applied Physics* **68**(11), pp. 5804–5809, 1990.

[84] S. Mamoun, A. Merad, and L. Guilbert, "Energy band gap and optical properties of lithium niobate from ab initio calculations," *Computational Materials Science* **79**, pp. 125 – 131, 2013.

[85] I. I. Fishchuk, A. Kadashchuk, H. Bässler, and S. Nešpůrek, "Nondispersive polaron transport in disordered organic solids," *Phys. Rev. B* **67**, p. 224303, Jun 2003.

[86] C. Merschjann, B. Schoke, and M. Imlau, "Influence of chemical reduction on the particular number densities of light-induced small electron and hole polarons in nominally pure $LiNbO_3$," *Physical Review B* **76**(8), p. 085114, 2007.

[87] F. Jansson, *Charge transport in disordered materials : simulations, theory, and numerical modeling of hopping transport and electron-hole recombination.* PhD thesis, Åbo Akademi University, 2011. ISBN: 9521226102, 9789521226106.

[88] Y. Okamoto, P. Wang, and J. F. Scott, "Analysis of quasielastic light scattering in $LiNbO_3$ near $T_C$," *Phys. Rev. B* **32**, pp. 6787–6792, Nov 1985.

[89] Y. Zhang, L. Guilbert, P. Bourson, K. Polgár, and M. D. Fontana, "Characterization of short-range heterogeneities in sub-congruent lithium niobate by micro-Raman spectroscopy," *Journal of Physics: Condensed Matter* **18**(3), p. 957, 2006.

[90] V. Caciuc, A. V. Postnikov, and G. Borstel, "Ab initio structure and zone-center phonons in $LiNbO_3$," *Phys. Rev. B* **61**, pp. 8806–8813, Apr 2000.

[91] Z. Jian-Lin, Z. Peng, Z. Jian-Bo, Y. De-Xing, Y. Dong-Sheng, and L. En-Pu, "Visualizations of light-induced refractive index changes in photorefractive crystals employing digital holography," *Chinese Physics Letters* **20**(10), p. 1748, 2003.

[92] L. Vittadello, A. Zaltron, N. Argiolas, M. Bazzan, N. Rossetto, and R. Signorini, "Photorefractive direct laser writing," *Journal of Physics D: Applied Physics* **49**(12), p. 125103, 2016.

[93] D. C. Ghiglia and M. D. Pritt, *Two-dimensional phase unwrapping: theory, algorithms, and software*, vol. 4, Wiley New York, 1998.

[94] M. A. Herráez, D. R. Burton, M. J. Lalor, and M. A. Gdeisat, "Fast two-dimensional phase-unwrapping algorithm based on sorting by reliability following a noncontinuous path," *Appl. Opt.* **41**, pp. 7437–7444, Dec 2002.

[95] C. Merschjann, D. Berben, M. Imlau, and M. Wöhlecke, "Evidence for two-path recombination of photoinduced small polarons in reduced $LiNbO_3$," *Phys. Rev. Lett.* **96**, p. 186404, May 2006.

[96] R. Kohlrausch, "Ueber das Dellmann'sche Elektrometer," *Annalen der Physik* **148**(11), pp. 353–405, 1847.

[97] S. Messerschmidt, "Private communication.".

[98] I. S. Akhmadullin, V. A. Golenishchev-Kutuzov, S. A. Migachev, and S. P. Mironov, "Low-temperature electrical conductivity of congruent lithium niobate crystals," *Physics of the Solid State* **40**, pp. 1190–1192, Jul 1998.

[99] D. Conradi, C. Merschjann, B. Schoke, M. Imlau, G. Corradi, and K. Polgár, "Influence of Mg doping on the behaviour of polaronic light-induced absorption in $LiNbO_3$," *physica status solidi (RRL) Rapid Research Letters* **2**(6), pp. 284–286, 2008.

[100] I. M. Zaritskii, L. G. Rakitina, G. Corradi, K. Polgar, and A. A. Bugai, "A new trapped-hole radiation defect in heavily Mg-doped $LiNbO_3$," *Journal of Physics: Condensed Matter* **3**(43), p. 8457, 1991.

[101] S. L. Shamblin, B. C. Hancock, Y. Dupuis, and M. J. Pikal, "Interpretation of relaxation time constants for amorphous pharmaceutical systems," *Journal of Pharmaceutical Sciences* **89**(3), pp. 417–427, 2000.

[102] S. Sanna, S. Neufeld, M. Rüsing, G. Berth, A. Zrenner, and W. G. Schmidt, "Raman scattering efficiency in $LiTaO_3$ and $LiNbO_3$ crystals," *Phys. Rev. B* **91**, p. 224302, Jun 2015.

[103] L. Guilbert *Private Communication* .

[104] I. Mhaouech and L. Guilbert, "Temperature dependence of small polaron population decays in iron-doped lithium niobate by monte carlo simulations," *Solid State Sciences* **60**, pp. 28 – 36, 2016.

[105] E. Krätzig, "Photorefractive effects and photoconductivity in $LiNbO_3$ : Fe," *Ferroelectrics* **21**(1), pp. 635–636, 1978.

[106] E. Krätzig and R. Orlowski, "Light induced charge transport in doped $LiNbO_3$ and $LiTaO_3$," *Ferroelectrics* **27**(1), pp. 241–244, 1980.

[107] P. A. Augstov and K. K. Shvarts, "The temperature and light intensity dependence of photorefraction in $LiNbO_3$," *Applied physics* **21**, pp. 191–194, Feb 1980.

[108] R. Grousson, M. Henry, S. Mallick, and S. L. Xu, "Measurement of bulk photovoltaic and photorefractive characteristics of iron doped $LiNbO_3$," *Journal of Applied Physics* **54**(6), pp. 3012–3016, 1983.

[109] R. Metzler and J. Klafter, "The random walk's guide to anomalous diffusion: a fractional dynamics approach," *Physics Reports* **339**(1), pp. 1–77, 2000.

[110] E. W. Montroll and G. H. Weiss, "Random walks on lattices. II," *Journal of Mathematical Physics* **6**(2), pp. 167–181, 1965.

[111] H. J. Haubold, A. M. Mathai, and R. K. Saxena, "Mittag-Leffler functions and their applications," *Journal of Applied Mathematics* **2011**, p. 51, 2011.

[112] B. Jin and W. Rundell, "A tutorial on inverse problems for anomalous diffusion processes," *Inverse Problems* **31**(3), p. 035003, 2015.

[113] M. Von Smoluchowski, "Drei Vortrage uber Diffusion. Brownsche Bewegung und Koagulation von Kolloidteilchen," *Z. Phys.* **17**, pp. 557–585, 1916.

[114] H. Kogelnik, "Coupled wave theory for thick hologram gratings," *The Bell System Technical Journal* **48**, pp. 2909–2947, Nov 1969.